ISSN 2587-1366

TURKISH JOURNAL OF ENGINEERING

VOLUME 3 ISSUE 2 APRIL 2019

JOURNAL SECRETARY

TURKISH JOURNAL OF ENGINEERING (TUJE)

Turkish Journal of Engineering (TUJE) is a multi-disciplinary journal. The Turkish Journal of Engineering (TUJE) publishes the articles in English and is being published 4 times (January, April, July and October) a year. The Journal is a multidisciplinary journal and covers all fields of basic science and engineering. It is the main purpose of the Journal that to convey the latest development on the science and technology towards the related scientists and to the readers. The Journal is also involved in both experimental and theoretical studies on the subject area of basic science and engineering. Submission of an article implies that the work described has not been published previously and it is not under consideration for publication elsewhere. The copyright release form must be signed by the corresponding author on behalf of all authors. All the responsibilities for the article belongs to the authors. The publications of papers are selected through double peer reviewed to ensure originality, relevance and readability.

AIM AND SCOPE

The Journal publishes both experimental and theoretical studies which are reviewed by at least two scientists and researchers for the subject area of basic science and engineering in the fields listed below:

Aerospace Engineering
Environmental Engineering
Civil Engineering
Geomatic Engineering
Mechanical Engineering
Geology Science and Engineering
Mining Engineering
Chemical Engineering
Metallurgical and Materials Engineering
Electrical and Electronics Engineering
Mathematical Applications in Engineering
Computer Engineering
Food Engineering

PEER REVIEW PROCESS

All submissions will be scanned by iThenticate® to prevent plagiarism. Author(s) of the present study and the article about the ethical responsibilities that fit PUBLICATION ETHICS agree. Each author is responsible for the content of the article. Articles submitted for publication are priorly controlled via iThenticate ® (Professional Plagiarism Prevention) program. If articles that are controlled by iThenticate® program identified as plagiarism or self-plagiarism with more than 25% manuscript will return to the author for appropriate citation and correction. All submitted manuscripts are read by the editorial staff. To save time for authors and peer-reviewers, only those papers that seem most likely to meet our editorial criteria are sent for formal review. Reviewer selection is critical to the publication process, and we base our choice on many factors, including expertise, reputation, specific recommendations and our own previous experience of a reviewer's characteristics. For instance, we avoid using people who are slow, careless or do not provide reasoning for their views, whether harsh or lenient. All submissions will be double blind peer reviewed. All papers are expected to have original content. They should not have been previously published and it should not be under review. Prior to the sending out to referees, editors check that the paper aim and scope of the journal. The journal seeks minimum three independent referees. All submissions are subject to a double blind peer review; if two of referees gives a negative feedback on a paper, the paper is being rejected. If two of referees gives a positive feedback on a paper and one referee negative, the editor can decide whether accept or reject. All submitted papers and referee reports are archived by journal Submissions whether they are published or not are not returned. Authors who want to give up publishing their paper in TUJE after the submission have to apply to the editorial board in written. Authors are responsible from the writing quality of their papers. TUJE journal will not pay any copyright fee to authors. A signed Copyright Assignment Form has to be submitted together with the paper.

PUBLICATION ETHICS

Our publication ethics and publication malpractice statement is mainly based on the Code of Conduct and Best-Practice Guidelines for Journal Editors. Committee on Publication Ethics (COPE). (2011, March 7). Code of Conduct and Best-Practice Guidelines for Journal Editors. Retrieved from http://publicationethics.org/files/Code%20of%20Conduct_2.pdf

PUBLICATION FREQUENCY

The TUJE accepts the articles in English and is being published 4 times (January, April, July and October) a year.

CORRESPONDENCE ADDRESS

Journal Contact: tuje@mersin.edu.tr

CONTENTS

Volume 3 – Issue 2

ARTICLES

Turkish Journal of Engineering

Turkish Journal of Engineering (TUJE)
Vol. 3, Issue 2, pp. 51-59, April 2019
ISSN 2587-1366, Turkey
DOI: 10.31127/tuje.433072
Research Article

INVESTIGATION OF MACHINABILITY PROPERTIES OF LASER TREATED S355JR CARBON STEEL WITH ZRB$_2$ NANOPARTICLES

Tuncay Şimşek *[1], Mustafa Bariş [2], Şadan Özcan [3,4] and Adnan Akkurt [5]

[1] Mersin University, Architecture Faculty, Department of Industrial Design, Mersin, Turkey
ORCID ID 0000-0002-4683-0152
tuncaysimsek@mersin.edu.tr

[2] Eti Maden Works General Management, Ankara 06010, Turkey
ORCID ID 0000-0002-2119-0697
mustafabaris@etimaden.gov.tr

[3] Hacettepe University, Faculty of Engineering, Department of Physical Engineering, Ankara, Turkey
[4] Hacettepe University, Division of Nanotechnology and Nanomedicine, Ankara,Turkey
ORCID ID 0000-0001-7966-1845
sadan@hacettepe.edu.tr

[5] Gazi University, Industrial Design Engineering, Ankara, Turkey
ORCID ID 0000-0002-0622-1352
aakurt@gazi.edu.tr

* Corresponding Author
Received: 11/06/2018 Accepted: 13/08/2018

ABSTRACT

In this study, the machinability properties of laser treated S355JR samples were investigated. The ZrB$_2$ nanoparticles were coated on the surface of S355JR carbon steel by 2 kW CO$_2$ laser. Then the coated samples were cut using the methods of abrasive water jet, wire-cut electrical discharge machining, laser, and abrasive disc, respectively. The phase structures and morphologies of the coated and cut surfaces were determined by using X-Ray diffractometry, optical microscope and scanning electron microscopy. The hardness was specified by using the microhardness device. It was found that low heat input and minimal damage was observed with the abrasive disc cutting method. Cutting with wire-cut electrical discharge machining, the worn zone was in a very narrow range, but there was also some heat-affected zone. While no heat input was seen in the method of cutting with abrasive water jet, significant damages in the shear edges and peripheral zones were observed due to abrasive particles. Intensive thermal deformation was also observed in the method of laser cutting.

Keywords: *Laser Coating, Nanoparticles, Machinability, Abrasive Water Jet, Wire-Cut Electrical Discharge Machining*

1. INTRODUCTION

Machining methods also develop as a result of developments in material technology. Machinability of new materials and traditional samples has been investigated for many years (Ozkul *et al.* 2013; Aouici *et al.,* 2014; Buldum *et al.,* 2012). Due to improperly selected methods, materials cannot fulfil their functions in critical processes and serious economic losses occur. Therefore, it is very important to determine the most appropriate cutting method for the produced materials. It is known that the high temperature materials such as TiC (Wang *et al.,* 2013), B_4C (Yibas *et al.,* 2015), WC (Pulsford *et al.,* 2018), SiC (Hashemi *et al.,* 2018), TiN (Zhang *et al.,* 2017), Al_2O_3 (Ruppi,, 2005), ZrC (Zhang *et al.,* 2018), TiB_2 (Han et al., 2018) etc. are coated on the base materials such as carbon and cold work steel (Pei *et al.,* 1996; Suresh *et al.,* 2018; (Sun et al., 2018), aluminum (Chi *et al.,* 2018), magnesium (Xu *et al.,* 2014), titanium alloys etc (Zhao *et al.,* 2018). The methods, such as self-propagating high temperature synthesis (SHS) (Masanta *et al.,* 2010), thermal spray coatings (Berger *et al.,* 2015), sol-gel (Tlili *et al.,* 2016), PVD (Lu *et al.,* 2018), and CVD (Liu *et al.,* 2018), reactive plasma spraying (Dai et al., 2017), are used intensively for coating of metals. Being one of these high temperature ceramics, zirconium diboride (ZrB_2) which has a melting temperature of 3245 ^{o}C, high hardness, oxidation resistance and thermal shock resistance, are mostly used in a wide area as diffusion barriers in the semiconductors, molten metal container, and ignition absorber in nuclear reactor cores (Fahrenholtz *et al.,* 2007; Sonber *et al.,* 2011; Baudis *et al.,* 1985). ZrB_2 nanoparticles can be obtained by using many different methods. Peters *et al.* (2009), obtained single phase ZrB_2 by grinding elemental Zr, and B powders in a Spex type high energy ball mill. Akgün *et al.* (2011), produced ZrB_2 using ZrO_2, Mg and B_2O_3 powders through mechanochemical method and volume combustion synthesis method. Setoudah *et al.* (2006), milled an elemental mixture of ZrO_2, B_2O_3 and Mg by using a laboratory scale mill under Ar atmosphere and synthesized a pure ZrB_2 with approximately 75 nm crystallite. Jalaly *et al.* (2013), obtained nanocrystal ZrB_2 from ZrO_2, B_2O_3 by magnesiothermic and aluminothermic reductions. Guo *et al.* (2009), produced ZrB_2 powders in the vacuum by boron/carbothermal reduction of ZrO_2, B_4C, and C. It is also seen that ZrB_2 significantly increases the wear and corrosion resistance when it coated on the material surfaces (Xue *et al.,* 2018; Zou *et al.,* 2017; Neuman *et al.,* 2017; Cheng *et al.,* 2017; Dangio *et al.,* 2018; Pourasad *et al.,* 2017).

Parts used in industries such as machine, manufacturing, space and automotive etc. deteriorate after a certain performance and mandatory changes in geometries are required. In the case of replacing high-cost parts with new ones, it is more economical to make some modification to these parts instead of replacing them. While, there are many studies about different coating metals such as steel, carbon steel, aluminum, copper, titanium alloys etc. in the literature, no study has been found especially about machinability of these coated materials. The properties of coated samples was lack to date. Considering this gap in literature, the S355JR carbon steel materials coated with ZrB_2 nanoparticles are subjected to micro cutting with widely used methods such as abrasive water jet, wire-cut electrical discharge machining, laser and abrasive disc cutting methods, respectively. Experimental studies have been focused on determination of how the coating layer is affected by these processes than the cut surface. In the present study, the mechanochemical synthesis method was preferred as the synthesis method because of the advantages such as occurrence of the reaction at room temperature, being an economical method, great flexibility in the selection of the processing parameters, ability to produce large quantities of material with the same physical properties and offering the possibility of producing compounds which cannot be produced by using conventional methods (Avar *et al.,* 2015; Simsek *et al.,* 2017). Synthesized ZrB_2 nanoparticles are coated with CO_2 laser after determining the optimum parameters on the surface of S355JR (St52) carbon steel materials. Besides its wide usage area in many fields such as aviation, automotive and manufacturing industries, its poor wear properties were effective in the selection of the base material. As coating method, laser coating method is chosen due to its important advantages which allows to obtain hard, protective, abrasion and corrosion resistant coating on the surfaces of metals. By utilizing superior properties of the laser beam; hard, homogenous, non-porous, crack-free coatings with high wear resistance can be obtained on the surfaces by melting a thin layer on the substrates surface. The ideal cutting (machining) method for samples coated with ZrB_2 nanoparticles was investigated in detail. The cut samples were examined by using optical and SEM microscopy and X-Ray diffractometry without any treatment. Hardness of coated and cut surfaces were determined.

2. EXPERIMENTAL STUDIES

2.1. Materials

Mechanochemically synthesized ZrB_2 nanoparticles were used as the coating material. ZrB_2 nanoparticles were obtained by milling Zr (873.05 µm, ≥ 99, Sigma Aldrich), Mg (138.66 µm, ≥99.00%, Sigma Aldrich), and B_2O_3 (545.74 µm, ≥98.00%, Eti Maden) under Ar atmosphere in a high energy ball mill (Fritch, P6) for 30h. The powder mixture consisting of MgO and ZrB_2 phases after 30h ball milling was purified with acetic acid (AA, CH_3COOH) solution, dried under vacuum, and then used in the coating applications. The detailed synthesis procedures of ZrB_2 nanoparticles are presented in (Simsek 2014).

2.2. Laser Coating and Machinability Experiments

S355JR carbon steel was used as the substrate material in the coating experiments. Table 1 shows the chemical composition of S355JR carbon steel.

Table 1. Chemical composition of S355JR carbon steel

Chemical Composition (wt %)	C	Si	Mn	P	S	Cu	N	Fe
	0.22	0.55	1.60	0.035	0.035	0.55	0.09	Bal.

The size of the base material used was 100 (length) X 15 (width) X 4 (thickness) mm. Prior to laser cladding, the samples were sandblasted and cleaned with acetone and ethanol. Firstly, the nanoparticles were coated on the surface of carbon steel with a thickness of 50 µm and all precoating processes were carried out in the vacuum. Then, the layers were heated up to 400 oC under Ar atmosphere for 4 hours to make good bond to substrate and convert the phenolic resin to carbon (Yilbas et al., 2011). This carbon film provides hard wear resistant carbide phases on the surface. This process was done very carefully because if the precoating was not done well, some problems was encountered such as adhesion to the substrate, inhomogeneity and porosity (Yilbas et al., 2012; Simsek et al., 2017). Secondly, the precoated layers were laser clad by a 2 kW CO2 laser (Amada, LC-2415 α III, Japan) at continuous-wave mode under N_2 gas atmosphere. Table 2 shows the laser coating parameters.

Table 2. Laser coating parameters

Laser power	W	2000
Power density	W/mm^2	181
Frequency	Hz	1000
Scanning rate	mm/s	5
Average power	W	160
Laser wave length	Mm	10.64
N_2 pressure	kPa	600

Fig. 1. shows the schematic view of laser cladding process and nozzle used. The coating experiments were conducted between 75-200 W laser powers under N_2 atmosphere. It is noticed that the higher and lower laser power usage resulted in very intensive cracks and pores. Due to obtaining homogenous distribution of nanoparticles without fractures and cracks, the samples of 160 W of laser power was used in the machinability experiments.

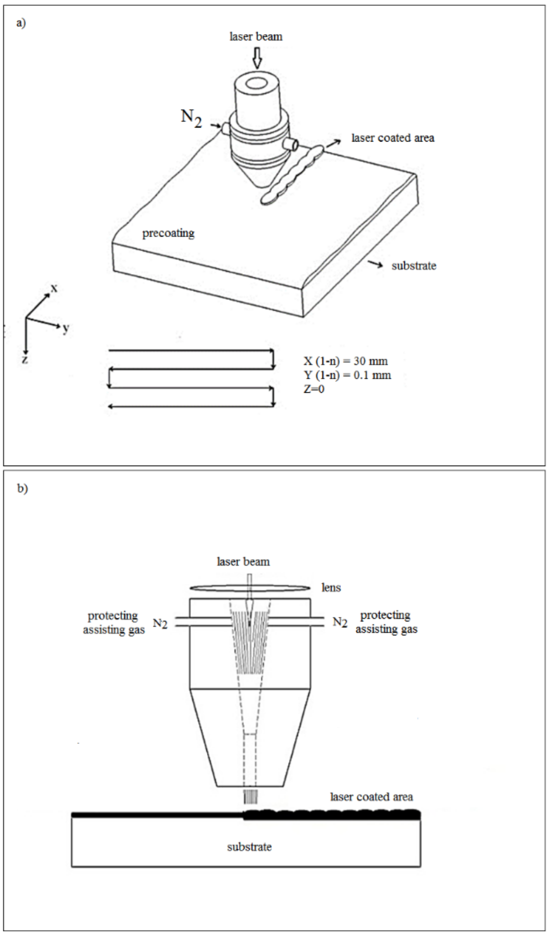

Fig. 1. Schematic view of a) laser coating process b) nozzle (Simsek 2014).

Machinability properties of the samples in respect of cutting methods were determined by cut with abrasive water jet (KMT, SLV-E50), wire-cut electrical discharge machining (Makino, Dou 43), laser (Amada, Lasmac LC-2415 α III), and abrasive disk (BMS, Bulucut-3), respectively. Table 3 shows the applied cutting parameters.

Table 3. Parameters applied in cutting tests

Abrasive water jet cutting		*Laser cutting*	
Nozzle Diameter	0.75 mm	Laser Power	2000 W
Sand Flow Rate	250 g/min	Cutting Speed	1000 mm/min
Pressure	4000 bar	Frequency	1000 Hz
Feed rate	150 mm/min	Duty	55 %
		Average Power	880 W
Wire-cut electrical discharge machining		*Abrasive disc cutting*	
Wire Diameter	0.3 mm	Disc Used	SiC
Wire Type	CuZn	Disc Sizes	250x32x1.6 mm
Wire Speed	6 m/min	Revolutions Speed	2840 rpm
Cutting Speed	11 mm/min	Feed rate	1 mm/s
Tension	10 cN	Cutting System	Automatic
Time of Energy Given	18 ms	Cooling	Cooling with fluid
Time of Energy Cut	70 ms		

2.3. Characterization

The phase structures of the coating layers were determined by XRD (Rigaku D/MAX-2200) with CuKα (λ=1.5408 ºA) radiation by selecting 40 kV operating voltage and 30 mA current, 2θ angle range 2-90°, and 4°/min scanning rate. The average crystallite size of the nanoparticles were calculated with Scherrer Equations [Eq.1], where τ is the crystallite size, K is the constant taken depending on the shape of crystal (0.89), λ is the wavelength of X ray (0.154 nm), β is the width of half-length of peak (FWHM), and θ is Bragg angle. In the calculation of crystallite size, FWHM values of (100) peak in XRD patterns were determined by graphic analysis using JADE 7.0 XRD analysis program.

$$\tau = \frac{K \, . \, \lambda}{B \, . \, Cos \, \theta} \qquad (1)$$

Microstructural examinations of the surface and cross-sections of the samples were characterized by scanning electron microscope (FEI Quanta 200F) and optical microscope (Leica M205 C). The hardness of samples was determined by using a Vickers hardness tester (Shimadzu HMV-2) under 50 g load for 15 s.

.

3. RESULTS AND DISCUSSION

As coating material ZrB_2 nano particles were used. XRD graphs of synthesized and purified nanoparticles are given in Fig. 2. The crystallite size of the purified nanoparticles was calculated as 20.45 nm by Scherrer formula. The powder mixtures of MgO and ZrB_2 were purified with hot acetic acid leaching and following to purification processes, ZrB_2 nanoparticles were carefully precoated on carbon steel and coated with a CO2 laser at 160 W laser power (Simsek 2014).

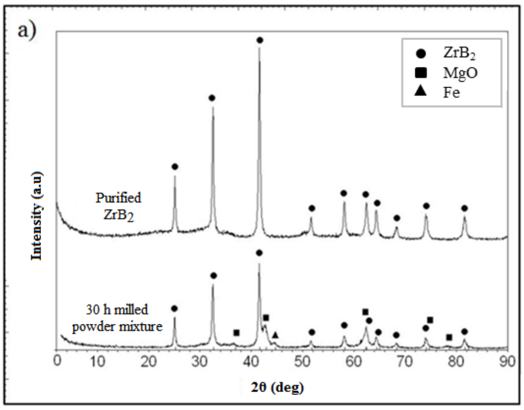

Fig. 2. XRD graph of the ZrB_2 nanoparticles (Simsek 2014).

Fig. 3. shows the SEM and optic images of the coated sample surfaces and the cross-sections. Homogeneous, nonporous and crack-free layers with good metallurgical bonding to substrate can be seen from Fig. 3. The thickness of layers was around 24 µm while the heat affected zone was around 60 µm

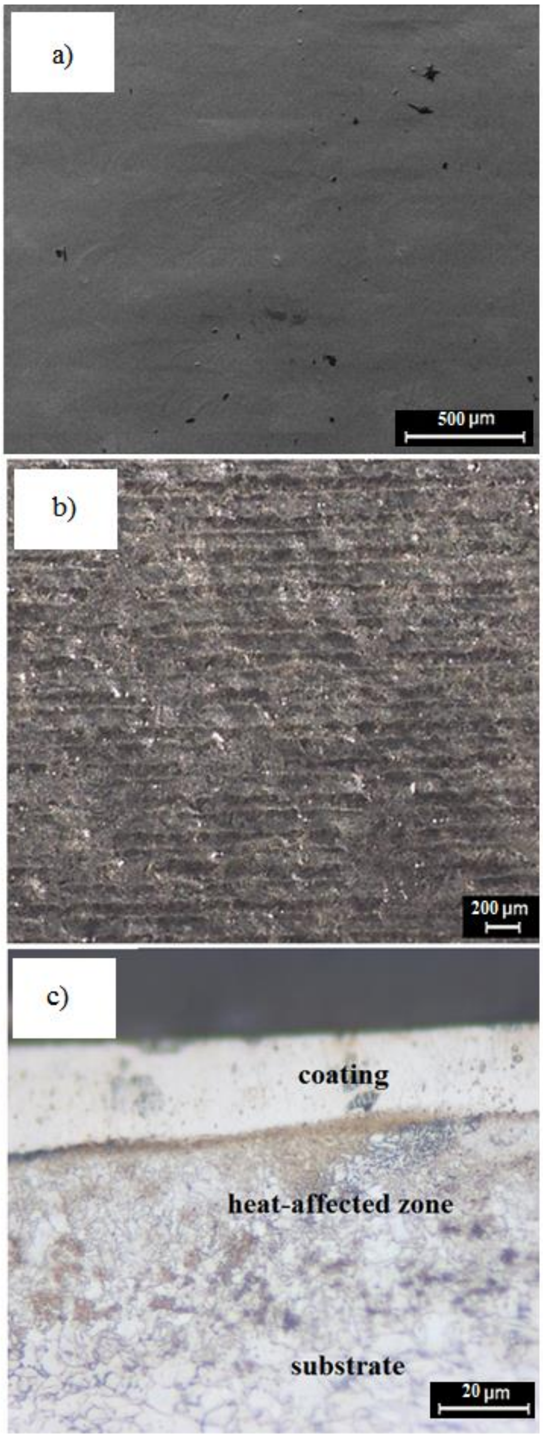

Fig. 3. a) Surface view (SEM), b) Surface view (optical microscope), c) Cross-section view (optical microscope) (Simsek 2014).

The phase structures were identified by X-Ray diffractometry. Fig. 4a shows the XRD analysis and hardness profiles of the coating layers obtained at 160 W laser power (Simsek 2014, Simsek 2017). $ZrN_{0.4}B_{0.6}$, Fe_3C and $FeN_{0.0760}$ $Zr_7O_8N_4$ phases were observed on the surfaces of the coating layers. Nitride phases were formed with the reaction of assisting–protecting N_2 gas at high temperatures while the carbide phase occurred with the reaction of carbon film formed on the substrate (Fig. 4a).

The same results were also observed by Yilbas et al. studies. They reported in their laser cladding experiments that N_2 gas resulted to formation of nitride phases on the substrate (Yilbas et al, 2012). Microhardness tests were performed for determining the hardness of the coating surface. Fig. 4b. represents the average hardness value of 5 measurements were taken from the every region of coating layers. It can be seen from Fig. 4b. that the hardness was about 220 HV, 600 HV, and 900 HV for substrate, heat–affected zone and coatings layers, respectively. It is noticed that the formation of Fe, Zr-rich carbide, boride and nitride phases substantially increased the coating layers hardness.

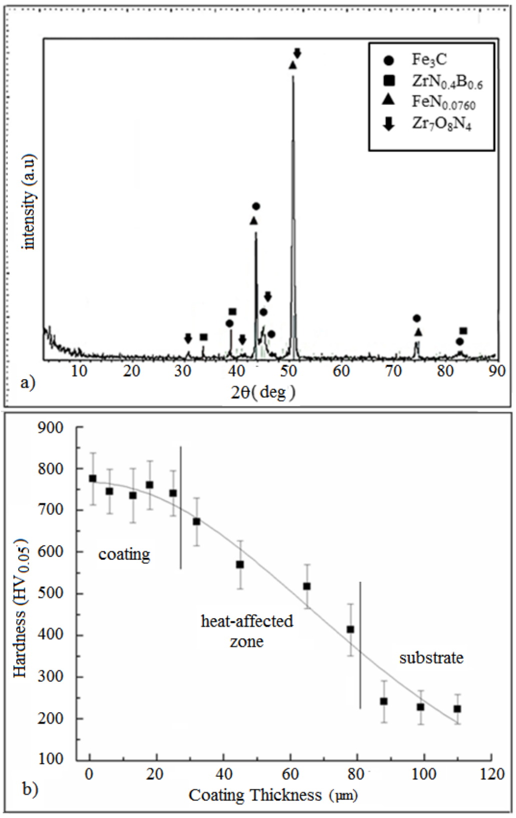

Fig. 4. a) XRD pattern of coating, b) Regional cross-section hardness values of the coated samples

Furthermore, in order to examine the regional structure properties of the coating layer, the heat-affected zone and base metal, the coated sample was left in liquid nitrogen for 10 minutes and then broken. Fig. 5. shows SEM images of the cross-sections of the fracture samples. When the images were examined, it was determined that a transition region was formed between the coating layer and the heat-affected zone, the structures of coating layer (a), heat-affected zone (b) and base metal (c) were different from each other due to the applied high heat. As a result of the high temperature releasing during the laser coating, columnar structures were observed in the hardened coating layer due to the rapid cooling; whereas, brittle ruptures in the coating layer and ductile fractures from transition region to the base metal after the fracture were observed (Simsek 2014).

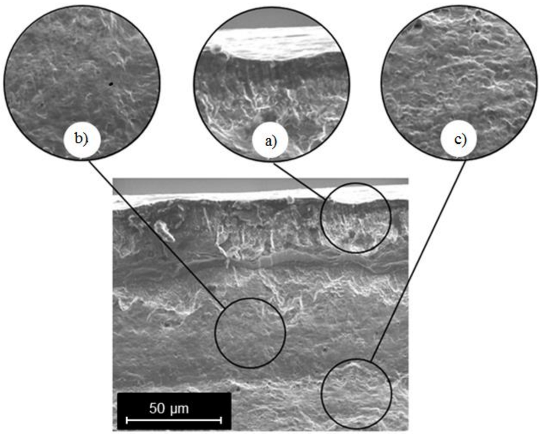

Fig. 5. SEM image of the structures released a result of the fracture of the coated samples in liquid nitrogen

After microstructural analysis of coated layer, the machinability performance of coated S355JR carbon steel layers were investigated with cutting the layers by advanced manufacturing methods such as abrasive water jet, wire-cut electrical discharge machining, laser and abrasive disc. Fig. 6. and 7 shows the optical microscope and SEM images of the samples cut with abrasive water jet, wire–cut electrical discharge machining, laser and abrasive disc, respectively. The cut samples were examined carefully and the deformations made by the methods on the coating layers were determined. When the optical microscope and SEM images of the cutting regions of S355JR carbon steel surface were evaluated; destructions of ~200 µm in cutting with abrasive water jet, ~150 µm in cutting with laser beam, ~25 µm in cutting with wire-cut electrical discharge machining and ~10 µm in cutting with abrasive disc were observed (Simsek, 2014). It is known that cutting process can be achieved with high pressure hydro-abrasive jet in water–jet system. Firstly, the pump generates a flow of pressurized water and granular abrasive is drawn into the water stream. In order to form and stabilize, the mixture of water and abrasive particles passes through the nozzle and directed to the surface of materials. With stream of this high pressure hydro–abrasive jet toughest materials can be cut successfully. The quality of cut layers are depending on the machining parameters such as water pressure, traverse speed, abrasive flow rate, and standoff distance etc. (Kumar et al., 2017; Uthayakumar et al., 2016; Hajdarevic et al., 2015). The parameters of cutting is given in Table 3. Jet-splashes are inevitable in the abrasive water jet cutting process (including uncoated specimens) by the use of thin water jets under high pressure with added abrasive slurry. These jet-splashes are scattered on the surface of the jet hit, backwards or backwards at a certain angle. Because of this situation, the coating layer has deformed significantly. At the cut surfaces, it was found that the roughness of the surface increased in the cutting area, and large peaks and valleys was appeared on the surfaces (Fig. 7a.) It was also observed that all the samples obtained had significant damage in the shear edges and peripheral zones of coating layer and the abrasive particles in the mixed state with water were buried from the coating layer to the next transition zone even in far distances. This is an expected situation, so it has been determined that cutting of nanoparticle coated materials with an abrasive water jet will not be an appropriate choice. The surface of samples cut with laser was significantly affected by the heat. The irregularity in the coating thickness on the shear edge surface increased compared to other cutting methods and a certain amount of loss (along with the evaporation and molten sub-metal) was observed from the coating material. Surface cracks are also another major problem due to high heat input and sudden cooling during cutting of the samples with laser. In addition, it has been found that the formation of droplet due to melting of main material and coating material causes a substantial damages of the cut surface geometry (Bouzakis et al., 2017; Siebert et al., 2014). It has been determined that laser cutting should not be preferred in the processing of the surfaces coated with nanoparticles, even though its use in micro processing methods is getting widespread every day. However, when the obtained data's were evaluated, it is a more acceptable method than the abrasive water jet.

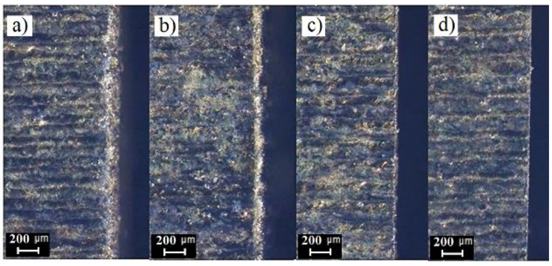

Fig. 6. Optical microscope (X100) images of the ZrB_2 coated samples after cutting processes; a) Abrasive water jet, b) Laser, c) Wire–cut electrical discharge machining, d) Abrasive disc

When the cut zones of samples obtained through wire-cut electrical discharge machining method were examined, it was observed that the coating, transition zone and substrate were affected by heat in a more limited way but there were even small amounts of residues (burr) on the cutting surface (Puri et al., 2005; Hascalik et al., 2004). By usage of cutting fluid in the process of cutting with abrasive disc, the heat effect was minimized when compared to wire-cut electrical discharge machining and smother shear edge was obtained.

The microhardness of cut layers are given in Fig. 8. Microhardness measurement of the cross-section of the cut samples were carried out after sample preparation procedures like polishing and etching. As a result of the sample preparation procedures, it was observed that the destruction zones caused by the cutting methods were eroded, so that the measurements were taken from the inner regions of the samples and it is observed that the microhardness values were very close to each other (Fig. 8). While damage occurred in laser and wire–cut electrical discharge machining cutting among thermal cutting methods due to heat, the effect of abrasive grains and the pressurized water was in question in abrasive water jet. Although there was no damage in cutting with abrasive water jet due to heat, abrasive grains deformed the cutting zone severely as a result of their random scatterings on the coating surface. The results showed that the method of cutting with abrasive disc was the most suitable cutting method in the positions where the machining capability is suitable but the wire-cut electrical discharge machining method should be preferred in the complicated geometric samples for which abrasive disc could not be used.

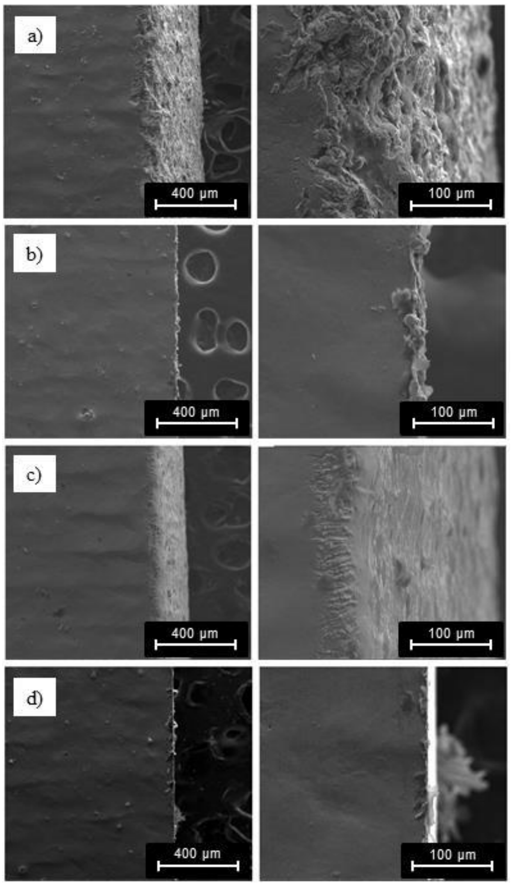

Fig. 7. SEM (X800) images of ZrB_2 coated samples after the cutting process; a) Laser beam b) Abrasive water jet, c) Wire – cut electrical discharge machining, d) Abrasive disc

When an overall evaluation was made, it was observed that processes of cutting with laser beam (due to thermal effect) and abrasive water jet (due to the impact of abrasive particles having random distribution in water) caused severe destruction on the coating layer. However, a small amount of damage was determined due to the thermal effect in method of cutting with wire-cut electrical discharge machining. It was found that minimum damage was seen in process of cutting with abrasive disc. Structural deformations were observed in a wide region due to heat dissipation as well as thin cracks and fractures on the surface caused by sudden high heat input and sudden cooling in the process of cutting with laser. In the method of cutting with wire-cut electrical discharge machining, there were smaller cracks and fractures related to heat on the surface. In addition, a much smaller region was affected by heat compared to the laser, and consequently structural deformations remained limited. There was no thermal deformation in the method of cutting with abrasive water jet since there was no heat input but as a result of were observed on the coating surface with the abrasive particle penetration. Cutting with abrasive random splashes of water-abrasive mixture on the surface at the beginning of the cutting process, significant ruptures on the coating surface and great amount of physical deformations disc was determined as the most efficient method among these methods.

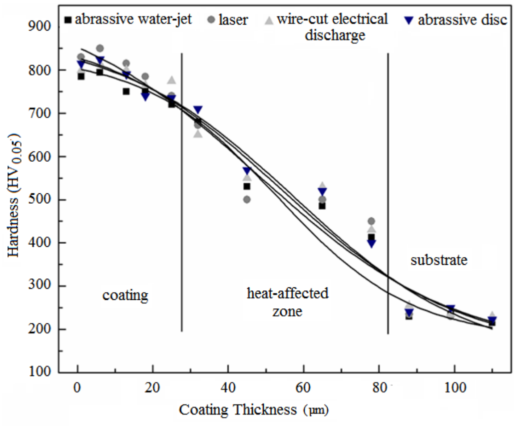

Fig. 8. Comparison of regional hardness values of ZrB_2 coated samples after cutting processes depending on the cutting method

4. CONCLUSIONS

The machinability of ZrB_2 nanoparticles coated S355JR carbon steel layers were investigated in the present study. 2 kW CO_2 laser with 2000 W power was operated at continuouswave mode was used for the laser coating applications. The layers without cracks and porosity obtained with 160 W laser power were used as specimen for cutting operations. The laser coated layers were cut with abrasive water jet cutting, wire-cut electrical discharge machining, laser and abrasive disc, respectively. The microstructural, morphological and phase structures were determined by using optic microscopy, scanning electron microscopy and X-Ray diffractometry. The findings are,

- When the coating area was evaluated in respect of machinability applications, minimal damage and the best surface properties were achieved in the method of cutting with abrasive disc.
- It was determined that abrasive water jet cutting should not be used for nanoparticle coated surfaces unless it is necessary. Random splashes of water-abrasive mixture on the surface at the beginning of the cutting process, significant ruptures on the coating surface and great amount of physical deformations occur on the coated layers surfaces. When the damage on the cutting surface was evaluated, it was determined that the method causing maximum damage in the coating layer was the abrasive water jet.
- Laser cutting method is also not suitable for cutting of this kind of coatings, due to a certain amount of loss (along with the evaporation and molten sub-metal) from the coating material and surface cracks due to high heat input and sudden cooling during cutting of the samples. In addition, it has been also seen that the formation of droplet due to melting of main material and coating material causes a substantial damages of the cut surface geometry.
- When the cut zones of samples obtained through wire-cut electrical discharge machining method were examined, it was observed that the coating, transition zone and substrate were affected by heat in a more limited way but there were even small amounts of residues (burr) on the cutting surface. Beyond its disadvantages, it is seen that thermal methods like laser and wire-cut electrical discharge machining, also minimize the rupture tendency of the coating from the substrate
- In the process of cutting with abrasive disc, by usage of cutting fluid the heat effect was minimized and smother shear edge was obtained.
- Microstructural investigations of the cutting regions of S355JR carbon steel surface were revealed the destructions of ~200 µm in cutting with abrasive water jet, ~150 µm in cutting with laser, ~25 µm in cutting with wire-cut electrical discharge machining and ~10 µm in cutting with abrasive disc.
- It was seen that cutting methods generally did not cause a significant change in hardness of cut layers, but even with small differences, the highest hardness occurred in the cutting made by laser beam and the lowest hardness occurred in the cutting with abrasive water jet. The hardness of cut layers were varied in the range of 780-865 HV.

ACKNOWLEDGEMENTS

The authors would like to thank Development of Technology Department, Eti Maden Works General Management for laboratory facilities.

REFERENCES

Akgün, B., Çamurlu, H.E., Topkaya, Y., Sevinç, N. (2011). “Mechanochemical and volume combustion sythesis of ZrB_2.” *International Journal of Refractory Metals and Hard Materials,* Vol. 29, pp. 601-607

Aouici, H., Bouchelaghem, H. Yallese, M. A., Elbah, M., Fnides, B. (2014) “ Machinability investigation in hard turning of AISI D3 cold work steel with ceramic tool using response surface methodology.” *International Journal of Advanced Manufacturing Technology,* Vol.73, pp. 1775–1788.

Avar, B., Ozcan, Ş. (2015). “Characterization and amorphous phase formation of mechanically alloyed Co60Fe5Ni5Ti25B5 powders.” *Journal of Alloys and Compounds* Vol. 650, pp. 53-58.

Baudis, U., Fitchte, R. (1985). Boric oxide and boric acid and borates, Schwetz, KA, Lipp A, Capbll FT, Pfefferkom R(Eds.). Boron carbide, boron nitride, and metal borides, Zirconium and zirconium compounds, Ullmann's Encyclopedia of Industrial Chemistry, Fifth, Completely Revised Edition A4, Wiley-VCH, Weinheim, 263-307, 91.

Berger, L.M. (2015). “Application of hardmetals as thermal spray coatings*.” International Journal of Refractory Metals and Hard Materials,* Vol. 49, pp. 350–364.

Buldum, B.B., Şık, A., Ozkul, I. (2012). "Investigation of Magnesium Alloys Machinability." *International Journal Of Electronics; Mechanical And Mechatronics Engineering,* Vol.2, pp. 261-268.

Bouzakis, K.D., Charalampous, P., Kotsanis, T., Skordaris, G., Bouzakis, E., Denkena, B., Breidenstein, B., Aurich, J.C., Zimmermann, M., Herrmann, T., M'saoubi R. (2017). "Effect of HM substrates' cutting edge roundness manufactured by laser machining and micro-blasting on the coated tools' cutting performance." *CIRP Journal of Manufacturing Science and Technology, Vol.* 18, pp. 188–197.

Cheng, E. J., Li., J., Sakamoto, Y.., Han, S., Sun, H., Noble, J., Katsui, H., Goto, T. (2017). "Mechanical properties of individual phases of ZrB_2-ZrC eutectic composite measured by nano indentation." *Journal of the European Ceramic Society,* Vol. 37, pp. 4223-4227.

Chi, Y., Gu, G., Yu, H., Chen, C. (2018). "Laser surface alloying on aluminum and its alloys: A review." *Optics and Lasers in Engineering,* Vol. 100, pp. 2337.

Dangio, A., Zoua, J., Binner, J., Ma, H.B., Hilmas, G.E., Fahrenholtz, W.G. (2018). "Mechanical properties and grain orientation evolution of zirconium diboride-zirconium carbide ceramics." *Journal of the European Ceramic Society,* Vol. 38, pp. 391-402.

Dai, X., Yan, D., Yang, Y., Chu, Z., Chen, X., Song, J. (2017). "In situ $(Al,Cr)_2O_3$-Cr composite coating fabricated by reactive plasma Spraying." *Ceramic International,* Vol. 43, pp. 6340-6344.

Fahrenholtz, W.G., Hilmas, G.E. (2007). "Refractory Diborides of Zirconium and Hafnium", *Journal of American Ceramic Society, Vol.* 90(5), pp. 1347-1364.

Hascalik, A., Caydas¸ A. (2004). "Experimental study of wire electrical discharge machining of AISI D5 tool steel." *Journal of Materials Processing Technology*, Vol. 148, pp. 362–367.

Hashemi, S.H., Shoja-Razavi, R. (2016). "Laser surface heat treatment of electroless Ni–P–SiC coating on Al356 alloy." *Optics and Laser Technology,* Vol. 85, pp. 1–6.

Han, Y.G., Yang, Y., Wang, L., Chen, X.G., Chu, Z.H., Zhang, X.N., Dong, Y.C., Liu, Z., Yan, D.R. Zhang, J.X., Li, C.G. (2018). "Microstructure and properties of in-situ TiB_2 matrix composite coatings prepared by plasma spraying." *Applied Surface Science,* Vol. 431, pp. 48-54.

Hajdarevic, D. B., Cekic, A., Mehmedovic, M., Djelmica, A. (2015). "Experimental Study on Surface Roughness in Abrasive Water Jet Cutting." *Procedia Engineering* Vol. 100, pp. 394 – 399.

Jalaly, M,, Bafghi, M.Sh., Tamizifar, M., Gotor, F.J. (2013). "Mechanosynthesis of nanocrystalline ZrB_2-based powders by mechanically induced self-sustaining reaction method." *Advanced in Applied Ceramics,* Vol. 112 (7), pp. 383-388.

Guo, W.M., Zhang, G.J. (2009). "Reaction Processes and Characterization of ZrB_2 Powder Prepared by Boro/Carbothermal Reduction of ZrO_2 in Vacuum." *Journal of the American Ceramic Society,* Vol. 92, pp. 264–267.

Kumar, A., Singh, H., Kumar, V. (2017). "Study the parametric effect of abrasive water jet machining on surface roughness of Inconel 718 using RSM-BBD techniques." *Materials and Manufacturing Processes,* pp. 1-7.

Liu, C., Liu, Z., Wang, B. (2018). "Modification of surface morphology to enhance tribological properties for CVD coated cutting tools through wet micro-blasting post-process." *Ceramic International,* Vol. 44, pp. 3430-3439.

Lu, C., Yao, J.W., Wang, Y.X., Zhu, Y.D., Guo, J.H., Wang, Y., Fu, H.Y., Chen, Z.B., Yan, M.F. (2018) "A novel anti-frictional multiphase layer produced by plasma nitriding of PVD titanium coated ZL205A aluminum alloy." *Applied Surface Science,* Vol. *431,* pp. 32-38.

Masanta, M., Ganesh. P., Kaul, R., Choudhury, A.R. (2010). "Microstructure and mechanical properties of TiB_2–TiC–Al_2O_3-SiC composite coatings developed by combined SHS, sol–gel and laser technology." *Surface and Coatings Technology,* Vol. 204, pp. 3471–3480.

Neuman, E.W., Hilmas, G.E., Fahrenholtz, W.G. (2017). "Processing, microstructure, and mechanical properties of zirconium diboride-boron carbide ceramics." *Ceramic International,* Vol. 43, pp. 6942-6948.

Ozkul, I., Buldum, B.B., Akkurt, A. (2013). "Machinabilty of Sleipner Cold Work Steel With Wire Electro Discharge Machining". *International Journal Of Electronics; Mechanical And Mechatronics Engineering,* Vol.2, pp. 252-260

Pulsford, J., Kamnis, S., Murray, J., Bai1, M., Hussain, T. (2018). "Effect of Particle and Carbide Grain Sizes on a HVOAF WC-Co-Cr Coating for the Future Application on Internal Surfaces: Microstructure and Wear." *Journal of Thermal Spray Technology,* Vol. 27, pp. 207–219.

Pei, Y.T., Ouyang, J.H, Lei, T.C. (1996). "Laser cladding of ZrO_2-(Ni alloy) composite coating." *Surface and Coatings Technology*, Vol. 81, pp. 131-135.

Peters, J.S., Cook, B.A., Harringa, I., Russell, A.M. (2009). "Erosion resistance of TiB_2-ZrB_2 composites." *Wear,* Vol. 267, pp. 136-143.

Pourasad, J., Ehsani, N. (2017). "In-situ synthesis of SiC-ZrB_2 coating by a novel pack cementation technique to protect graphite against oxidation." *Journal of Alloys and Compounds,* Vol. 690, pp. 692-698.

Puri, A.B., Bhattacharyya, B. (2005). "Modeling and analysis of white layer depth in a wire-cut EDM process through response surface methodology." *International Journal of Advanced Manufacturing Technology,* Vol.25, pp. 301–307.

Ruppi, S. (2005). “Deposition, microstructure and properties of texture-controlled CVD a-Al_2O_3 coatings.” International *Journal of Refractory Metals and Hard Materials*, Vol. 23, pp. 306–316.

Siebert, R., Schneider, J., Beyer, E. (2014). “Laser Cutting and Mechanical Cutting of Electrical Steels and its Effect on the Magnetic Properties.” *Ieee Transactions On Magnetics,* Vol. 50 (4), 2001904-2001908.

Suresh, S., Rangarajana, S., Bera, S., Krishnan, R., Amirthapandian, S., Sivakumar, M., Velmurugan, S. (2018). “Evaluation of corrosion resistance of nano nickel ferrite and magnetite double layer coatings on carbon steel.” *Thin Solid Films,* Vol. 645, pp. 77-86.

Sun, C., Xue, Q., Zhang, J., Wan, S., Tieu, A.K., Tran, B.H. (2018). “Growth behavior and mechanical properties of Cr-V composite surface layer on AISI D3 steel by thermal reactive deposition.” *Vacuum,* Vol. 148 pp. 158-167

Sonber, J.K., Suri, A.K. (2011). “Synthesis and Consolidation of Zirconium Diboride: Review.” *Advances in Applied Ceramics, Vol.* 110 (6), pp. 321-334.

Setoudeh, N., Welham, N.J. (2006). “Formation of zirconium diboride (ZrB_2) by room temperature mechanochemical reaction between ZrO_2, B_2O_3 and Mg.” *Journal of Alloys and Compounds,* Vol. 420, pp. 225-228.

Şimşek, T. (2014). Investigation of The Zirconium Diboride Nanocrystal Coated Different Materials Mechanic and Mechinability Properties. Ph. D. Thesis, University of Gazi, Ankara, Turkey.

Simsek, T., Baris, M., Chattoopahyay, A. K., Ozcan, S., Akkurt, A. (2017). Surface Treatment of S355JR Carbon Steel Surfaces with ZrB_2 Nanocrystals by CO_2 Laser.” *Transactions of the Indian Institute of Metals,* Vol. 71, pp. 1885-1896.

Simsek, T., Baris, M., Kalkan, B. (2017). “Mechanochemical processing and microstructural characterization of pure Fe2B nanocrystals.” *Advanced Powder Technology,* Vol. 28 (11), pp. 3056-3062.

Tlili, B., Barkaoui, A., Walock, M. (2016). “Tribology and wear resistance of the stainless steel. The sol–gel coating impact on the friction and damage.” *Tribology International,* Vol. 102, pp. 348-354.

Uthayakumar, M., Khan, M.A., Kumaran, S.T., Slota, A., Zajac, J. (2016). “Machinability of Nickel-Based Super alloy by Abrasive Water Jet Machining.” *Materials and Manufacturing Processes,* Vol. 31 (13), pp. 1733-1739.

Wang, X.H., Pan, X.N., Du, B.S., Li, S. (2013). “Production of in situ TiB2+TiC/Fe composite coating from precursor containing B4C-TiO2-Al powders by laser cladding.” *Transactions of Nonferrous Metals Society of China,* Vol. 23, pp. 1689-1693.

Xu, J., Zou, B., Fan, X., Zhao, S., Hui, Y., Wang, Y., Zhou, X., Cai, X., Tao, S., Ma, H., Cao, X. (2014). “Reactive plasma spraying synthesis and characterization of TiB_2–TiC–Al_2O_3/Al composite coatings on a magnesium alloy.” *Journal of Alloys and Compounds,* Vol. 596, pp. 10–18

Xue, C., Zhou, H., Hu, J., Wang, H., Xu, J., Dong, S. (2018) “Fabrication and microstructure of ZrB_2–ZrC–SiC coatings on C/C composites by reactive melt infiltration using ZrSi2 alloy.” *Journal of* Advanced *Ceramics,* Vol. (7), pp. 64-71.

Yilbas, B.S., Karatas, C., Karakoc, H., AbdulAleem, B.J., Khan, S., Al-Aqeeli N. (2015). “Laser surface treatment of aluminum based composit mixed with B_4C particles.” *Optics and Laser Technology,* Vol. 66, pp. 129–137.

Yilbas, B.S., Akhtar, S.S., Karatas, C. (2011). “Laser carbonitriding of alumina surface.” *Optics and Lasers in Engineering, Vol.* 49, pp. 341–350.

Yilbas, B.S., Al-Aqeeli N, Karatas, C. (2012). “Laser control melting of alümina surfaces with presence of B_4C particles.” *Journal of Alloys and Compounds,* Vol. 539, pp. 12-16.

Zhang, M., Araez, N.G. (2017). “A sol–gel route to titanium nitride conductive coatings on battery materials and performance of TiN-coated LiFePO4.” *Journal of Materials Chemistry A,* Vol. 5, pp. 2251-2260.

Zhang, Y., Wang, H., Li, T., Fu, Y., Ren, J. (2018). “Ultra-high temperature ceramic coating for carbon/carbon composites against ablation above 2000 K.” *Ceramic International,* Vol. 44, pp. 3056-3063.

Zhao, X., Zhang, P., Wang, X., Chen, Y., Liu, H., Chen, L., Sheng, Y., Li, W. 2018). “In-situ formation of textured TiN coatings on biomedical titanium alloy by laser irradiation.” *Journal of the Mechanical Behavior of Biomedical Materials,* Vol. 78, pp. 143-153

Zou, J., Rubio, V., Binner, J. (2017). “Thermo ablative resistance of ZrB_2-SiC-WC ceramics at 2400 ^{o}C.” *Acta Materialia, Vol.* 133, pp. 293-302.

Turkish Journal of Engineering

Turkish Journal of Engineering (TUJE)
Vol. 3, Issue 2, pp. 60-67, April 2019
ISSN 2587-1366, Turkey
DOI: 10.31127/tuje.452921
Compilation Article

ANTIBIOTIC APPLICATIONS IN FISH FARMS AND ENVIRONMENTAL PROBLEMS

Tolga Bahadır *[1], Hakan Çelebi [2], İsmail Şimşek [3] and Şevket Tulun [4]

[1] Aksaray University, Engineering Faculty, Environmental Engineering Department, Aksaray, Turkey
ORCID ID 0000-0001-9647-0338
tolgabahadir61@gmail.com

[2] Aksaray University, Engineering Faculty, Environmental Engineering Department, Aksaray, Turkey
ORCID ID 0000-0002-7726-128X
hakanaz.celebi@gmail.com

[3] Aksaray University, Engineering Faculty, Environmental Engineering Department, Aksaray, Turkey
ORCID ID 0000-0003-1950-5159
ismailsimsek83@hotmail.com

[4] Aksaray University, Engineering Faculty, Environmental Engineering Department, Aksaray, Turkey
ORCID ID 0000-0002-0570-7617
sevkettulun@gmail.com

* Corresponding Author

Received: 13/08/2018 Accepted: 12/09/2018

ABSTRACT

Today, fish farming creates significant impacts on water resources and food chain from a global perspective, as compared to those of the other agricultural activities. Some methods and chemicals heavily using production and consumption periods in fish farming are related to the environmental damages. Chemicals have a common usage in both the world and our country to protect the products from the negative effects of diseases. They are also imposed to increase the production. As Turkey has significant potential in fish farming in comparison to many other countries in the world, there is a wide use of antibiotics in production. This research examines the use of antibiotics in fish farming to shed light on the effects of chemicals on the production and human health.

Keywords: *Antibiotic, Fish Farming, Environmental Factor, Aquaculture*

1. INTRODUCTION

Environmental pollution is defined as the deterioration of the natural balance of the ecosystem by various pollutants emerging as a result of human activities (Karaman, 2006). Therefore, in order to be able to eradicate the pollution, scientific studies are being carried out at the international level (Orçun and Sunlu, 2007). Scientific studies on this issue investigate the imbalance related to the ecology in different ways and suggest solutions (Karaman, 2006). In particular, fish farms need to be monitored in terms of unconscious and irregular chemical usage (drugs and antibiotics, disinfectants etc.) and in parallel with this, in terms of formation of environmental pollution. Antibiotics are substances produced by microorganisms that can destroy or inhibit the growth of other microorganisms. At the present time, antibiotics are not only used as a drug for humans. It is also broadly used in livestock breeding and fish farming. Some of the microorganisms that cause health problems in fish farms include *Mycobacterium marinum, Nocardia spp., Edwardsiella tarda, Vibrio vulnificus, Vibrio vulnificus, Vibrio parahaemolyticus, Streptococcus iniae, Lactococcus garviae, Micrococcus lylae, Aeromonas hydrophila, Plesiomonas shigelloides, Erysipelotrix insidiosa, Escherichia coli, Salmonella spp., Raoultella ornithinolytica, Pseudomonas spp., Leptospira icterohaemorrhagiae, Yersinia ruckerii and Stenotrophomonas maltophilia* (Türk, 2015). Antibiotics used for health and development in fish farms can kill beneficial microorganisms in the receiving environment. In addition, the application of antibiotics in fish farms leads to the proliferation of antibiotic-resistant microorganisms. It is generally known that 20-30% of antibiotics are in the body of fish, and the remaining 70-80% are transmitted to the environment. However, antibiotics that are recklessly discharged into the medium pose a major danger to habitats and all living things (Zhong *et al.,* 2018; Uma and Rebecca, 2018; Yang *et al.,* 2018; Li *et al.,* 2018; Tran *et al.,* 2016; Martinez *et al.,* 2015; Bengtsson-Palme and Larsson, 2015; Van Boeckel *et al.,* 2015). Anthropogenic activities result in the input of different antibiotics into aquatic environments, including effluent from hospitals and wastewater treatment facilities and discharge from agriculture, fish farming, and livestock husbandry (see Fig. 1) (Yang *et al.,* 2018; Guo *et al.,* 2017; Mishra *et al.,* 2017). Today, some factors such as the rapid increase of food demand in parallel with the increasing population, socio-economic progress and the efforts to reach healthy food led to the numerical development of fish and similar species having economic values (Meador *et al.,* 2016; Scott *et al.,* 2015).

Aquaculture is an effective food production area in terms of reducing the unconscious fishing in the natural fishery, creating business space and supporting the economy. Aquaculture has become an important food source with the increase of the global population (Miranda *et al.,* 2018). Fish farming industries play a crucial role in profit and employment in worldwide and procuration reliable foods to the population of the countries (Rahman *et al.,* 2017). The value of fish produced in fish farms has increased steadily in the last four decades (see Fig. 2) (Elevancini, 2017). For these reasons, aquaculture tends to increasingly grow all over the world and in Turkey. Compared to other countries, aquaculture activities in fish farms in Turkey are quite new (see Table 1) (Aydın and Baltacı, 2017; Özdal and Pulatsü, 2012).

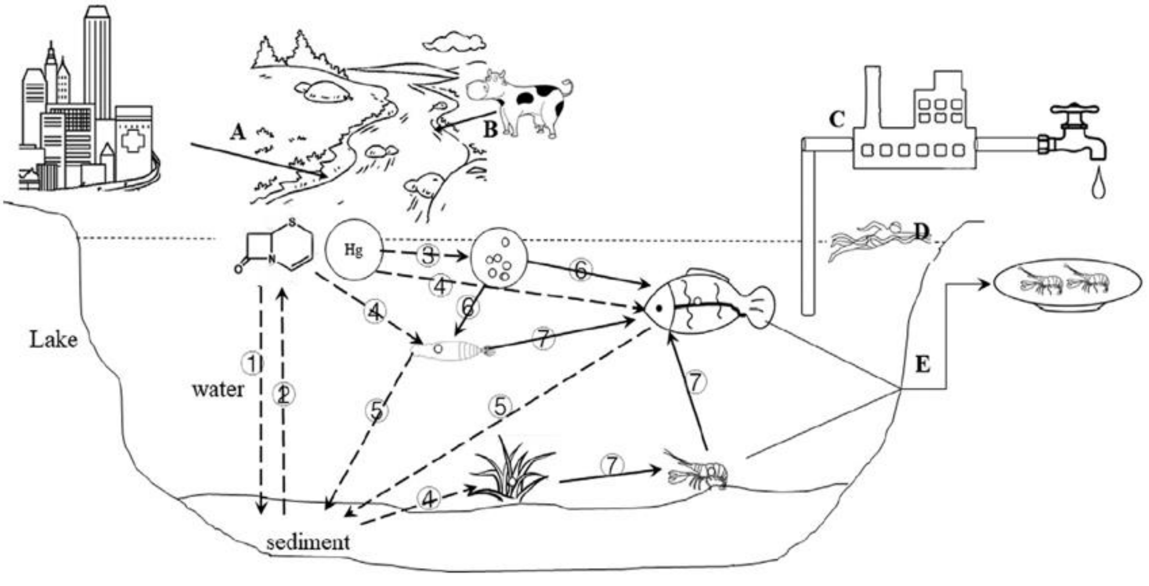

Fig. 1. Spread of antibiotics in different environments and possible exposure to all live health (Yang *et al.,* 2017a; Yang *et al.,* 2017b). *(A: antibiotics from wastewater treatment facilities-hospitals; B: antibiotics from agriculture, aquaculture and livestock husbandry; C: drinking water; D: recreation and swimming; E: swallow of aquatic products. ① the precipitation of antibiotics from water; ② the resuspension of antibiotics from residue; ③ change of microbial community by antibiotics; ④ chemical drugs cumulative by the aquatic medium; ⑤ antibiotics released from the death of aquatic lives; ⑥ Antibiotics absorbed/ adsorbed by water biota; ⑦ the transport of antibiotics and drugs among aquatic biota)*

Tablo 1. According to the year in Turkey, the amount of product produced in fish farms (Kayhan and Olmez, 2014).

Fish species	**2007**	**2008**	**2009**	**2010**	**2011**	**2012**	**2013**	**2014**	**2015**	**2016**
Total (tonnes)	138773	151990	158640	166801	188785	212410	233394	233713	238638	250281
Fish farms in the inland water district										
Trout (Rainbow)	58433	65928	75657	78165	100239	111335	122873	107533	100411	99712
Mirror-carp	600	629	591	403	207	222	146	157	206	196
Sturgeon	-	-	-	-	-	-	-	17	28	6
Tilapia	-	-	-	-	-	-	-	32	12	58
Fish farms in the sea area										
Trout (Rainbow)	2740	2721	5229	7079	7697	3234	5186	4812	6 187	4643
gilt-head bream	33500	31670	28362	28157	32187	30743	35701	41873	51844	58254
Perch	41900	49270	46554	50796	47013	65512	67913	74653	75164	80847
Fangri	-	-	-	-	-	-	-	106	143	225
Granyöz	-	-	-	-	-	-	-	3281	2801	2463
Sinagrit	-	-	-	-	-	-	-	113	132	43
tunny	-	-	-	-	-	-	-	1136	1710	3834
Other	1600	1772	2247	2201	1442	1364	1575	-	-	-

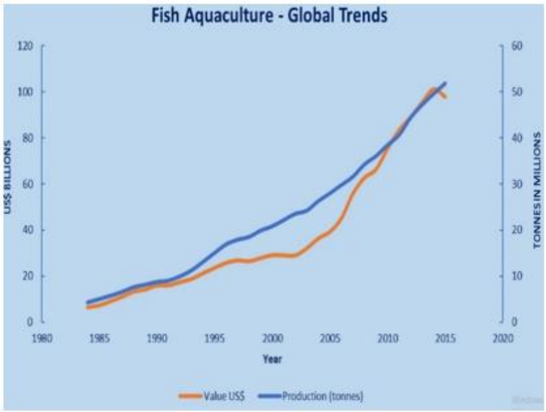

Fig. 2. Global production and value of cultured fish for the period 1984-2015 (Elevancini, 2017).

Due to the faeces and non-consumed feed, food elements in various forms (organic carbon, nitrogen, phosphorus) enter the receiving environments in the fish farms (Topçu *et al.,* 2017; Yavuzcan *et al.,* 2010). In addition, the antibiotic and drug residues used to protect fish and aquatic products from diseases also enter the receiving environments (Agoba *et al.,* 2017; Kim *et al.,* 2017; Caruso, 2016; Meador *et al.,* 2016; Scott *et al.,* 2015;). These chemicals accumulating in the base of the cage systems of these farms cause adverse changes in the life on the seabed, and therefore, they form sensitive areas in terms of environmental pollution. The production-environment interaction needs to be evaluated in order to determine whether the aquaculture in net cages used in the fish farms cause pollution of water resources. Fig. 3 shows the components that should be in a cage system used in these farms. The environmental problems occurring in fish farms during the aquaculture works are graphically expressed.

In this study, the environmental effects of production of various fish and other aquatic products carried out in cage systems in fish farms on especially water ecosystem, sediment, benthic flora and fauna, the harmful aspects of antibiotics and other drugs used to destroy pathogenic microorganisms and the problems that might occur in the food chain were investigated.

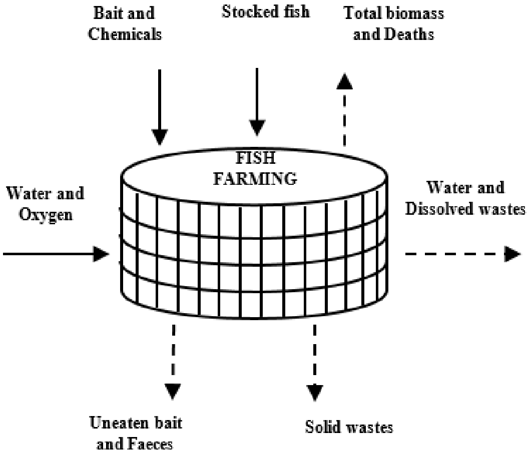

Fig. 3. Main inputs (straight lines) and output (cut lines) from cages in fish farms (URL-1, 2018).

2. MATERIAL AND METHOD

All academic areas related to fish farms and antibiotic usage were determined by electronic scanning of MEDLINE, PubMed, Google academic, ISIWeb of Science, Springer, Taylor-Francis, Elsevier and Scopus without time and language limitations. By using some keywords (fish farms, antibiotics, environmental problems, feed, cage fishing etc.), a national and international literature review was carried out.

3. ENVIRONMENTAL EFFECTS OF FISH FARMS

Although the rapid development of fish farms provides important socio-economic contributions to the countries, particularly their negative effects on water quality and ecological structure arise concern. Depending on the production methods and technologies in the farms, the amount of water products produced, and the quality of the receiving water environment, the size of this environmental change on the ecosystem varies.

3.1. Solid wastes and antibiotics

The negative effect of fish farming in cages on water resources emerges mainly due to the wastes originating from the aquaculture (Meador *et al.,* 2016; Abu Bakar *et al.,* 2016; Scott *et al.,* 2015). The types of waste originating from farms established in the receiving water environment have similar features all over the world, and the characteristics and levels of waste differ only according to the type of aquatic products and the farming technique (Yayan, 2015). Pollutants occurring as a result of the production of aquatic products in fish farms are considered as two different groups. The majority of solid wastes originating from fish farming is composed of substances such as fish faeces, scales, mucus secretion and non-consumed feed (see Fig. 4).

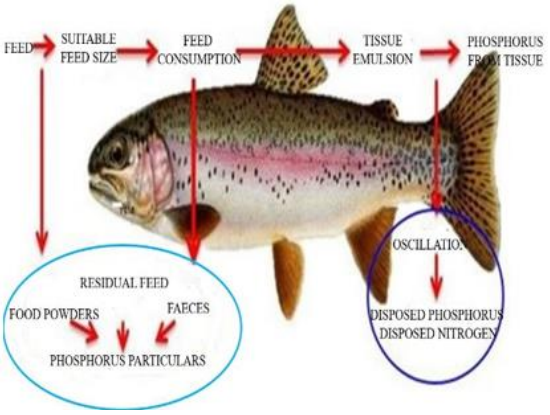

Fig. 4. Contaminants originating from a fish species produced in fish farms (Yayan, 2015; Rein *et al.*, 2015).

The highest rate of environmental pollutants in fish farms belongs to the pollutants resulting from feeding. At this point, it is observed that in the farms where proper feeding is not applied, there is a sediment accumulation and therefore an increase in the organic load of water (Yayan, 2015; Rein *et al.,* 2015; Yeo *et al.,* 2004; Bureau *et al.,* 2003). Solid wastes that are exposed in fish farms negatively affect the physicochemical structure and biological equilibrium of the different waters (Kim *et al.,* 2018; Opiyo *et al.,* 2018; Schumann *et al.,* 2017; Dolan *et al.,* 2013; Mirzoyan *et al.,* 2010). These solid wastes consist of various antibiotics, medicines, and uneaten fish food mixed with disinfectant, faeces, dead fish excretion and bio-flora. In particular, Tetracycline and amoxicillin are intensively applied with the aim of protecting the health of the fish (Chen *et al.,* 2017). Continuous exposure to these antibiotics in aquaculture may increase high antibiotic resistance (Zhao *et al.,* 2017; Harnisz *et al.,* 2015; Di Cesare *et al.,* 2013). Studies have reported that solid waste from fish farmings can act as potential pollutant-containing antibiotics (Kim *et al.,* 2018; Chen *et al.,* 2018; Xiong *et al.,* 2015; Luo *et al.,* 2010).

Antibiotics, drugs and hormones are extensively used in fish farms in order to treat the diseases caused by microorganisms such as *Clostridium, Vibrio, Pseudomonas, Escherichia, and Salmonella,* to enhance resistance, to improve product quality and for the other purposes (Cengizler *et al.,* 2017; Türk and Oğuz, 2013; Neary *et al.,* 2008;). In particular, various behavioural changes observed in fish (period movement, drowsiness, gathering together, etc.) and changes in the appearance of the eye (eye bleeding, colour problem, swelling, cysts, etc.) increase the use of these chemicals intensively. Especially, some antibiotics are used in the fish farms in all regions of the world (see Table 2) (Baba, 2017; Türk and Oğuz, 2013). In fish farms, *sodium, baylucite, iodophors, oxytetracycline, amoxicillin, erythromycin, sulphonamides* are widely used both in the world and in our country.

Table 2. Some chemicals used in fish farms (Kumar and Roy, 2017).

Antibiotics	Other Drugs	Disinfectants
Florfenicol	Akinitrazol	Phenols
Bacitracin	Methyl Parathion	Zephirol
Chloramphenicol	Salicylic acid	Sodium
Enrofloxacin	Copper sulphate	Baylusit
Canamycin	Trypaflavin	Formalin
Erythromycin	Rivanol	Chloramine T
Griseofulvin	Piavetrin	Slaked lime
Oleandomycin	Niclosamid	Quicklime
Neomycin	Metrifonate	Iodophors
Oxytetracycline	Lysol	Gonadotropin
Polymyxin	Gabrocol	Ormetoprim
Sulfamerazine	Diflubenzuron	Sulfasol
Sulfanilamide	Malathion	
Amoxicillin		

3.2. Effects on water quality criteria

In the cage where fish and other aqueous products are kept at fish farms, the effects of wastes originating from different production on aqueous environment have been being frequently observed in recent years. In particular, some studies have found that nitrogen, phosphorus, organic substance, chlorophyll-a, antibiotic residues, trace elements and suspended solids in the aqueous ecosystem increase the amount of solids, and reduce the entry of sunlight into the water, oxygen levels and acid-base balance. When the organic substance entering the aqueous environment by feed dissolves in water or transfers from sediment to water, it can lead to eutrophication and reduce the permeability of light especially in the environments where nutrients are limiter (see Fig. 5) (Coldebella et al., 2018; Abu Bakar *et al.,* 2016; Mancuso, 2015; Kayhan and Ölmez, 2014; Koca *et al.,* 2011; Holmer, 2010; Yıldırım and Korkut, 2004;).

4. CONCLUSIONS

While the world population is growing rapidly, humans’ need for food, especially the need for animal source food is also increasing. In line with this food demand, fish farms have become one of the rapidly growing food sectors on the global scale. Together with the development of the aquaculture field, the increase of pollution problems in the ecosystem has become inevitable. Because of the chemicals used in this sector such as antibiotics, hormones, and drugs, important environmental problems have been observed in terms of the quality of receiving water, sediment and benthic ecosystem. As in the entire in pollution situation, a strategy and plan for the pollution related to the fish farms also need to be developed. During the establishing and operating the fish farms, keeping certain precautions and rules in the foreground is of great importance to minimize the environmental pollution. In this context, the environmental aspects of aquaculture can be assessed in all aspects in the light of the following items.

1. In the selection of the area where the farms will be established, places with high flow rates should be preferred instead of places with low flow rates.
2. In the appropriate areas, at the end of each production season, the location of the cages should be changed; that is, the rotation should be applied.
3. In fish farms, feed management must be provided separately for each aquatic product and in this way, solid waste control must be ensured.
4. Because of some conditions (temperature-flow rate changes, insufficient gap rates in cages, water quality parameters) that can be observed in the areas established in fish farms, there may be uneasiness and restless behaviors in fish and similar aquatic products. In order to eliminate the existing stress, the regular control of the cage systems should be ensured.
5. Environmental monitoring of fish farms should be performed. In this way, detection of the problems arising from the farm and intervention to the problems are realized in a shorter time.
6. The natural landscape in the facility usage area should be given importance; especially endangered species of plants should not be harmed. Legislation, regulations, standards, and practices covering long years for such production in the country should be carried out and implemented in conjunction with both the production authorities and the population living in the region. In addition, activities that can eliminate environmental problems arising from fish farms should be concentrated on.

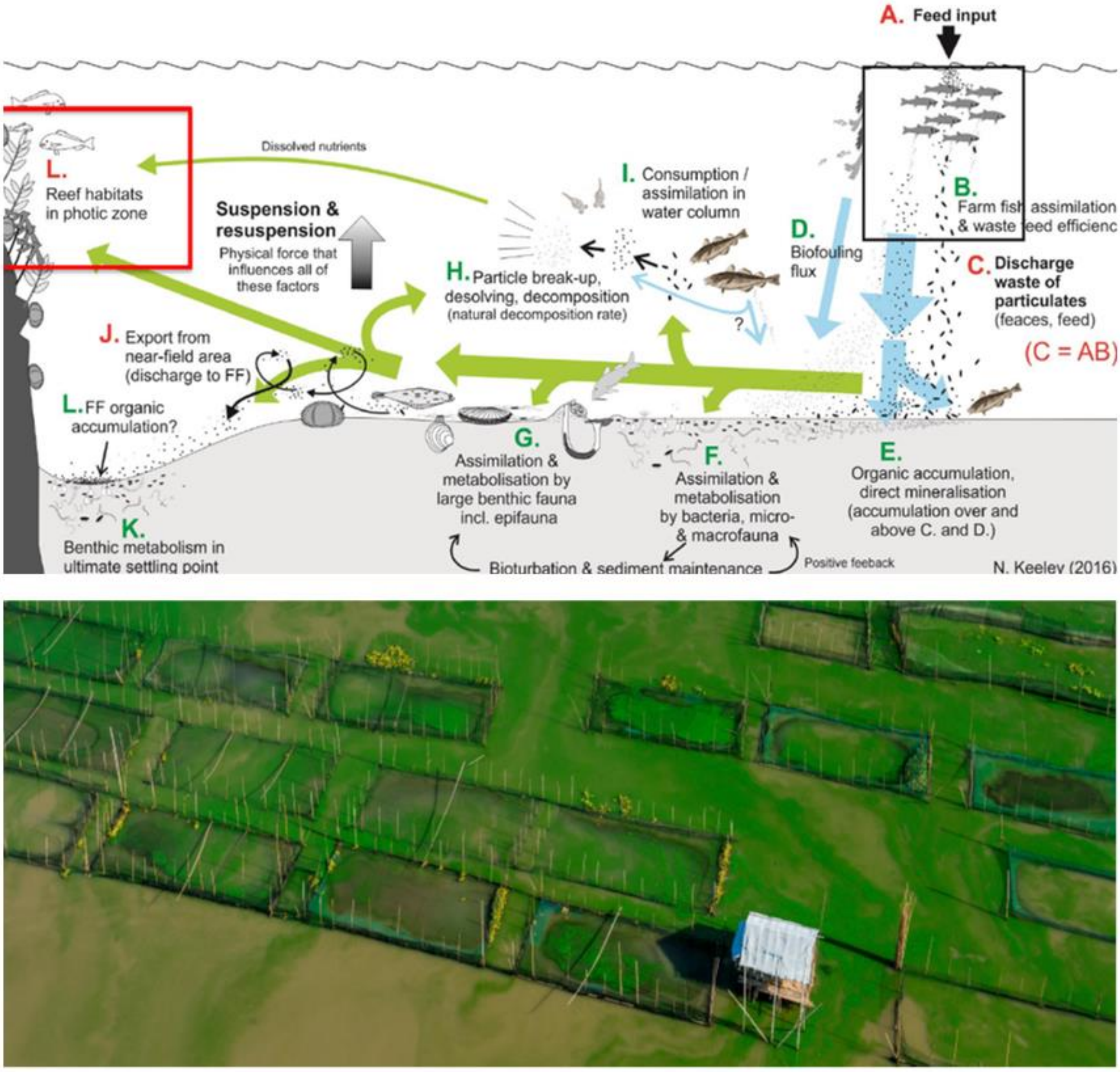

Fig. 5. Discharges and changes in the water environment of organic charges (Coldebella et al., 2018; Jakobsen *et al.*, 2017; Abu Bakar *et al.*, 2016; Buschmann *et al.*, 2009).

REFERENCES

Abu Bakar, N. H., Jusoh, A., Ahmad, M. F., Noor, M. J. M. M., Norzilah, A. (2016). " A Spatial nutrient distribution due to seabass aquaculture activities at Setiu, Terengganu, Malaysia." *Journal of Fisheries and Aquatic Science,* Vol. 11, pp. 332-348.

Agoba, E. E., Adu, F., Agyare, C., Boamah, V. E. (2017). "Antibiotic use and practices in selected fish farms in the Ashanti Region of Ghana." *Journal of Infectious Diseases and Treatment,* Vol. 3, pp. 1-6.

Aydın, H., Baltacı, M.A. (2017). "Türkiye'de alabalık üretiminin yaygınlaşmasında istanbul üniversitesi sapanca içsu ürünleri üretimi araştırma ve uygulama birimi'nin yeri." *Turkish Journal of Aquatic Sciences,* Vol. 32, No. 3, pp. 129-134.

Baba, E. (2017). "Su ürünleri yetiştiriciliğinde bitkisel immunostimulant kullanımı." *Iğdır Üniversitesi Fen Bilimleri Enstitüsü Dergisi,* Vol. 7, No. 3, pp. 249-256.

Bengtsson-Palme, J., Larsson, D. G. J. (2015). "Antibiotic resistance genes in the environment: prioritizing risks." *Nature Reviews Microbiology,* Vol. 13, p. 396.

Buschmann, A. H., Cabello, F., Young, K., Carvajal, J., Varela, D. A., Henriquez, L. (2009). "Salmon aquaculture and coastal ecosystem health in Chile: Analysis of regulations, environmental impacts and bioremediation systems." *Ocean and Coastal Management,* Vol. 52, pp. 243-249.

Bureau, D. P., Gunther, S. J., Cho, C. Y. (2003). "Chemical composition and preliminary theoretical estimates of waste outputs of rainbow trout reared in commercial cage culture operations in Ontario." *North American Journal of Aquaculture,* Vol. 65, pp. 33-38.

Caruso, G. (2016). "Antibiotic resistance in fish farming environments: a global concern." *Journal of Fisheries Sciences,* Vol. 10, No. 4, pp. 9-13.

Cengizler, İ., Aytaç, N., Aldık, R. (2017). "Biocide use and its potential risks in aquaculture in Turkey." *Eastern Anatolian Journal of Science,* Vol. 3, No. 1, pp. 1-5.

Chen, C.Q., Zheng, L., Zhou, J.L., Zhao, H. (2017). "Persistence and risk of antibiotic residues and antibiotic resistance genes in major mariculture sites in Southeast China." *Science of the Total Environment,* Vol. 580, pp. 1175-1184.

Chen, H., Liu, S., Xu, X. R., Diao, Z. H., Sun, K. F., Hao, Q. W., Liu, S. S., Ying, G. G. (2018). "Tissue distribution, bioaccumulation characteristics and health risk ofantibiotics in cultured fish from a typical aquaculture area." *Journal of Hazardous Materials,* Vol. 343, pp. 140-148.

Coldebella, A., Gentelini, A. L., Piana, P. A., Codebella, P. F., Boscolo, W. R., Feiden, A. (2018). "Effluents from fish farming ponds: a view from the perspective of its main components." *Sustainability,* Vol. 10, pp. 1-16.

Di Cesare, A., Luna, G.M., Vignaroli, C., Pasquaroli, S., Tota, S., Paroncini, P., Biavasco, F. (2013). "Aquaculture can promote the presence and spread of antibiotic-resistant Enterococci in marine sediments." *PLoS One,* Vol. 8, pp. e62838.

Dolan, E., Murphy, N., O'Hehir, M. (2013). "Factors influencing optimal micro-screen drum filter selection for recirculating aquaculture systems." *Aquacultural Engineering,* Vol. 56, pp. 42-50.

Elevancini, J. S. (2017). How do third-party certifications control the use of antibiotics in global salmon aquaculture?, PhD Thesis, Dalhousie University, Halifax, Nova Scotia.

Guo, J. H., Li, J., Chen, H., Bond, P. L., Yuan, Z. G. (2017). "Metagenomic analysis reveals wastewater treatment plants as hotspots of antibiotic resistance genes and mobile genetic elements." *Water Research,* Vol. 123, pp. 468-478.

Harnisz, M., Korzeniewska, E., Gołaś, I. (2015). "The impact of a freshwater fish farm on the community of tetracycline-resistant bacteria and the structure of tetracycline resistance genes in river water." *Chemosphere,* Vol. 128, pp. 134-141.

Holmer, M. (2010). "Environmental issues of fish farming in offshore waters: perspectives, concerns and research needs." *Aquaculture Environment Interactions,* Vol. 1, pp. 57-70.

Jakobsen, H. R., Skarra, H., Arvesen, M. P. (2017). *Nordic Conference 2017-Aquaculture,* Technical Report, Norway.

Karaman, S. (2006). "Hayvansal üretimden kaynaklanan çevre sorunları ve çözüm olanakları." *KSÜ Fen ve Mühendislik Dergisi*, Vol. 9, No. 2, pp. 133-139.

Kayhan, M. H., Olmez, M. (2014). "Aquaculture and organic aquaculture in Turkey." *Journal of Aquaculture Research & Development,* Vol. 5, No. 5, pp. 1-5.

Kim, H. Y., Lee, I. S., Oh, J. E. (2017). "Human and veterinary pharmaceuticals in the marine environment including fish farms in Korea." *Science of the Total Environment,* Vol. 579, pp. 940-949.

Kim, Y. B., Jeon, J. H., Choi, S., Shin, J., Lee, Y., Kim, Y. M. (2018). "Use of a filtering process to remove solid waste and antibiotic resistance genes from effluent of a flow-through fish farm." *Science of the Total Environment,* Vol. 615, pp. 289-296.

Koca, S. B., Terzioğlu, S., Didinen, B. I., Yiğit, N. Ö. (2011). "Sürdürülebilir su ürünleri yetiştiriciliğinde çevre dostu üretim." *Ankara Üniversitesi Çevrebilimleri Dergisi*, Vol. 3, No. 1, pp. 107-113.

Kumar, V., Roy, S. (2017). "Aquaculture drugs: sources, active ingredients, pharmaceutic preparations and methods of administration." *Journal of Aquaculture Research and Development,* Vol. 8, No. 9, pp. 1-13.

Li, S., Shi, W., Liu, W., Li, H., Zhang, W., Hu, J., Ke, Y., Sun, W., Ni, J. (2018). "A duodecennial national synthesis of antibiotics in China's major rivers and seas (2005-2016)." *Science of the Total Environment,* Vol. 615, pp. 906-917.

Luo, Y., Mao, D., Rysz, M., Zhou, Q., Zhang, H., Xu, L., Alvarez P. J. J. (2010). "Trends in antibiotic resistance genes occurrence in the Haihe River, China." Environmental Science and Technology, Vol. 44, pp. 7220-7225.

Mancuso, M. (2015). "Effects of fish farming on marine environment." *Journal of Fisheries Sciences,* Vol. 9, No. 3, pp. 89-90.

Martinez, J. L., Coque, T. M., Baquero, F. (2015). "What is a resistance gene? Ranking risk in resistomes." *Nature Reviews Microbiology,* Vol. 13, pp. 116-123.

Meador, J. P., Yeh, A., Young, G., Gallagher, E. P. (2016). "Contaminants of emerging concern in a large temperate estuary." *Environmental Pollution,* Vol. 213, pp. 254-267.

Miranda, C. D., Godoy, F. A., Lee, M. R. (2018). "Current status of the use of antibiotics and the antimicrobial resistance in the chilean salmon farms." *Frontiers in Microbiology,* Vol. 9, 1-14.

Mirzoyan, N., Tal, Y., Gross, A. (2010). "Anaerobic digestion of sludge from intensive recirculating aquaculture systems: review." *Aquaculture,* Vol. 306, pp. 1-6.

Mishra, S. S., Das, R., Choudhary, P., Debbarma, J., Sahoo, S. N., Swain, P., Rathore, R., Giri, B. S. (2017). "Prevalence of fish and shrimp diseases and use of various drugs and chemicals in ındian aquaculture for disease management." *Journal of Fisheries and Aquaculture Development,* Vol. 2017, No. 6, pp. 1-16.

Neary, E. T., Develi, N., Yüksel, S. A. (2008). "Su ürünleri yetistiriciliginde kullanılan aşılar." *GOÜ Ziraat Fakültesi Dergisi,* Vol. 25, No. 2, pp. 29-35.

Opiyo, M. A., Marijani, E., Muendo, P., Odede, R., Leschen, W., Charo-Karisa, H. (2018). "A review of aquaculture production and health management practices of farmed fish in Kenya." *International Journal of Veterinary Science and Medicine,* (article in press).

Orçun, E., Sunlu, U. (2007). "Sığacık (Seferihisar-İzmir) Bölgesi Ağ Kafeslerde Yapılan Balık Yetiştiriciliğinin Sucul Ortama Olan Etkilerinin Araştırılması." *E.Ü. Su Ürünleri Dergisi*, Vol. 24, No. 1-2, pp. 1-9.

Özdal, B., Pulatsü, S. (2012). **"**Ağ kafeslerde sürdürülebilir balık yetiştiriciliği için bir bilgisayar yazılımının kullanımı." *Ankara Universitesi Cevrebilimleri Dergisi***,** Vol. 4, No. 1, pp. 15-26.

Rahman, Md. Z., Khatun, A., Kholil, Md. I., Hossain, Md. M. M. (2017). "Aqua drugs and chemicals used in fish farms of Comilla regions." *Journal of Entomology and Zoology Studies,* Vol. 5, No. 6, pp. 2462-2473.

Rein, A., Wu, Y., Yemelyanova, M. (2015). *Phosphorus Project: Sea Breeze, IV.* Project Report, Denmark.

Schumann, M., Unger, J., Brinker, A. (2017). "Floating faeces: effects on solid removal and particle size distribution in RAS." *Aquacultural Engineering,* Vol. 78, pp. 75-84.

Scott, W. C. C., Du, B., Haddad, S. P., Breed, C. S., Saari, G. N., Kelly, M., Broach, L., Chambliss, C. K., Brooks, B. W. (2015). "Predicted and observed therapeutic dose exceedences of ionizable pharmaceuticals in fish plasma from urban coastal systems." *Environmental Toxicology and Chemistry,* Vol. 35, No. 4, pp. 983-995.

Topçu, A., Pulatsü, S., Kaya, D. (2017). "Almus baraj gölü (Tokat)'nde kafeslerde gökkuşağı alabalığı yetiştiriciliğinin sedimentten fosfor salınımına etkisi." *Iğdır Üniversitesi Fen Bilimleri Enstitüsü Dergisi,* Vol. 7, No. 2, pp. 295-302.

Türk, E. (2015). Muğla bölgesindeki balık çiftlikleri çevresinden avlanan balıklarda tetrsiklin aranması, Doktora Tezi, Selçuk Üniversitesi, Konya, Türkiye.

Tran, N. H., Chen, H. J., Reinhard, M., Mao, F., Gin, K. Y. H. (2016). "Occurrence and removal of multiple classes of antibiotics and antimicrobial agents in biological wastewater treatment processes." *Water Research,* Vol. 104, pp. 461-472.

Türk, E., Oğuz, H. (2013). "Kültür balıkçılığında ilaç kullanımı ve halk sağlığı açısından önemi." *Bornova Veteriner Bilimleri Dergisi,* Vol. 35, No. 49, pp. 35-43.

Uma, A., Rebecca, G. (2018). "Antibiotic resistance in bacterial isolates from commercial probiotics used in aquaculture." *International Journal of Current Microbiology and Applied Sciences,* Vol. 7, No. 1, pp. 1737-1743.

URL-1, Ağ Kafeslerde Balık Yetiştiriciliğinin Su Kalitesine Etkisi, https://acikders.ankara.edu.tr [Accessed 26 July 2018].

Van Boeckel, T. P., Brower, C., Gilbert, M., Grenfell, B. T., Levin, S. A., Robinson, T. P., Teillant, A., Laxminarayan, R. (2015). "Global trends in antimicrobial use in food animals." *Proceedings of the National Academy of Sciences of the United States of America*, Vol. 112, No. 8, pp. 5649-5654.

Xiong,W., Sun, Y., Zhang, T., Ding, X., Li, Y.,Wang, M., Zeng, Z. (2015). "Antibiotics, antibiotic resistance genes, and bacterial community composition in fresh water aquaculture environment in China." *Microbial Ecology,* Vol. 70, pp. 425-432.

Yang, Y., Liu, W., Xu, C., Wei, B., Wang, J. (2017a). "Antibiotic resistance genes in lakes from middle and lower reaches of the Yangtze River, China: effect of land use and sediment characteristics." *Chemosphere,* Vol. 178, pp. 19-25.

Yang, Y., Song, W., Lin, H., Wang, W., Du, L., Xing, W. (2018). "Antibiotics and antibiotic resistance genes in global lakes: A review and meta-analysis." *Environment International,* Vol. 116, pp. 60-73.

Yang, Y., Xu, C., Cao, X., Lin, H., Wang, J. (2017b). "Antibiotic resistance genes in surface water of eutrophic urban lakes are related to heavy metals, antibiotics, lake morphology and anthropic impact." *Ecotoxicology,* Vol. 26, pp. 831-840.

Yavuzcan, H., Pulatsü, S., Demir, N., Kırkağaç, M., Bekcan, S., Topçu, A., Doğankaya, L., Basçınar, N. (2010). "Türkiye'de Sürdürülebilir Su Ürünleri Yetistiriciliği." *TMMOB Ziraat Mühendisliği VII. Teknik Kongresi*, Ankara, Türkiye, pp.767-789.

Yayan, D. T. (2015). Durgun sularda balık yetiştiriciliğinin besin elementleri açısından etkilerinin azaltılması, Uzmanlık Tezi, Türkiye Cumhuriyeti Orman ve Su İşleri Bakanlığı, Ankara, Türkiye.

Yeo, S. F., Binkowski, F. P., Morris, J. E. (2004). "Aquaculture effluents and waste by-products characteristics, potential recovery, and beneficial reuse." *NCRAC Technical Bulletins,* Vol. 6, pp. 1-41.

Yıldırım, Ö., Korkut, A. Y. (2004). "Su ürünleri yemlerinin çevreye etkisi." *Ege Üniversitesi Su Ürünleri Dergisi,* Vol. 21, No 1-2, pp. 167-172.

Zhao, Z., Wang, J., Han, Y., Chen, J., Liu, G., Lu, H., Yan, B., Chen, S. (2017). "Nutrients, heavy metals and microbial communities co-driven distribution of antibiotic resistance genes in adjacent environment of mariculture." *Environmental Pollution,* Vol. 220, pp. 909-918.

Zhong, Y., Chen, Z. F., Dai, X., Liu, S. S., Zheng, G., Zhu, X., Liu, S., Yin, Y., Liu, G., Cai, Z. (2018). "Investigation of the interaction between the fate of antibiotics in aquafarms and their level in the environment." *Journal of Environmental Management,* Vol. 207, pp. 219-229.

Turkish Journal of Engineering

Turkish Journal of Engineering (TUJE)
Vol. 3, Issue 2, pp. 68-75, April 2019
ISSN 2587-1366, Turkey
DOI: 10.31127/tuje.453593
Research Article

INVESTIGATION OF OXYGEN-RELATED DEFECTS IN ZnO: GROWING TIME AND Mn CONCENTRATION EFFECTS

Saadet Yıldırımcan [1] and Selma Erat [*2,3]

[1] Toros University, Faculty of Engineering, Department of Electrical-Electronics, Mersin, Turkey
ORCID ID 0000 – 0002 – 9044 – 6908
saadetyildirimcan@gmail.com

[2] Mersin University, Vocational School of Technical Sciences, Department of Medical Services and Techniques, Program of Opticianry, Mersin, Turkey
[3]Advanced Technology, Research and Application Center, Mersin University, Mersin, Turkey
ORCID ID 0000 – 0001 – 7187 – 7668
selmaerat33@gmail.com

---

* Corresponding Author
Received: 14/08/2018 Accepted: 12/09/2018

ABSTRACT
The optical and photoluminescence properties of ZnO nanocrystals synthesized via hydrothermal method are determined in this study. The effect of growing time (1 h, 6 h, 12 h, 24 h and 36 h) and Mn concentration ($5x10^{-4}$ mol, $10x10^{-4}$, $25x10^{-4}$ mol, $75x10^{-4}$ mol, $100x10^{-4}$ mol, $250x10^{-4}$ mol) on these properties are investigated and presented in detail. The ultraviolet–visible (UV-Vis) and photoluminescence (PL) spectroscopy techniques are used for optical and photoluminescence properties characterization. Room temperature PL spectra of the ZnO nanopowders show a near band-edge emission (peak at 385 nm) and a red light emission (peak at 650 nm) for both ZnO synthesized for different growing time and different Mn concentration. The ZnO prepared with 1 h and 12 h includes the lowest oxygen related defects. The ZnO doped with $5x10^{-4}$ mol shows the highest oxygen related defects whereas that of $100x10^{-4}$ mol shows the lowest defects.

Keywords: *ZnO, Mn, Photoluminescence Properties, Optical Properties, Nanoparticles*

1. INTRODUCTION

Zinc oxide (ZnO) being which is an intrinsic n-type II-VI semiconductor and have a wide-band gap (3.37 eV) and a large exciton binding energy (60 meV, at room temperature) has received considerable attention since it is low cost, non-toxic, chemically stable, high thermally stable environmentally friendly and further its optical and electrical properties can be tuned by doping (Putri *et al.*, 2018; Karmakar *et al.*, 2012; Kadam *et al.*, 2017; Dhara *et al.*, 2018; Fan *et al.*, 2004; Wang *et al.*, 2011; Choudhury *et al.*, 2016). Therefore, ZnO has several applications such as gas sensors (Wang *et al.*, 2017; Wang *et al.*, 2015; Othman *et al.*, 2017), solar cells (Dhara *et al.*, 2018; Sekine *et al.*, 2009; Keis *et al.*, 2002; Law *et al.*, 2005; Martinson *et al.*, 2007), and light emitting diodes (Saito *et al.*, 2002), optical modulator waveguides (Koch *et al.*, 1995), field effect transistor (Vijayalakshmi *et al.*, 2015), UV detectors (Das *et al.*, 2010), and surface acoustic wave filters (Emanetoglu *et al.*, 1999). ZnO has been synthesized using different techniques such as microwave-assisted synthesis (Schneider *et al.*, 2010), sol–gel processing (Bahnemann *et al.*, 1987), hydrothermal synthesis (Li *et al.*, 2001), aerosol spray analysis (Motaung *et al.*, 2014), wet chemical (Toloman *et al.*, 2013) and hydrolysis/condensation (Cohn *et al.*, 2012).

It was reported that doping ZnO with transition metal ions such as Mn, Fe, Co, Ni, and Cu reduced the band gap energy and prevent electron-hole pair recombination through the generation of new states (Achouri *et al.*, 2016; Anandan *et al.*, 2007; Chauhan *et al.*, 2012; Saleh *et al.*, 2014; Bhatia *et al.*, 2017; Nasser *et al.*, 2017; Tabib *et al.*, 2017; Altintas Yildirim *et al.*, 2016). Besides, it is known that tuning the morphology of ZnO nanostructure turns out variations in optical and electrical properties (Awad *et al.*, 2015). Among all of the aforementioned transition elements, the most encouraging one is Mn for doping ZnO nanostructure because Mn with valence state of 2+ has the highest possible magnetic moment (Khanna *et al.*, 2003). Further, substituting Mn ions into ZnO may enhance the photocatalytic activity under UV and visible irradiation and that is attributed to an increase in the number of defect sites acting as electron traps that effectively suppresses the recombination of the photogenerated carriers (Achouri *et al.*, 2016; Saleh *et al.*, 2014; Ma *et al.*, 2016; Barzgari *et al.*, 2016; Umar *et al.*, 2015; Donkova *et al.*, 2010; Ullah *et al.*, 2008).

There are some other studies about Mn doped ZnO for instance Deka *et al.* (Deka *et al.*, 2007) reported that doping Mn ions in ZnO results in an increase in both of unit cell volume and the optical band gap. In addition, Li *et al.* (Moontragoon *et al.*, 2013) demonstrated that Mn doped ZnO nanorods had a strong near band-edge emission and a weak deep level emission. It was an aim of our group to investigate the changes of local environment of doped ion Mn^{2+} in ZnO (Yildirimcan *et al.*, 2016). The defects in pure ZnO and Mn doped Mn were determined via electron paramagnetic resonance (EPR) and it was concluded that structural defects due to Zn and O vacancies were dominant compared to extrinsic (Mn^{2+} ion) structural defects (Yildirimcan *et al.*, 2016). Since the synthesis process and characterization of the electronic and thermal properties of our ZnO and Mn doped ZnO nanocrystals were studied via x-ray diffraction (XRD), thermogravimetry (TG), differential thermal analysis (DTA), field emission-scanning electron microscopy (FE-SEM), transmission electron microscopy (TEM), energy dispersive x-ray (EDX), inductively coupled plasma mass spectrometry (ICP-MS) techniques by our group (Yildirimcan *et al.*, 2016), here in this study we focus on the optical properties of those samples of ZnO and Mn doped ZnO nanocrystals synthesized by using hydrothermal route. The ultraviolet–visible (UV-Vis) and photoluminescence (PL) spectroscopy techniques are used in order to investigate the optical properties of the samples.

2. EXPERIMENTAL PROCESS

The ZnO and Mn-doped ZnO nanopowder was synthesized with the hydrothermal technique in Teflon-lined autoclave at 70 °C. The synthesis of these samples is the same as our previously published study (Yildirimcan *et al.*, 2016). The precursor solutions were prepared using the stoichiometric amount of zinc nitrate hexahydrate ($Zn(NO_3)_2$ $6H_2O$, Acros Organics), polyethylene glycol (PEG300, Aldrich Chemistry) and ammonia (NH_3, Analar Normapur) to produce ZnO nanopowders. ZnO nanopowders were synthesized for various duration times such as 1 h, 6 h, 12 h, 24 h and 36 h. The $Mn(NO_3)_2$ $4H_2O$ solution was prepared certain Mn^{2+} concentration (X1: undoped, X2: 5 $x10^{-4}$ mol; X3: 10 x 10^{-4} mol; X4: 25 x 10^{-4} mol; X5: 75 x 10^{-4} mol; X6: 100 x 10^{-4} mol; X7: 250 x 10^{-4} mol). These solutions were added into the solutions, which are used to prepare ZnO nanopowders (6 h) and the synthesis of Mn doped ZnO nanopowders was performed. Finally, the precipitation of ZnO and ZnO:Mn was filtered, washed with distilled water, and were dried in an oven at 80 °C for 1 h (Yildirimcan *et al.*, 2016). All of the details about the chemical reaction mechanisms followed for the formation of ZnO and Mn doped ZnO were given (Yildirimcan *et al.*, 2016).

Photoluminescence (PL) measurements of the nanocrystals were made by using a Varian Cary Eclipse Fluorescence spectrophotometer. The UV-visible spectra of the nanocrystals were recorded by using UV-1800 Shimadzu UV-Vis spectrophotometer in the range 200-900 nm.

3. RESULTS AND DISCUSSIONS

Recently, the crystallographic structure of the ZnO and Mn doped ZnO was presented by our group (Yildirimcan *et al.*, 2016) and is summarized in this study for the reader to get a view of all properties. The crystallographic structures of the nanocrystals were defined in following:

The samples synthesized for 1 h, 6 h, 12 h, 24 h, and 36 h were grown in hexagonal wurtzite structure, which was well coincided with JCPDS no: 36-1451. The (101) direction was preferred by the samples synthesized for 1 h-24 h whereas (002) was preferred by the sample 36 h. It was calculated that the crystallite sizes of the samples are increased from 30 nm to 51 nm upon growing time increase from 1 h to 36 h. On the other hand, Mn doped ZnO samples (X2-X7) were formed in hexagonal structure, which was well coincided with JCPDS no: 03-0888. There were no observed systematic increases of crystallite size by increasing the Mn concentration in ZnO. Fig. 1 shows the change in the lattice parameter of for the samples synthesized for 1 h − 36 h and synthesized with different Mn concentration (Yildirimcan *et al.*, 2016).

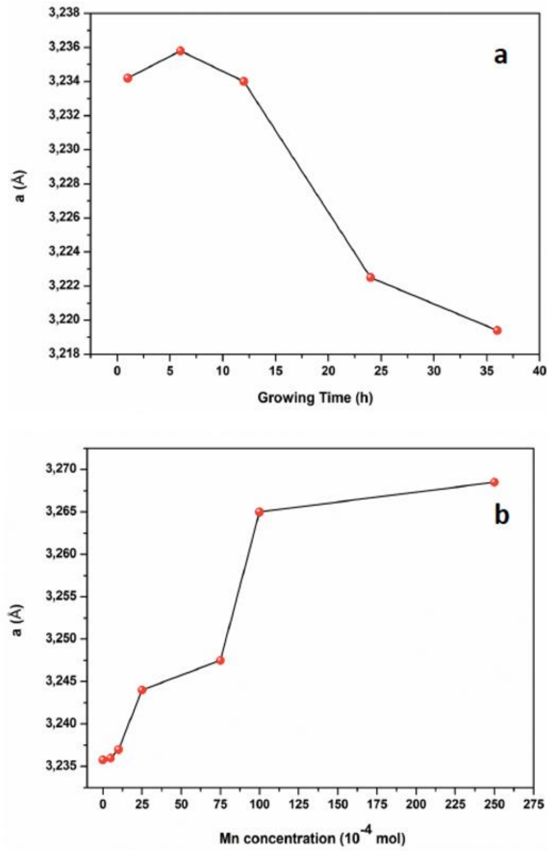

Fig. 1. Change in the lattice parameter of a in hexagonal structure of ZnO (a) depending growing time (b) depending on Mn concentration (Yildirimcan *et al.*, 2016)

The highest value of *a* is observed for the sample prepared for 6 h in the series presented in Fig. 1 (a). Besides, the value of *a* is increased upon Mn concentration increase as it is shown in Fig. 1 (b).

Photoluminescence and optical properties, which are the main scope of this study, are investigated and presented in detail. The results were presented in two different sections in following. The comparisons of the results with literature are presented in the discussions part.

3.1. Photoluminescence Analysis of ZnO Nanoparticles: Growing Time and Mn Concentration Effects

Photoluminescence (PL) spectra are recorded by using a Varian Cary Eclipse Fluorescence spectrophotometer. The PL measurements of ZnO synthesized with different growing time and Mn doped ZnO nanoparticles were performed under the excitation wavelength of λ_{ex}: 325 nm. Fig. 2 shows the PL spectra of ZnO nanocrystals synthesized for different growing time.

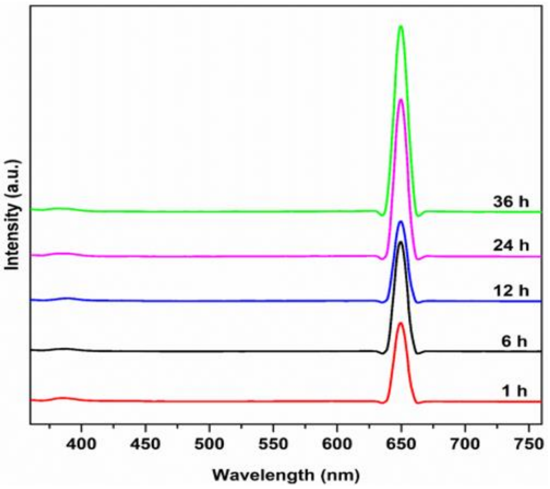

Fig. 2. PL spectra of ZnO synthesized for different growing time.

As it is easy to observe in Fig. 2, there is a significant change in the peak exists at around 650 nm. However, it is difficult to observe the change in peak at around 390 nm. Therefore, Fig. 3 shows the change in PL spectra of ZnO depending on growing time (a) UV emission peak in the wavelength 370-410 nm and (b) red emission peak in the wavelength 640-660 nm.

The wavelengths of UV emission of ZnO nanopowders prepared for 1 h, 6 h, 12 h, 24 h and 36 h are 386 nm (3.22 eV), 387 nm (3.21 eV), 389 nm (3.19 eV), 384 nm (3.23 eV) and 383.5 nm (3.24 eV), respectively.

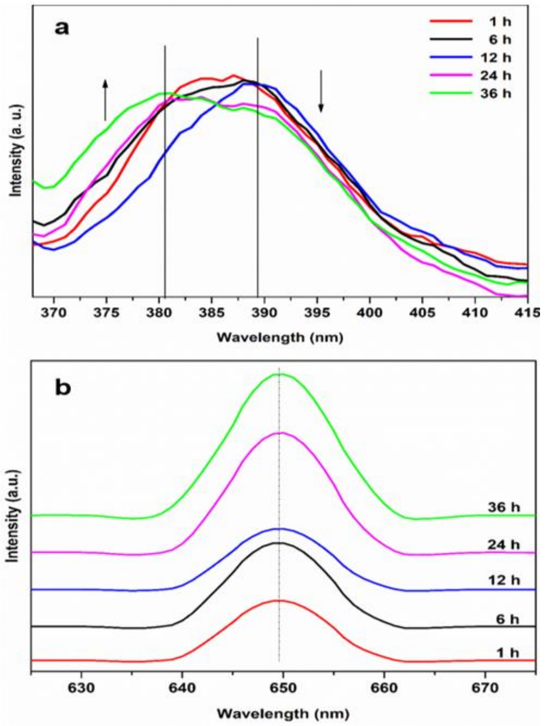

Fig. 3. Enlarged (a) UV peak and (b) visible light emission of ZnO nanoparticles depending on growing time.

The UV peak is characteristic emission peak of ZnO, which is a near band-edge emission. Also, ZnO has very good UV emission characteristics. (Wei *et al.*, 2010). There was no significant change in the UV peak intensity of ZnO nanopowders depending on the growing time. The samples prepared for 6 h and 12 h shift to a longer wavelength, while those prepared for 24 h and 36 h shift to a shorter wavelength.

The red emission peaks of ZnO prepared for different growing times are shown in Fig. 3 (b). The peaks exist at around the wavelength of 650 nm. The change in the PL spectra of ZnO depending Mn concentration is shown in Fig. 4.

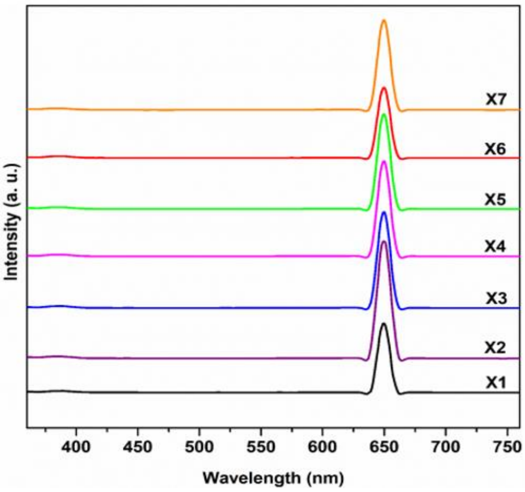

Fig. 4. PL spectra of ZnO:Mn nanoparticles.

Since it is difficult to follow the change both in UV peak and red emission peak in this figure, the peaks are redrawn separately in Fig. 5 (a) and (b), respectively.

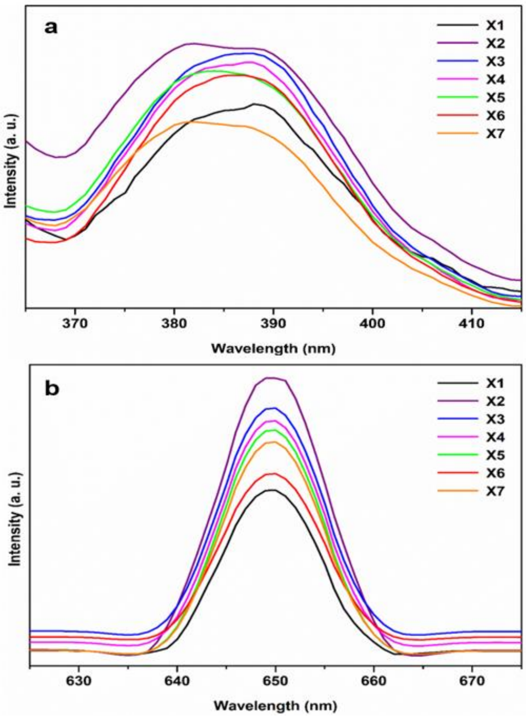

Fig. 5. Enlarged (a) UV peak and (b) visible light emission of ZnO nanoparticles depending on Mn concentration.

The UV emission wavelength of Mn doped ZnO nanopowders is 386 nm, 384.23 nm, 386.15 nm, 385.6 nm, 384.7 nm, 386 nm and 382.65 nm for X1 (undoped), X2, X3, X4, X5, X6, and X7, respectively. It is difficult to observe a systematic change neither in peak position nor in intensity of the UV peak upon Mn concentration increase. It was not observed a regular change in the UV peak wavelength and intensity of Mn doped ZnO nanoparticles depending on the Mn^{2+} concentration. In Fig. 5 (b), the red emission peaks are observed at the wavelength of 650 nm for Mn doped ZnO samples in agreement with the literature (Kaftelen *et al.*, 2012).

3.2. Optical Properties of ZnO Nanoparticles: Growing Time and Mn Concentration Effects

The UV–visible spectra of the nanoparticles were recorded using UV–1800 Shimadzu UV-Vis spectrophotometer in the range 200 – 900 nm at room temperature (RT). Figure 6 shows the RT absorbance spectra of ZnO nanocrystals prepared for different growing time (1 h, 6 h, 12 h, 24 h, and 36 h).

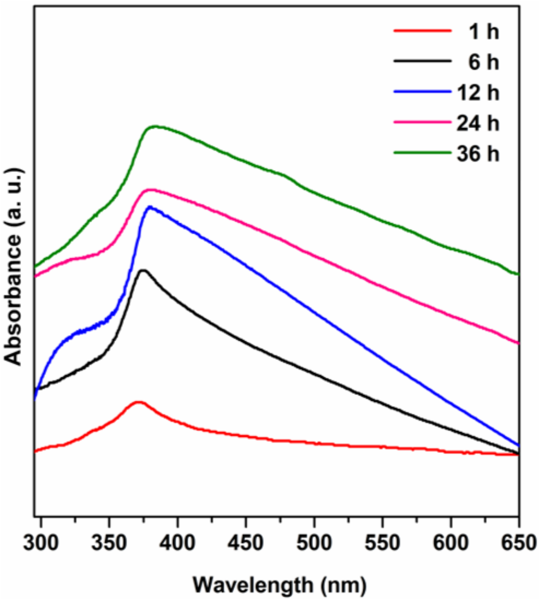

Fig. 6. UV-VIS absorbance spectra of ZnO nanoparticles depending on growing time

The absorbance peaks known as excitonic absorption peaks of the samples appeared in the wavelength range of 350 nm – 420 nm. Namely, the excitonic peak exists at 371 nm, 374 nm, 379 nm, 380 nm, and 382 nm for the sample synthesized for 1 h, 6 h, 12 h, 24 h, and 36 h, respectively. It was mentioned in the literature (Samanta *et al.*, 2018) that the absorbance spectra of nanostructures were affected by various factors such as particle size, defect of structure, oxygen vacancy. A small shift toward higher wavelength known as red shift is observed with increasing growing time. The reason for red shift might be increasing concentration of oxygen vacancies on surface ZnO nanopowders (Ahmed, 2017).

Figure 7 shows the change in the excitonic absorption peak position in energy scale (eV) depending on the growing time.

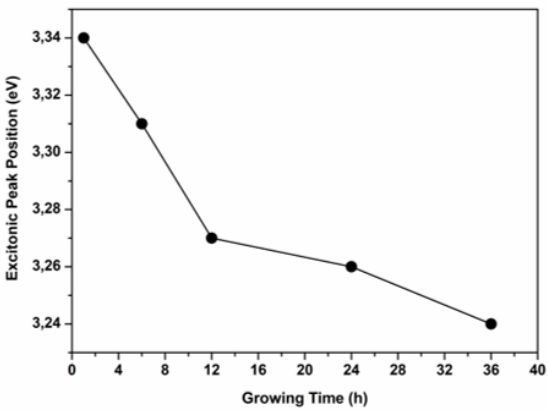

Fig. 7. The change in the excitonic absorption peak position of ZnO depending on growing time

It is observed in Fig. 7 that there is a decrease at the peak position with increasing growing time.

Fig. 8 shows the RT UV–visible absorbance spectra of ZnO nanocrystals doped with different Mn^{2+} concentrations in the wavelength range of 200 nm – 700 nm. It is noticed that the spectra of ZnO is changed drastically once it is doped with Mn^{2+} ions. However, increasing Mn^{2+} ion concentration does not make any change in the spectra significantly. The absorbance peak occurred at 374 nm for undoped ZnO (X1) and 372 nm, 372 nm, 370 nm, 370 nm, 372 nm, 372 nm for X2, X3, X4, X5, X6, and X7, respectively. An extra absorption peak starts to be existed with Mn^{2+} ions doping in ZnO.

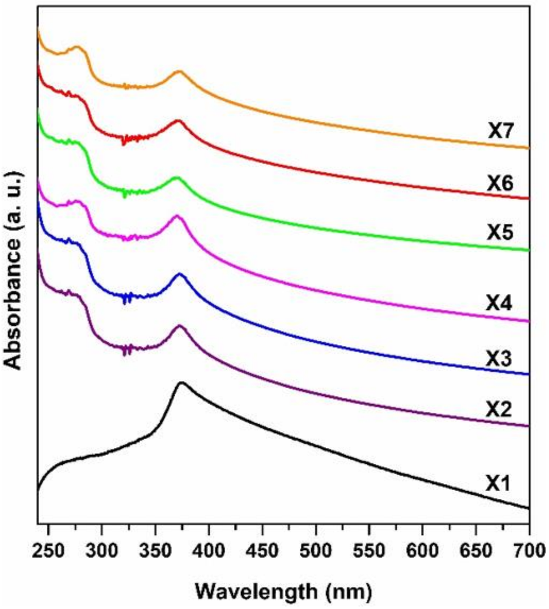

Fig. 8. UV-VIS absorbance spectra of ZnO:Mn nanoparticles depending on Mn concentration

The main part of our discussion is about photoluminescence of the ZnO and ZnO:Mn since there are quite different explanation especially about the origin of visible light emission in PL spectra. It is obvious that the concentration of defects should be reduced in order to fabricate highly efficient optoelectronic devices. Thus, firstly it is important to determine the origin of defects created in the structure in other words the origin of defect related emission in visible region. Besides, it is known that different techniques to produce nanomaterials play a role on morphology as well as different types of defects and following different luminescence spectra. Namely, different defects are responsible for the variable visible emissions. For instance, it was reported (Gong *et al.*, 2007) that red emission which takes place in the PL spectra at around (620 nm–780 nm) is originated by mainly either oxygen interstitials or oxygen vacancies. Besides, it was mentioned that oxygen vacancy has three possible charge states in following (Gong et. al., 2007): the neutral oxygen vacancy ($\boldsymbol{V_O^0}$), the singly ionized oxygen vacancy ($\boldsymbol{V_O^{\cdot}}$) and the doubly ionized oxygen vacancy ($\boldsymbol{V_O^{\cdot\cdot}}$). Since the single ionized state is thermodynamically unstable with respect to the first principle calculations (Erhart *et al.*, 2006; Janotti *et al.*, 2005), it is not possible for the oxygen vacancy to be existed in single ionized state. Further, the neutral oxygen vacancies having the lowest formation energy will dominate for ZnO nanoparticles in n-type bulk form. It was observed in the literature that the red-orange emission peak position at ~640–680 nm or ~1.8–1.9 eV was less commonly observed than green and yellow emissions (Studenikin *et al.*, 1998; Mei *et al.*, 2005; Vlasenko *et al.*, 2005; Radoi *et al.*, 2003; Wu *et al.*, 2006; El Hichou *et al.*, 2005) and the effect of excitation wavelength on green, yellow, and orange defect emission form ZnO nanostructures (Djurisic *et al.*, 2006).

In this study, the PL spectra of ZnO nanocrystals prepared for different growing time and doped with different Mn concentrations are measured at RT. In both of cases, the PL spectra consist of two peaks: first peak is occurred at ~370–400 nm (3.10–3.35 eV) know as typical UV emission peak, which is attributed to band-edge emission or donor-band excitation (Glushenkov *et al.*, 2007) and second one at ~640–660 nm (1.87–1.94 eV) visible light emission, red emission. It was reported (Alvi *et al.*, 2011) that the red emission of ZnO occurred between 620–750 nm could be attributed to oxygen interstitials (O_i) for the range from 620 nm to 690 nm and to oxygen vacancies (V_o) for the range from 690 nm to 750 nm. The UV peak known as exciton emission shift is due to crystal defects and Burstein-Moss Effect (Chang *et al.*, 2012). The long-wavelength shift is related to defects, while short-wavelength shift is related to Burstein Moss effect. That is, the band gap is expanded by the short wavelength shift (Chang *et al.*, 2012).

The intensity of the red-light emission at 650 nm increases drastically with increasing growing time except for the sample grown for 12 h. Thus, we can conclude that the 12 h sample has the lowest oxygen related defects in the samples of 6h, 24 h, and 36 h. On the other hand, it is difficult to observe a linear correlation between Mn concentration and so-called red peak emission intensity centered at ~650 nm. In this series, the undoped ZnO shows the lowest intensity and once it is doped $5x10^{-4}$ mole of Mn (X2) shows the strongest intensity. The PL intensity decreases with increasing concentration from $5x10^{-4}$ (X3) to $5x10^{-4}$ (X6) and then the intensity increases for X7.

Wei *et al.* (2010) calculated the intensity ratios of the UV to visible light emission peak as a function of annealing temperature. They concluded that the largest intensity ratio with the lowest defect emission was obtained by annealing at 700°C. The similar intensity ratios of our PL spectra are calculated and the results shows that the ratios of the samples 1 h and 12 h are very close to each other (0.0305 and 0.0302) and these are the values which are greater than those of the samples 6 h, 24 h, and 36 h (0.0185, 0.0125, and 0.0070). From the point of view of intensity ratio of PL spectra we can conclude that doping ZnO with Mn^{2+} ions creates oxygen related defects in the structure. The sample labeled with X6 shows the lowest oxygen related defects where as that of X2 shows the highest defects.

4. CONCLUSIONS

In the present work, the effects of growing time and Mn concentration on the photoluminescence and optical properties of ZnO nanocrystals synthesized by hydrothermal method have been investigated. It is concluded that the sample prepared for 36 h has the highest oxygen related defects whereas 1 h and 12 h samples have the lowest defects. Besides, doping Mn^{2+} ions creates similar defects in ZnO. However, there is no linear correlation observed between Mn^{2+} concentration and the defect concentration. While the sample X2 also has the highest oxygen related defects, the sample X6 has the lowest defects. We conclude that all of these oxygen related defects are originated by either oxygen interstitial or oxygen vacancies. In addition, these oxygen vacancies should be neutral oxygen vacancies and not by single ionized or doubly ionized oxygen vacancies existing in the structure. In the UV–visible spectra of ZnO the red shift is observed with increasing growing time. Doping Mn^{2+} ions in ZnO creates an extra peak at around 279 nm. However, increasing Mn^{2+} concentration does not change the UV-visible spectra significantly in ZnO:Mn samples.

REFERENCES

Achouri, F., Corbel, S., Balan, L., Mozet, K., Girot, E., Medjahdi, G., Ben, M., Ghrabi, A. and Schneider, R. (2016). “Porous Mn-doped ZnO nanoparticles for enhanced solar and visible light photocatalysis.” *JMADE*, Vol. 101, pp. 309–316.

Ahmed, S. A. (2017). “Structural, optical, and magnetic properties of Mn-doped ZnO samples.” *Results Phys.*, Vol. 7, pp. 604–610.

Altintas Yildirim, O., Arslan, H. and Sönmezoğlu, S. (2016). “Facile synthesis of cobalt-doped zinc oxide thin films for highly efficient visible light photocatalysts.” *Appl. Surf. Sci.*, Vol. 390, pp. 111–121.

Alvi, N. H., Hasan, K., Nur, O. and Willander, M. (2011). “The origin of the red emission in n-ZnO nanotubes / p-GaN white light emitting diodes.” *Nanoscale Research Lett.*, Vol. pp. 1–7.

Anandan, S., Vinu, A., Mori, T., Gokulakrishnan, N., Srinivasu, P., Murugesan, V. and Ariga, K. (2007). “Photocatalytic degradation of 2,4,6-trichlorophenol using lanthanum doped ZnO in aqueous suspension.” *Catal. Commun.*, Vol. 8, pp. 1377–1382.

Awad, M. A., Ahmed, A. M., Khavrus, V. O. and Ibrahim, E. M. M. (2015). “Tuning the morphology of ZnO nanostructure by in doping and the associated variation in electrical and optical properties.” *Ceram. Int.*, Vol. 41, No. 8, pp. 10116–10124.

Bahnemann, D. W., Kormann, C. and Hoffmann, M. R. (1987). “Preparation and characterization of quantum size zinc oxide: a detailed spectroscopic study.” *J. Phys. Chem.*, Vol. 91, No. 14, pp. 3789-3798.

Barzgari, Z., Ghazizadeh, A. and Zahra, S. (2016). “Preparation of Mn-doped ZnO nanostructured for photocatalytic degradation of Orange G under solar light.” *Res. Chem. Intermed.*, Vol. 42, No. 5, pp. 4303–4315.

Bhatia, S., Verma, N. and Bedi, R. K. (2017). “Sn-doped ZnO nanopetal networks for efficient photocatalytic degradation of dye and gas sensing applications” *Appl. Surf. Sci.*, Vol. 407, pp. 495–502.

Chang, Y. Q., Wang, P. W., Ni, S. L., Long, Y. and Li, X. D. (2012). “Influence of Co Content on Raman and Photoluminescence Spectra of Co Doped ZnO Nanowires.” *J. Mater. Sci. Technol.*, Vol. 28, No. 4, pp. 313–316.

Chauhan, R., Kumar, A. and Chaudhary, R. P. (2012). “Structural and photocatalytic studies of Mn doped TiO2 nanoparticles.” *Spectrochim. Acta – Part A Mol. Biomol. Spectrosc.*, Vol. 98, pp. 256–264.

Choudhury, S., Sain, S., Mandal, M. K., Pradhan, S. K. and Meikap, A. K. (2016). “Investigation of dielectric and electrical behavior of nanocrystalline Zn1−xMnxO (x = 0 to 0.10) semiconductors synthesized by mechanical alloying.” *Physica E*, Vol. 81, pp. 122 130.

Cohn, A.W., Kittilstved, K. R. and Gamelin, D. R. (2012). “Tuning the Potentials of “Extra” Electrons in Colloidal n-Type ZnO Nanocrystals via Mg2+ Substitution.” *J. Am. Chem. Soc.*, Vol. 134, No. 18, pp. 7937-7943.

Das, S. N. Moon, K. J., Kar, J. P., Choi, J. H., Xiong, J., Lee, T. and Myoung, J. M. (2010). “ZnO single nanowire-based UV detectors.” *Appl. Phys. Lett.*, Vol. 97, pp. 022103.

Deka, S. and Joy, P. A. (2007). “Synthesis and magnetic properties of Mn doped ZnO nanowires.” *Solid State Commun.*, Vol. 142, No. 4, pp. 190–194.

Dhara, A., Sain, S., Das, S. and Pradhand, S. K. (2018). “Microstructure, optical, dielectric and electrical characterizations of Mn doped ZnO nanocrystals synthesized by mechanical alloying.” *Ceramics International*, Vol. 44, pp. 7110-7121.

Djurisic, A. B., Leung, Y. H., Tam, K. H., Ding, L., Ge, W. K., Chen, H. Y. and Gwo, S. (2006). "Green, yellow, and orange defect emission from ZnO nanostructures: Influence of excitation wavelength." *Applied Physics Letters*, Vol. 88, No. 10, pp. 28–31.

Donkova, B., Dimitrov, D., Kostadinov, M., Mitkova, E. and Mehandjiev, D. (2010). “Catalytic and photocatalytic activity of lightly doped catalysts M:ZnO (M = Cu, Mn).” *Mater. Chem. Phys*., Vol. 123, pp. 563–568.

El Hichou, A., Addou, M., Ebothé, J., Troyon, M. (2005). “Influence of deposition temperature (Ts), air flow rate (f) and precursors on cathodoluminescence properties of ZnO thin films prepared by spray pyrolysis.” *J Lumines*, Vol. 113, pp. 183–190.

Emanetoglu, N. W., Gorla, C., Liu, Y., Liang, S. and Lu, Y. (1999). “Epitaxial ZnO piezoelectric thin films for saw filters.” *Mater. Sci. Semicond. Process*., Vol. 2, No. 3, pp. 247–252.

Erhart, P., Albe, K. and Klein, A. (2006). “First-principles study of intrinsic point defects in ZnO: Role of band structure, volume relaxation, and finite-size effects.” *Physical Review B - Condensed Matter and Materials Physics*, Vol. 73, No. 20, pp. 1–9.

Fabbiyola, S., Sailaja, V., Kennedy, J., Bououdina, L., Judith, M. and Vijaya, J., (2017). “Optical and magnetic properties of Ni-doped ZnO nanoparticles.” *Journal of Alloys and Compounds*, Vol. 694, pp. 522-531.

Fan, Z., Wang, D., Chang, P., Tseng, W. and Lu, J. G. (2004). “ZnO nanowire field-effect transistor and oxygen sensing property.” *Appl. Phys. Lett*., Vol. 84, pp. 5923.

Gong, Y., Andelman, T., Neumark, G. F., O’Brien, S. and Kuskovsky, I. L. (2007). “Origin of defect-related green emission from ZnO nanoparticles: effect of surface modification.” *Nanoscale Res. Lett*., Vol. 2, pp. 297–302.

Glushenkov, A. M., Zhang, H. Z., Zou, J., Lu, G. Q. and Chen, Y. (2007). “Efficient production of ZnO nanowires by a ball milling and annealing method,” *Nanotechnology*, Vol. 18 No. 17, pp. 175604 (6pp).

Janotti, A. and Van De Walle, C. G. (2005). “Oxygen vacancies in ZnO.” *Applied Physics Letters*, Vol. 87, No. 12, pp. 1–3.

Kaftelen, H., Ocakoglu, K., Thomann, R., Tu, S., Weber, S. and Erdem, E. (2012). “EPR and photoluminescence spectroscopy studies on the defect structure of ZnO nanocrystals.” *Phys. Rev. B*, Vol. 86, No. 1, pp. 1–9.

Kadam, A. N., Kim, T. G., Shin, D. S., Garadkar, K. M. and Park, J. (2017). “Morphological evolution of Cu doped ZnO for enhancement of photocatalytic activity.” *J. Alloys Compd*., Vol. 710, pp. 102–113.

Karmakar, R., Neogi, S. K., Banerjee, A. and Bandyopadhyay, S. (2012). “Structural; morphological; optical and magnetic properties of Mn doped ferromagnetic ZnO thin film.” *Appl. Surf. Sci*., Vol. 263, pp. 671–677.

Khanna, S. N., Rao, B. K., Jena, P. and Knickelbein, M. (2003). “Ferrimagnetism in Mn 7 cluster.” *Chem. Phys. Lett*., Vol. 378, No. 3, pp. 374–379.

Keis, K., Baue, C., Boschloo, G., Hagfeldt, A., Westermark, K., Rensmo, H. and Siegbahn, H. (2002). “Nanostructured ZnO electrodes for dye-sensitized solar cell applications.” *J. Photochem. Photobiol. A: Chem*., Vol. 148, pp. 57–64.

Koch, M. H., Timbrell, P. Y. and Lamb, R. N. (1995). “The influence of film crystallinity on the coupling efficiency of ZnO optical modulator waveguides.” *Semicond. Sci. Technol*., Vol. 10, pp. 1523–1527.

Law, M., Greene, L. E., Johnson, J. C., Saykally, R. and Yang, P. D. (2005). “Nanowire dye-sensitized solar cells.” *Nat. Mater*., Vol. 4, No. 6, pp. 455–459.

Li, W. J., Shi, E. W., Zheng, Y. Q. and Yin, Z. W. (2001). “Hydrothermal preparation of nanometer ZnO nanopowders.” *J. Mater. Sci. Lett*., Vol. 20, pp. 1381-1383.

Ma, Q., Lv, X., Wang, Y. and Chen, J. (2016). “Optical and photocatalytic properties of Mn doped flower-like ZnO hierarchical structures.” *Opt. Mater*., Vol. 60, pp. 86–93.

Martinson, A. B. F., Elam, J. W., Hupp, J. T. and Pellin, M. J. (2007). “ZnO Nanotube Based Dye-Sensitized Solar Cells.” *Nano Lett*., Vol. 7, No. 8, pp. 2183–2187.

Mei, Y. F., Siu, G. G., Fu, R. K. Y., Wong, K. W., Chu, P. K., Lai, C. W. and Ong, H. C. (2005). “Determination of nitrogen-related defects in N-implanted ZnO films by dynamic cathodoluminescence.” *Nuclear Instruments and Methods in Physics Research, Section B: Beam Interactions with Materials and Atoms*, Vol. 237, pp. 307–311.

Moontragoon, P., Pinitsoontorn, S. and Thongbai, P. (2013). “Mn-doped ZnO nanoparticles: Preparation, characterization, and calculation of electronic and magnetic properties.” *Microelectron. Eng*., Vol. 108, No. 3, pp. 158–162.

Motaung, D. E., Kortidis, I., Papadaki, D., Nkosi, S. S., Mhlongo, G. H., Wesley-Smith, J., Malgas, G. F., Mwakikunga, B. W., Coetsee, E., Swart, H. C., Kiriakidis, G. and Ray, S. S. (2014). “Defect-induced magnetism in un-doped and Mn-doped wide band gap Zinc oxide grown by aerosol spray pyrolysis.” *Appl. Surf. Sci*., Vol. 311, pp. 14-26.

Nasser, R., Othmen, W. B. H., Elhouichet, H. and Férid, M. (2017). “Preparation, characterization of Sb-doped ZnO nanocrystals and their excellent solar light driven photocatalytic activity.” *Appl. Surf. Sci*., Vol. 393, pp. 486–495.

Othman, A. A., Osman, M. A., Ibrahim, E. M. M., Ali, M. A. and Abd-Elrahim, A. G. (2017). “Mn-doped ZnO nanocrystals synthesized by sonochemical method: Structural, photoluminescence, and magnetic properties.” *Materials Science and Engineering: B*, Vol. 219, pp. 1-9.

Putri, N. A., Fauzia, V., Iwan, S., Roza, L., Umar, A. A.

and Budi, S. (2018). “Mn-doping-induced photocatalytic activity enhancement of ZnO nanorods prepared on glass substrates.” *Applied Surface Science*, Vol. 439, pp. 285–297.

Radoi, R., Fern ndez, P., Piqueras, J., Wiggins, M. S. and Solis, J. (2003). “Luminescence properties of mechanically milled and laser irradiated ZnO.” *Nanotechnology*, Vol. 14, pp. 794–798.

Saito, N., Haneda, H., Sekiguchi, T., Ohashi, N., Sakaguchi, I. and Koumoto, K. (2002). “Low‐Temperature Fabrication of Light‐Emitting Zinc Oxide Micropatterns Using Self‐Assembled Monolayers.” *Adv. Mater.*, Vol. 14, No. 6, pp. 418-421.

Saleh, R. and Djaja, N. F. (2014). “Transition metal-doped ZnO nanoparticles: Synthesis, characterization and photocatalytic activity under UV light.” *Spectrochim. Acta – Part A Mol. Biomol. Spectrosc.*, Vol. 130, pp. 581–590.

Samanta, A., Goswami, M. N. and Mahapatra, P. K. (2018). “Magnetic and electric properties of Ni-doped ZnO nanoparticles exhibit diluted magnetic semiconductor in nature.” *Journal of Alloys and Compounds*, Vol. 730, No. 399–407.

Schneider, J. J., Hoffmann, R. C., Engstler, J., Klyszcz, A., Erdem, E., Jakes, P., Eichel, R. A., Pitta-Bauermann, L. and Bill, J. (2010). “Synthesis, characterization, defect chemistry, and FET properties of microwave-derived nanoscaled zinc oxide.” *Chem. Mater.*, Vol. 22, No. 2203-2212.

Sekine, N., Chou, C. H., Kwan, W. L. and Yang, Y. (2009). “ZnO nano-ridge structure and its application in inverted polymer solar cell.” *Org. Electron*, Vol. 10, No. 8, pp. 1473–1477.

Studenikin, S. A., Golego, N. and Cocivera, M. (1998). “Fabrication of green and orange photoluminescent, undoped ZnO films using spray pyrolysis.” *Journal of Applied Physics*, Vol. 84, No. 4, pp. 2287–2294.

Tabib, A., Bouslama, W., Sieber, B., Addad, A., Elhouichet, H., Férid, M. and Boukherroub, R. (2017). “Structural and optical properties of Na doped ZnO nanocrystals: application to solar photocatalysis.” *Appl. Surf. Sci.*, Vol. 396, pp. 1528–1538.

Toloman, D., Mesaros, A., Popa, A., Raita, O., Silipas, T. D., Vasile, B. S., Pana, O. and Giurgiu, L. M. (2013). “Evidence by EPR of ferromagnetic phase in Mn-doped ZnO nanoparticles annealed at different temperatures.” *Journal of Alloys and Compounds*, Vol. 551, pp. 502-507.

Ullah, R. and Dutta, J. (2008). “Photocatalytic degradation of organic dyes with manganese doped ZnO nanoparticles.” *J. Hazard. Mater.*, Vol. 156, pp. 194–200.

Umar, K., Aris, A., Parveen, T., Jaafar, J., Abdul Majid, Z., Vijaya Bhaskar Reddy, A. and Talib, J. (2015). “Synthesis, characterization of Mo and Mn doped ZnO and their photocatalytic activity for the decolorization of two different chromophoric dyes.” *Appl. Catal. A Gen.*, Vol. 505, pp. 507–514.

Vijayalakshmi, K. and Sivaraj, D. (2015). “Enhanced antibacterial activity of Cr doped ZnO nanorods synthesized using microwave processing.” *RSC Adv.*, Vol. 5, pp. 68461–68469.

Vlasenko, L. S. and Watkins, G. D. (2005). “Optical detection of electron paramagnetic resonance for intrinsic defects produced in ZnO by 2.5-MeV electron irradiation in situ at 4.2 K.” *Physical Review B - Condensed Matter and Materials Physics*, Vol. 72, No. 3, pp. 1–12.

Wang, J., Yang, J., Han, N., Zhou, X., Gong, S., Yang, J., Hu, P. and Chen, Y. (2017). “Highly sensitive and selective ethanol and acetone gas sensors based on modified ZnO nanomaterials.” *Materials and Design*, Vol. 121, pp. 69–76.

Wang, J., Yang, P. and Wei, X. (2015). “High-Performance, Room-Temperature, and No-Humidity-Impact Ammonia Sensor Based on Heterogeneous Nickel Oxide and Zinc Oxide Nanocrystals.” *ACS Appl. Mater*. Interfaces, Vol. 7, No. 6, pp. 3816–3824.

Wang, N., Yang, Y. and Yang, G. (2011). “Great blue-shift of luminescence of ZnO nanoparticle array constructed from ZnO quantum dots.” *Nanoscale Res. Lett.*, Vol. 338, pp. 6.

Wei, S., Lian, J. and Wu, H. (2010). “Annealing effect on the photoluminescence properties of ZnO nanorod array prepared by a PLD-assistant wet chemical method.” *Mater. Charact.*, Vol. 61, No. 11, pp. 1239–1244.

Wu, L., Wu, Y., Pan, X. and Kong, F. (2006). “Synthesis of ZnO nanorod and the annealing effect on its photoluminescence property.” *Opt Mater.*, Vol. 28, pp. 418–422.

Yang, J., Li, X., Lang, J., Yang, L., Gao, M., Liu, X., Wei, M., Liu, Y. and Wang, R. (2011). “Effects of mineralizing agent on the morphologies and photoluminescence properties of Eu3+-doped ZnO nanomaterials.” *J. Alloys Compd.*, Vol. 509, No. 41, pp. 10025–10031.

Yildirimcan, S., Ocakoglu, K., Erat, S., Emen, F. M., Repp, S. and Erdem, E. (2016). "The effect of growing time and Mn concentration on the defect structure of ZnO nanocrystals: X-ray diffraction, infrared and EPR spectroscopy." *RSC Adv.*, Vol. 6, No. 45, pp. 39511–39521.

Turkish Journal of Engineering

Turkish Journal of Engineering (TUJE)
Vol. 3, Issue 2, pp. 76-91, April 2019
ISSN 2587-1366, Turkey
DOI: 10.31127/tuje.454978
Research Article

REGIONAL GEOELECTRICAL DIMENSIONALITY OF THE NORTHWESTERN PART OF TURKEY FROM MAGNETOTELLURIC TENSOR INVARIANTS

Fahriye Akar *[1] and Cemal Kaya [2]

[1] Erzincan University, Department of Construction Technologies, Erzincan, Turkey,
ORCID ID 0000-0002-8445-0353
fhrykcmzb@gmail.com

[2] Kayaç Yer Bilimleri, Private Company (Owner), Ankara, Turkey,
ORCID ID 0000-0002-1065-0205
cemal.kaya2010@hotmail.com

* Corresponding Author

Received: 23/08/2018 Accepted: 15/09/2018

ABSTRACT

In this study, measurements obtained through the first two profiles from the TÜBİTAK (The Scientific and Technological Research Council of Turkey) project titled "Research of the Crustal Structure of Northwestern Anatolia with Geophysical Methods" from 2007 were used. Magnetotelluric (MT) measurements were taken from 174 sites approximately every 3 km in the region between Zonguldak and Akşehir (Konya). Dimensionality analysis was conducted with the decomposition of the impedance tensor obtained through the measurement data from the two profiles. The relationship between the observed geo-electric behaviors, the geological structure of the area and the MT dimensionality changes were detected. Two-dimensional (2D) and three-dimensional (3D) structures were revealed as a result of the dimensionality analysis obtained through the MT data from the region located between Zonguldak and Akşehir. The dimensionality was observed to be complex in small periods due to the heterogeneous conductive materials close to the surface and 3D structures were observed to be predominant in high periods. Moreover, the dimensionality near the suture zones were observed to be more complex compared to other areas according to the dimensionality analysis results. The structures in the vicinity of the North Anatolian Fault were found out to be N-NE striking. This indicates the accuracy and reliability of the results.

Keywords: *Magnetotelluric Method, Geoelectric Dimensionality, Geoelectric Struture, Northwestern Anatolian*

1. INTRODUCTION

The MT data could be interpreted 1-, 2- or 3-dimensionally with the dimensionality analysis. Usually, the constants found through the decomposition of the tensor components obtained from the MT data measured at the site are used for determining the dimensionality. Distortions and strike directions of geo-electric structures can also be found via dimensionality analysis. MT data are affected by distortions that mask the dimensionality of earth electricity structures and this may lead to wrong interpretations. For the correct interpretation of the data in magnetotelluric method, distortions should be defined and kept away from the data. Therefore, a good dimensional analysis is necessary.

Dimensionality analysis is a significant part of the MT study. There are several methods used to determine the dimensionality of the underground structures and they are usually based on rotational invariants. Swift (1967), Berdichevsky and Dimitriev (1976), Bahr (1988), Bahr (1991), Lilley (1993, 1998a, 1998b) made classifications of dimensionality using groups of parameters calculated via the measured MT tensors. Ranganayaki (1984), Ingham (1988), Park and Livelybrooks (1989) revealed 1D structures using the impedance average. Swift (1967) researched whether structures were 2D or not by using MT data. Bahr (1988) researched whether the 3D structures and measured MT data were affected from distortions caused by small local anomalies or not. Fischer and Masero (1994) suggested 7 independent and 1 dependent invariables using the components defining impedance tensor. Szarka and Menvielle (1997) formed a group of MT tensor invariants to be used in dimensionality analysis by thoroughly examining the rotational features of MT tensor. Romo *et al*. (1999) used invariant parameters obtained through magnetic transfer function (tipper) to define 2D and 3D reactions. Weaver et al. (2000) made a definition of geoelectric dimensionality using the rotational invariants they obtained from the MT tensor. Caldwell et al. (2004) put forward the notion of MT phase tensor using the relation between the real and virtual parts of the MT tensor. In this study, the dimensionality analysis of the geologically complex region between Zonguldak and Akşehir was carried out with Wal invariants obtained from impedance tensor, using the measurements from 173 MT points (Weaver et al., 2000).

This study aimed at determining the dimensionality of geoelectric structure and strike directions in the study site, contributing to gathering more information on the geology of the site, which has a complex structure.

2. MT DATA ACQUISITION

North to East measurements were taken along the two profiles located in western Turkey in 2007 were used in this study. The first profile passes through Kıbrıscık, Kırbaşı, Beypazarı, Günyüzü, Çeltik, Yunak and Turgut; the second profile passes through Akçakoca, Düzce, Dokurcun Valley, Emirdağ, Bolvadin and Çay (Fig.1). Magnetotelluric (MT) measurements were taken from a total of 174 points, approximately every 3 km along both profiles. Fourier transforms were applied on the measured time series magnetotelluric data, impedances were obtained in frequency setting and files were created in EDI (Electrical Data Interchange) standards.

Potential electrodes consisting of four nonpolarized conductive ceramic cables containing lead-lead chloride ($Pb\text{-}PbCl_2$) were used to measure the electric field.
The distance between electrodes ranges between 50 to 200 m depending on the site conditions. The electrodes in North-South direction are called Ex and the ones in East-West direction are called Ey. Electrodes are placed in approximately 25 cm deep pits filled with mud.

The magnetic field is measured with induction coils that has a conductor in the core. Coils used in this study are sensitive to the range between 400 Hz and 0.00002 Hz. The horizontal coils are placed in parallel with the north-east direction. The coil placed as the free end pointing towards north is called hx and the coil placed as the free end pointing towards east is called hy. The third coil called hz should be placed vertically in a pit deep enough to cover the whole coil, as delicately as possible.

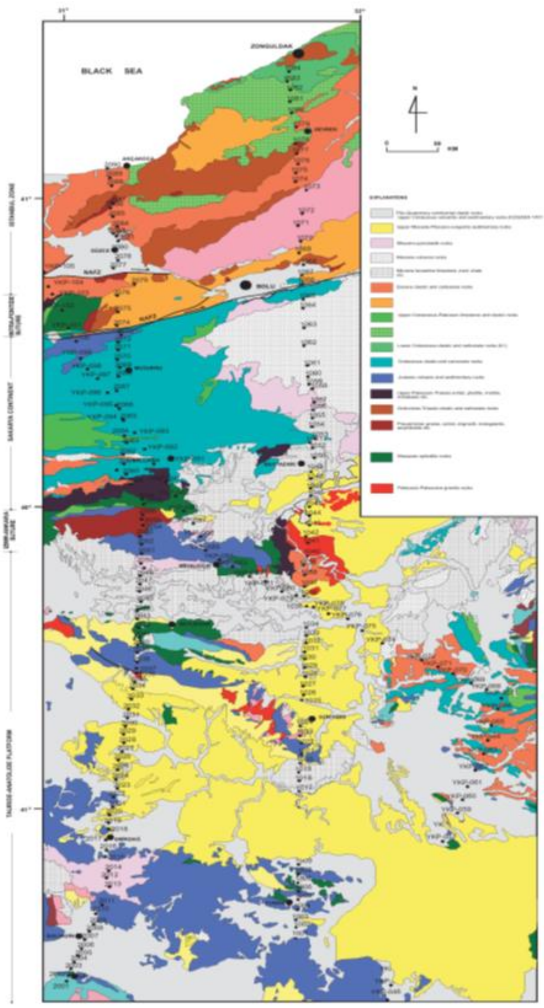

Fig. 1. Geologic map of the study site, drawn based on the 1/500,000 scale Geological Map of Turkey Ankara, Zonguldak map sheets, General Directorate of MTA (Mineral Research and Exploration) 2002.

3. GEOLOGICAL SETTING

It is generally accepted that there are 6 main lithospheric plates in Turkey, namely Istranca, İstanbul and Sakarya zones, Torid-Anatolid Block, Kırşehir Massif and ArabicPlatform (Şengör and Yılmaz 1981; Şengör et al. 1982; Okay 1989; Okay et al. 1994). The main continental pieces and suture zones in and around Turkey are shown in Fig. 2.

The region in the Northwest Anatolia extending from the Black Sea to Araç-Daday-İnebolu is known as the İstanbul Zone (Okay, 1989). Şengör and Yılmaz (1981), Şengör et al. (1984), Tüysüz (1990) stated that the İstanbul Zone was a pre-Dopper nappe; Okay et al. (1995) stated that it settled in its current location after rifting from the Moesian platform in Cretaceous period; Yılmaz et al. (1997) stated that the Sakarya Continent and Istranca Zone united due to Paleotethys and its continuation Intra-Pontide oceans coming together between the end of the Triassic period and the Cretaceous period; and Tüysüz (1999) stated that the east end of the İstanbul Zone was bordered by the Intrapontide Suture.

Intra-Pontide Suture constitutes the border between the İstanbul Zone and Sakarya Continent. Currently, it corresponds to the North Anatolian Fault, which is a post-Miocene strike-slip fault (Okay & Tüysüz, 1999; Okay Güncüoğlu 2004). E-W trending Sakarya Zone located between the Intra-Pontide suture and İzmir-Ankara suture lies along the profiles towards south. Triassic subduction-accumulation units named as the Karakaya Complex include the lower section of the Permo-Triassic metabasite-marble-phyllite series with exotic Triassic lenses of eclogite (Monod et al., 1996; Okay and Monié, 1997).

İzmir – Ankara – Erzincan Suture, which is one of the most important sutures of Anatolia, represents the closing of the north arm of the Tethys Ocean between Laurasia and Gondwana from late Paleozoic to early Tertiary period. It separates the Sakarya Continent from the Anatolide-Tauride Block in north to south direction (Okay and Tüysüz, 1999). Tavşanlı Zone is a subsection of the Anatolide-Tauride Block (Fig. 2). Together with the Neotethyan Ocean, it is a metamorphic arch formed due to the subduction of the northern edge of the Anatolide-Tauride Block (Okay, 1982, 1986; Sherlock et al., 1999; Droop et al., 2005).

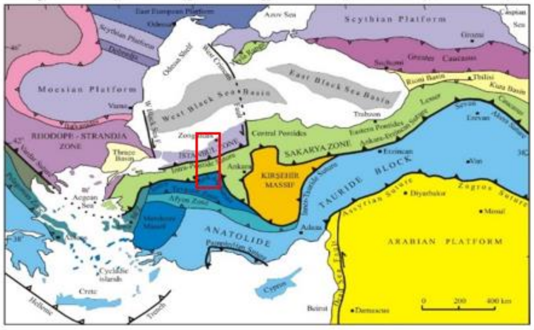

Fig. 2. Tectonic map of the eastern Mediterranean region showing large troops and suture borders. Full triangles indicate dipole polarity, red rectangular shows study area (Okay and Tüysüz, 1999).

MT profiles start from the Tavşanlı Zone, pass through İzmir-Ankara-Erzincan Suture zone, Sakarya zone and the Intra-Pontide suture and end at the İstanbul Zone.

4. WAL DIMENSION ANALYSIS

Weaver et al. (2000) aimed at finding out information about the underground dimensionality by producing rotational invariant parameters (WAL invariants) from the MT tensor. WAL invariant linear combinations of the complex parameters obtained through decomposition of the real and imaginary parts of the MT tensor, which is a complex number, was found with $\zeta_i = \xi_i + \eta_i i$ (i=1,4). These complex parameters are given as follows;

$$\zeta_1 = (M_{xx} + M_{yy})/2 \, , \tag{1}$$

$$\zeta_2 = (M_{xy} + M_{yx})/2 \, , \tag{2}$$

$$\zeta_3 = (M_{xx} - M_{yy})/2 \, , \tag{3}$$

$$\zeta_4 = (M_{xy} - M_{yx})/2 \tag{4}$$

From here, the MT tensor is defined with:

$$M = \begin{pmatrix} \zeta_1 + \zeta_3 & \zeta_2 + \zeta_4 \\ \zeta_2 + \zeta_4 & \zeta_1 - \zeta_3 \end{pmatrix} = \begin{pmatrix} \xi_1 + \xi_3 & \xi_2 + \xi_4 \\ \xi_2 - \xi_4 & \xi_1 - \xi_3 \end{pmatrix} + i \begin{pmatrix} \eta_1 + \eta_3 & \eta_2 + \eta_4 \\ \eta_2 + \eta_4 & \eta_1 - \eta_3 \end{pmatrix}$$
(5)

Thus, WAL invariants are as follows:

$$I_1 = (\xi_1^{\,2} + \xi_4^{\,2})^{1/2} \text{ (m/s)}, \tag{6}$$

$$I_2 = (\eta_1^{\,2} + \eta_4^{\,2})^{1/2} \text{ (m/s)}, \tag{7}$$

$$I_3 = \frac{(\xi_2^{\,2} + \xi_3^{\,2})^{1/2}}{I_1} \, , \tag{8}$$

$$I_4 = \frac{(\eta_2^{\,2} + \eta_3^{\,2})^{1/2}}{I_2} \, , \tag{9}$$

$$I_5 = \frac{\xi_4 \eta_1 + \xi_1 \eta_4^{\,2}}{I_1 I_2} \, , \tag{10}$$

$$I_6 = \frac{\xi_4 \eta_1 - \xi_1 \eta_4}{I_1 I_2} = d_{41} \, , \tag{11}$$

$$I_7 = (d_{41} - d_{23})/Q \, . \tag{12}$$

d_{ij} and Q parameters are dependent on ξ_i, η_i variants and the other invariants identified above and are defines as such:

$$d_{ij} = \frac{\xi_i \eta_j - \xi_j \eta_i}{I_1 I_2}, \text{ (i=1,…,4 ve j=1,…,4)} \quad (13)$$

$$Q = \left[\left(d_{12} - d_{34}\right)^2 + \left(d_{13} + d_{24}\right)^2 \right]^{1/2} \quad (14)$$

I_1 and I_2 invariants are used for finding the resistivity and phase of a 1D place:

$$\rho_{1D} = \mu_0 \frac{(I_1^{\,2} + I_2^{\,2})}{\omega}, \quad (15)$$

$$\varphi_{1D} = \arctan(\frac{I_2}{I_1}) \quad (16)$$

The requirements of I_3 I_4 I_5 I_6 I_7 and Q invariants necessary for the detection of galvanic distortion and dimensionality (Weaver *et al.*, 2000) are given in Table 1.

Table 1 WAL invariants and dimensional criteria (Weaver et al., 2000)

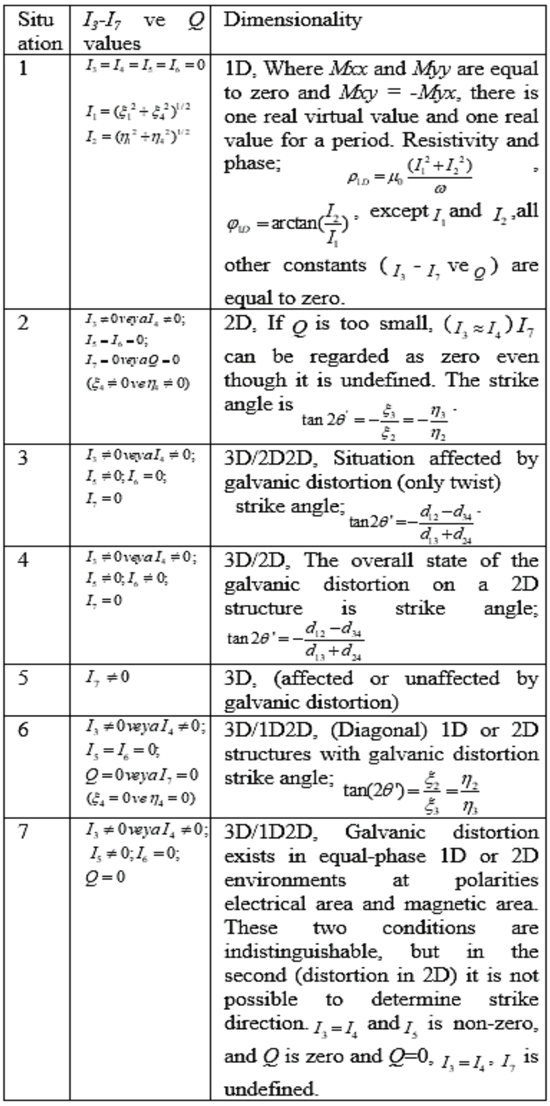

Situation	I_3-I_7 ve Q values	Dimensionality
1	$I_3 = I_4 = I_5 = I_6 = 0$ $I_1 = (\xi_1^{\,2} + \xi_4^{\,2})^{1/2}$ $I_2 = (\eta_1^{\,2} + \eta_4^{\,2})^{1/2}$	1D, Where *Mxx* and *Myy* are equal to zero and *Mxy* = -*Myx*, there is one real virtual value and one real value for a period. Resistivity and phase; $\rho_{1D} = \mu_0 \frac{(I_1^2 + I_2^2)}{\omega}$, $\varphi_{1D} = \arctan(\frac{I_2}{I_1})$, except I_1 and I_2, all other constants (I_3 - I_7 ve Q) are equal to zero.
2	$I_3 = 0 veya I_4 = 0;$ $I_5 = I_6 = 0;$ $I_7 = 0 veya Q = 0$ $(\xi_4 \neq 0 ve \eta_1 \neq 0)$	2D, If Q is too small, $(I_3 \approx I_4)$ I_7 can be regarded as zero even though it is undefined. The strike angle is $\tan 2\theta' = -\frac{\xi_3}{\xi_2} = -\frac{\eta_3}{\eta_2}$.
3	$I_3 \neq 0 veya I_4 \neq 0;$ $I_5 \neq 0; I_6 = 0;$ $I_7 = 0$	3D/2D2D, Situation affected by galvanic distortion (only twist) strike angle; $\tan 2\theta' = -\frac{d_{12} - d_{34}}{d_{13} + d_{24}}$.
4	$I_3 \neq 0 veya I_4 \neq 0;$ $I_5 \neq 0; I_6 \neq 0;$ $I_7 = 0$	3D/2D, The overall state of the galvanic distortion on a 2D structure is strike angle; $\tan 2\theta' = -\frac{d_{12} - d_{34}}{d_{13} + d_{24}}$
5	$I_7 \neq 0$	3D, (affected or unaffected by galvanic distortion)
6	$I_3 \neq 0 veya I_4 \neq 0;$ $I_5 = I_6 = 0;$ $Q = 0 veya I_7 = 0$ $(\xi_4 = 0 ve \eta_4 = 0)$	3D/1D2D, (Diagonal) 1D or 2D structures with galvanic distortion strike angle; $\tan(2\theta') = \frac{\xi_2}{\xi_3} = \frac{\eta_2}{\eta_3}$
7	$I_3 \neq 0 veya I_4 \neq 0;$ $I_5 \neq 0; I_6 = 0;$ $Q = 0$	3D/1D2D, Galvanic distortion exists in equal-phase 1D or 2D environments at polarities electrical area and magnetic area. These two conditions are indistinguishable, but in the second (distortion in 2D) it is not possible to determine strike direction. $I_3 = I_4$ and I_5 is non-zero, and Q is zero and Q=0, $I_3 = I_4$, I_7 is undefined.

5. DIMENSION OF THE REGION BETWEEN ZONGULDAK AND AKSEHIR

I_1 , I_2 , I_3 , I_4 , I_5 , I_6 , I_7 and Q values, strike directions and distortion parameters of the WAL invariants developed by Weaver et al. (2000) were calculated at 80 frequency for each measurement. Maps that display the distribution of WAL invariant values in different locations and different periods in the profiles were created. In addition to these, the dimensionality types in the 174 stations along profile 1 and profile 2 for different periods were mapped. Thus, contour maps showing the distribution of the WAL invariants in different depths were formed and analyzed. Lastly, pseudo-sections were created using WAL invariants, vertical axis being the period and horizontal axis being the distance.

In order to show the change in the values of WAL invariants acquired in the logarithmic period bands for MT data and each measurement; and to show the values used in dimensionality, KBA is contoured as a map. The figures below show the contour maps of the WAL invariants in fixed periods such as T=0.01, 0.1, 1, 10, 100, 1000s.

Fig. 3 shows the change of I_3 for logarithmic periods. According to this figure, I_3 is usually low through both profiles in T=0.01s and T=0.1s. While I_3 has a high value in T=1s map in the northern section of the 1st profile and the middle of the 2nd profile, it has low values in other parts. I_3 usually has high values in T=1s, T=10s and T=100s. I_3 value is again usually high in T=1000s in the northern section of the 1st profile and middle of the 2nd profile, while it is low in other parts.

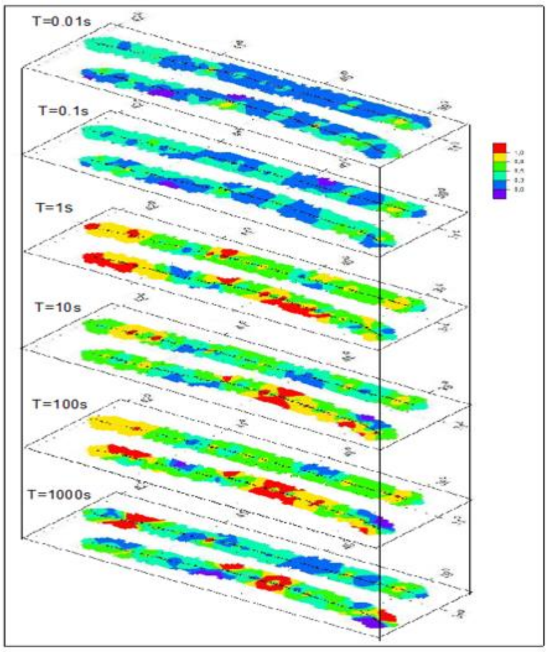

Fig. 3. Contour maps of the WAL constant I_3 at T = 0.01, T = 0.1, T = 1, T = 10, T = 100 and T = 1000 periods.

Fig. 4 shows the changes of I_4 values in the maps prepared for the logarithmic periods. I_4 values are high in the middle section of the 2nd profile for the periods

T=0.01s, T=1s and T=10s. In these periods, values are usually low in the 1st profile. *I₄* values are low in the T=0.1s in both profiles. While *I₄* values are usually high throughout the 2nd profile for T=1000s, they drop in the northern section of the 1st profile.

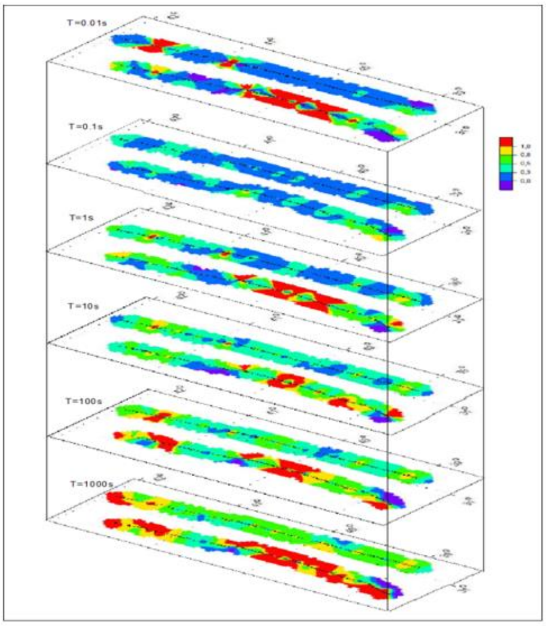

Fig. 4. Contour maps of the WAL constant I_4 at T = 0.01, T = 0.1, T = 1, T = 10, T = 100 and T =1000.

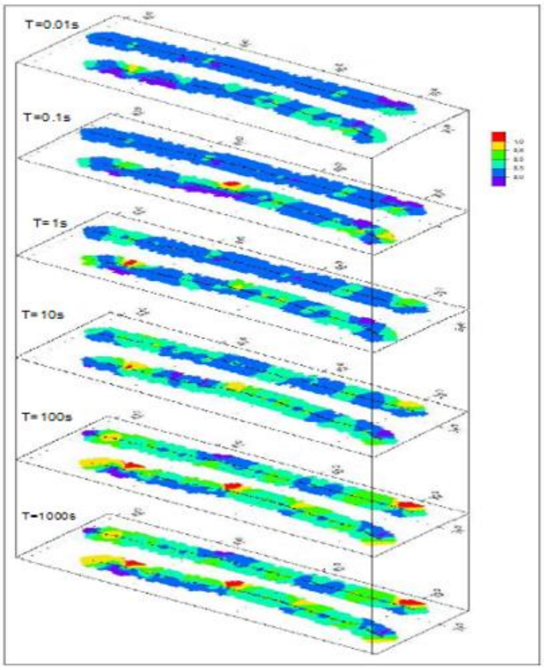

Fig. 5. Contour maps of the WAL constant I_5 at T = 0.01, T = 0.1, T = 1, T = 10, T = 100 and T =1000.

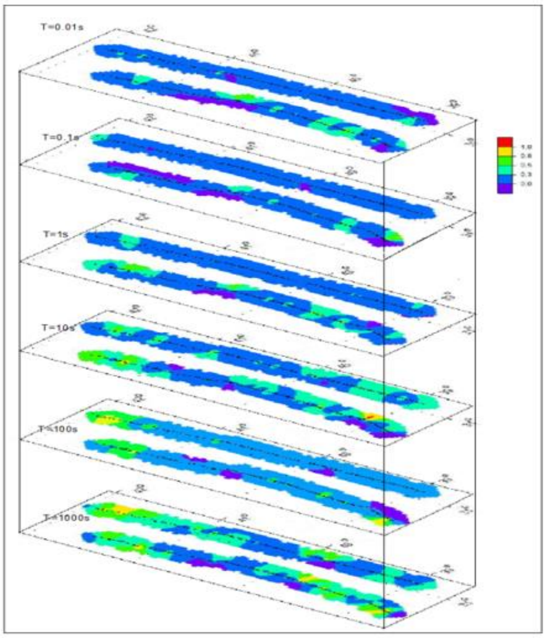

Fig. 6. Contour maps of the WAL constant I_6 at T = 0.01, T = 0.1, T = 1, T = 10, T = 100 and T =1000.

When the changes in I5 in the stated fixed periods (Fig. 5) are analyzed, it is observed that the values in the first three maps are usually high and gradually increases in the other maps. The changes in I6 throughout the 1st Profile and the 2nd Profile are shown in Fig. 6. According to the figure shown, I6 values in T=0.01s, T=0.1s and T=1s are usually low throughout both profiles. However, in T=10s and T=100s maps, I6 value increases in the north of the 1st and 2nd Profiles. While I6 value also increases in both the northern and southern sections of the 1st and 2nd Profiles, it is usually low in the middle section.

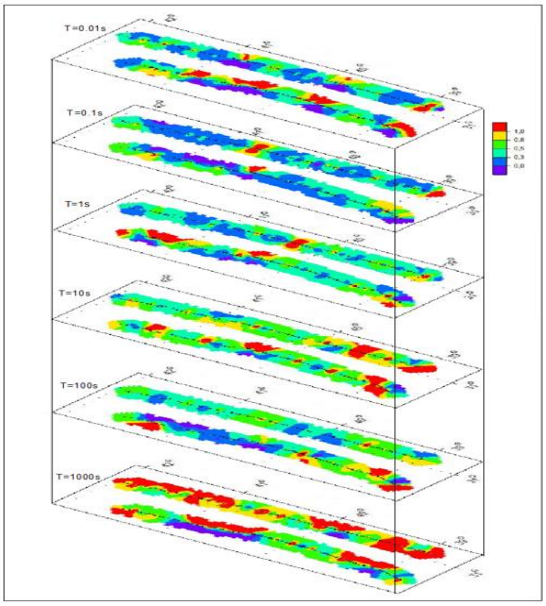

Fig. 7. Contour maps of the WAL constant I_7 at T = 0.01, T = 0.1, T = 1, T = 10, T = 100 and T = 1000 periods.

Changes in the value in specific fixed periods throughout the 1st Profile and the 2nd Profile are shown in Fig. 7. Changes are observed in I7 values in T=0.01s and T=0.1s throughout both profiles. While I7 value is observed to be usually high in T=1s in the south of the 1st and the 2nd Profile decreasing towards the north, it is also observed that the I7 value increases again in the northern section of the 2nd Profile. I7 values are usually high in T=10s, T=100s and T=1000s but I7 values are low in the northern section of the 2nd Profile in T=100s.

The changes in *Q* throughout the 1st Profile and the 2nd Profile are shown in Fig. 8. According to the figure, there are high values in the northern section of the 1st Profile while there are low values in the other sections. The *Q* values are high in the middle section of the 2nd Profile while they are low in the other sections. *Q* values are low throughout the 1st Profile in T=0.1. The values are also low in the northern section of the 2nd Profile but high in the other sections. The distribution in T=1s is similar to that in T=0.01s. In T=10s, there are usually low values in the 1st Profile while high values are observed in the northern section of the 2nd Profile. Values are usually low in the 1st Profile in T=100s and T=1000s. While the *Q* values are high in the northern section of the 2nd Profile and in the inner sections in T=100s, they are low in the other sections. *Q* values are high throughout the 2nd Profile in T=1000s.

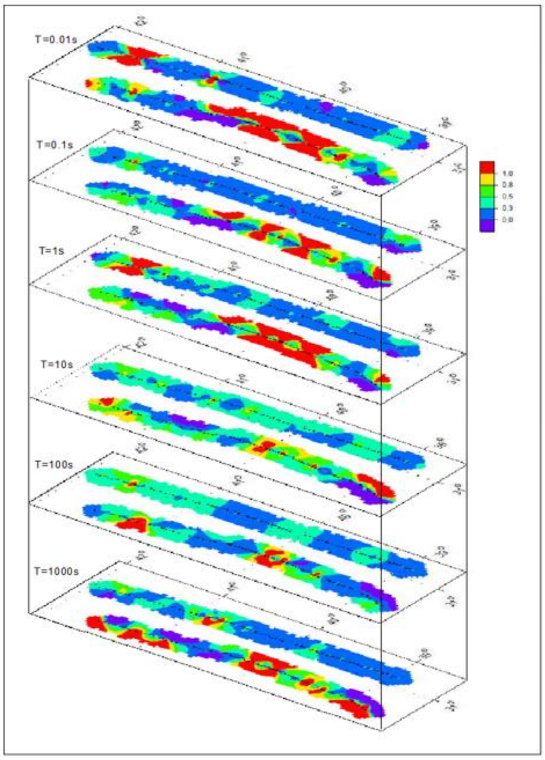

Fig. 8. Contour maps of the WAL constant *Q* for periods T = 0.01, T = 0.1, T = 1, T = 10, T = 100 and T = 1000.

6. DIMENSIONALITY ANALYSIS OF STUDY AREA

In this chapter, dimensionality analysis was performed for each point in all periods similar to the study by Marti (2004). $\tau = 0.15$ and $\tau_Q = 0.1$ threshold values tested and applied by Marti et al. (2004) for WAL invariants were used for determining the dimensionality. Because, WAL invariants can never be equal to zero (Weaver et al., 2000). Dimensionality maps were obtained by grouping the results on logarithmic period bands. The average strike directions for 2D and 3D/2D regions were drawn along with their standard deviations. Strike directions were scaled inversely proportional to error values. In short periods, there is complexity in dimensionality due to the local shallow materials that cause distortion in the measured data. Dimensionality is less complex in the long periods compared to the short ones.

WAL criteria were taken into consideration in this calculation. The reason for WAL invariants to be used instead of other methods is that it uses all the information obtained from the MT tensor and identifies dimensionality accordingly.

It is observed in Fig. 9 that the 1st band (0.001-0.01) is usually represented by 3-Dimensionality and 2-Dimensionality. When analyzed in detail, it is observed that there are 3D /2D and 2D structures in NE-SW strike directions in the first ten MT stations around Turgut (Konya) located on the Tauride-Anatolide Block in the south. However, the area between the points1010-1020, around Çeltik, is 1D. Dimensionality changes between the Tauride-Anatolide Block and the Sakarya Continent at the İzmir-Ankara Suture Zone and displays 3/2/1 dimensionality. There are 2D structures with NE-SW strike directions on points 1035 and 1036. 3D/2D, 3D, 1D structures are observed moving towards north. Some NE-SW trending 2D structures are observed near the Çeltikçi fault zone in parallel to the fault zone. The southwest of Kıbrıscık is represented by 1 Dimensionality. Moving towards north, the dimensionality becomes complex again near Bolu and 1D, 3D, NE-SW trending 3D/2D and 2D structures are noticed. This section corresponds to the Intra-Pontide Suture located between the Sakarya Continent and İstanbul Zone. Although there are some 1D, N-S trending 3D/2D structures are observed in some parts around Devrek and Zonguldak located at the northernmost section of the 1st Profile, there are also some 3D structures in some parts.

When the second profile in Fig. 9 is analyzed it is observed that most of the points located on the Tauride-Anatolide block, the southernmost section on the map, are 3D. On the inner section of the map, on points 2028-2036, the dimensionality is 1D and a change is observed around the Eskişehir fault zone. In this region there are 3D, 3D/2D/1D structures are located and there are also some 2D and 3D/2D structures with different strike directions considered to be due to other curves and faults of different trends. Beylikova vicinity and the west of Mihalıççık are represented by 1 Dimensionality. There are some 3D structures between points 2050-2058. In the southwest of Nallıhan, dimensionality is 3D, 3D/2D/1D, 1D and there are E-W trending 3D/2D structures. Considering that the dimensionality changes significantly in this region, it could be said that this region is similar to the İzmir-Ankara suture zone.

Between the points 2062-2066, there are usually NE-SW trending 3D/2D structures with different angles. There are 3D, 1D and NE-SW trending 2D structures near the North Anatolian Fault zone. Moving towards the north, 3-Dimensionality is more dominant between the Karadere Kaynaşlı Mengen Sub Fault Zone and Akçakoca.

In Fig. 10, results of the dimensionality analysis obtained from the WAL invariants on T=0.01-0.1s period band for measurement points 1001-1084 from south to north throughout the 1st Profile. When this figure is analyzed, 2D structures are observed between points 1001-1008 at the southernmost section of the profile. These structures also display strike directions of N19E and N46E. In the section between points 1009 and 1020 there are some 2D and 1D structures with strike directions of N46E and N82E. The structures between points 1020-1025 are 3D. Most of the structures between points 1025-1037 are 1D. While there are mostly 3D structures between stations 1038-1045, there are also some 3D/2D structures with N65E and N26E strike directions. The dimensionality between points 1046-1065 is usually 3D/2D. The strike directions of these structures range between N32E and N83E from south to north. The structures between points 1065-1072 are 1D, 3D/2D and 3D. The dimensionality of points 1072, 1073 and 1074 is 2D and the strike direction of these structures is N71E. There are usually 3D structures between points 1075-1084 located at the northernmost section of the profile and there are some 3D/2D/1D structures at some points.

Fig. 10 shows the dimensionality analysis results obtained from WAL parameters on the T=0.01-0.1 period band for measurement points 2001-2090 throughout the 2nd Profile from south to north. According to this figure, there are 3D structures affected by the galvanic distortion in places between measurement points 2001-2008 at the southernmost point of the profile. The dimensionality between points 2008-2014 is 3D/2D/1D and 2D. The places between points 2014-2029 are generally 3-Dimensional; however, there are also 3D/2D structures with N81E strike direction near the measurement point 2042. The dimensionality between points 2045-2050 is 1D. It is observed that there are 3D structures; 2D structures with N54E strike direction; 3D/2D structures with N20E strike direction and 3D/2D/1D structures between points 2050-2060. In the region where points 2060-2076 are located there are 3D/2D structures with N25E strike direction; 2D structures with N71E strike direction and 1D structures in some parts; however, the region is mostly represented by 3D structures. Dimensionality of all points on the İstanbul zone, which is located at the northernmost section of the 2nd Profile, is 3D.

Fig. 11 shows the dimensionality analysis results obtained from WAL parameters on T=0.1-1s period band for measurement points 1001-1084 throughout the 1st Profile, from south to north. According to this figure, the dimensionality between the first points 1001-1012 on the Tauride-Anatolide Block located at the southern most section of the 1st Profile on the 3rd band is 3D. While the dimensionality between points 1012-1020 is mainly 1D, there are also 2D structures with N78E strike direction between points 1013 and 1014. The dimensionality between points 1020-1027 is generally 3D. There are 1D and 3D structures between points 1027 and 1040. The dimensionality of the places between points 1040-1066 is complex with 1D structures, 2D structures with N60E strike angle and 3D/2D, 3D, 3D/2D/1D structures with N50E strike direction. In addition, there are generally 3D/2D structures with N55E strike direction between points 1066-1073. However, point 1072 is 2D and its strike direction is N73E. The dimensionality between points 1073-1084 located at the northernmost section of the profile on the İstanbul Zone is 3D.

Fig. 11 shows the dimensionality analysis results obtained from WAL parameters on T=0.1-1s period band for measurement points 2001-2090 throughout the 2nd Profile, from south to north. According to this figure, on the 3rd band there are usually 3D structures between points 2001-2012 located at the southernmost section of the 2nd Profile and there are some 2D and 3D/2D structures, as well. The dimensionality between points 2012-2039 is 3D. There are 3D/2D structures with N35E strike direction at points 2039, 2040 and 2041. Points 2042, 2043, 2044 are 3D and points 2045, 2046 and 2047 are 1D. There are generally 3D structures between points 2047-2065. There are 3D/2D structures with N60E strike direction between points 2065-2070. There are 3D structures at 2070-2090 stations.

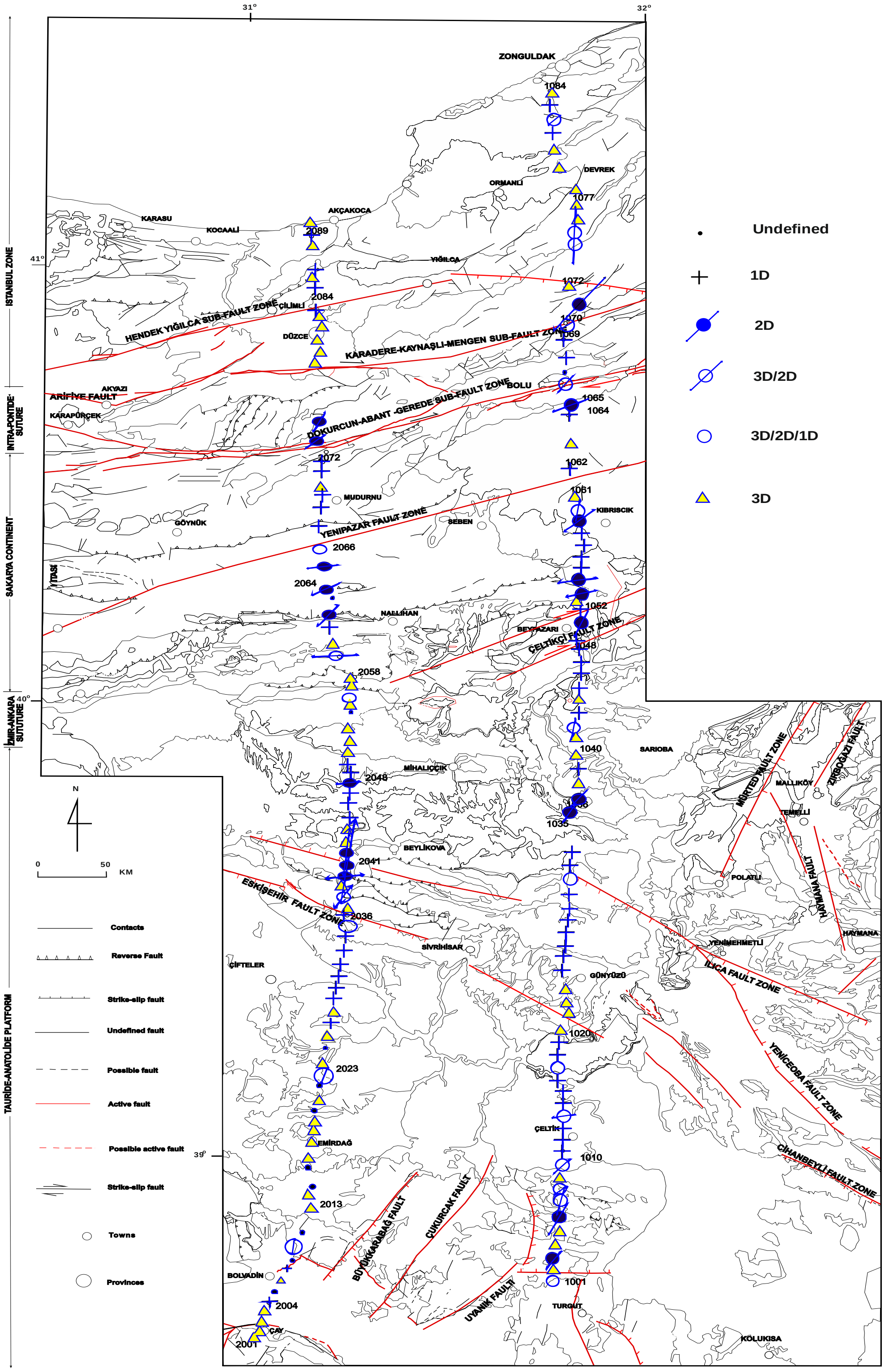

Fig. 9. Shows the KBA dimensionality analysis results on T=0.001s-0.01s band. Arrows show the strike direction. 3D/2D twist and 3D/2D are drawn as a single incident (3D/2D). Strike directions were scaled inversely proportional to error values. Certain signes are used for the existence of certain structures.

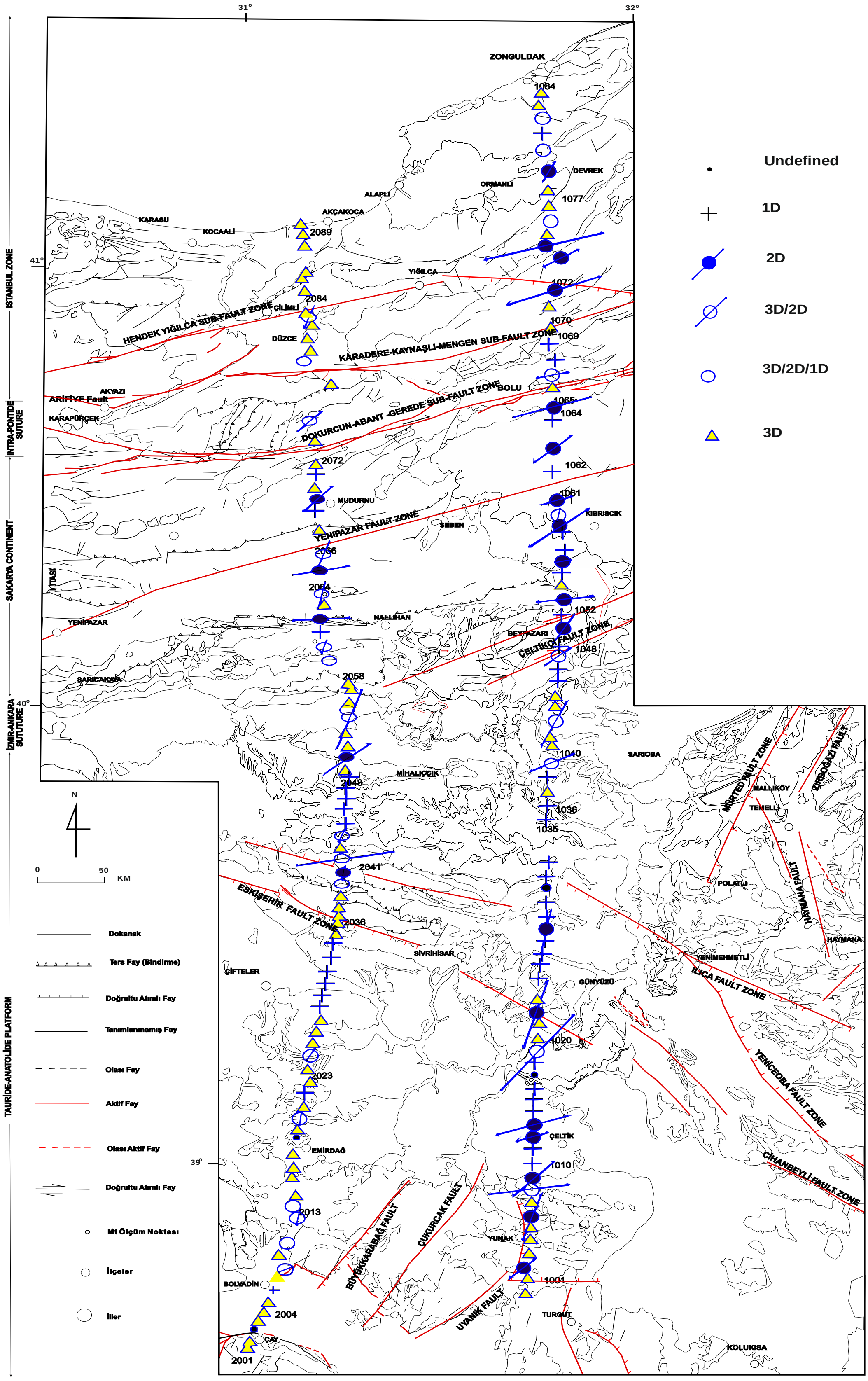

Fig.10. Shows the KBA dimensionality analysis results on T=0.0s-0.01s band. Arrows show the strike direction. 3D/2D twist and 3D/2D are drawn as a single incident (3D/2D). Strike directions were scaled inversely proportional to error values. Certain signes are used for the existence of certain structures.

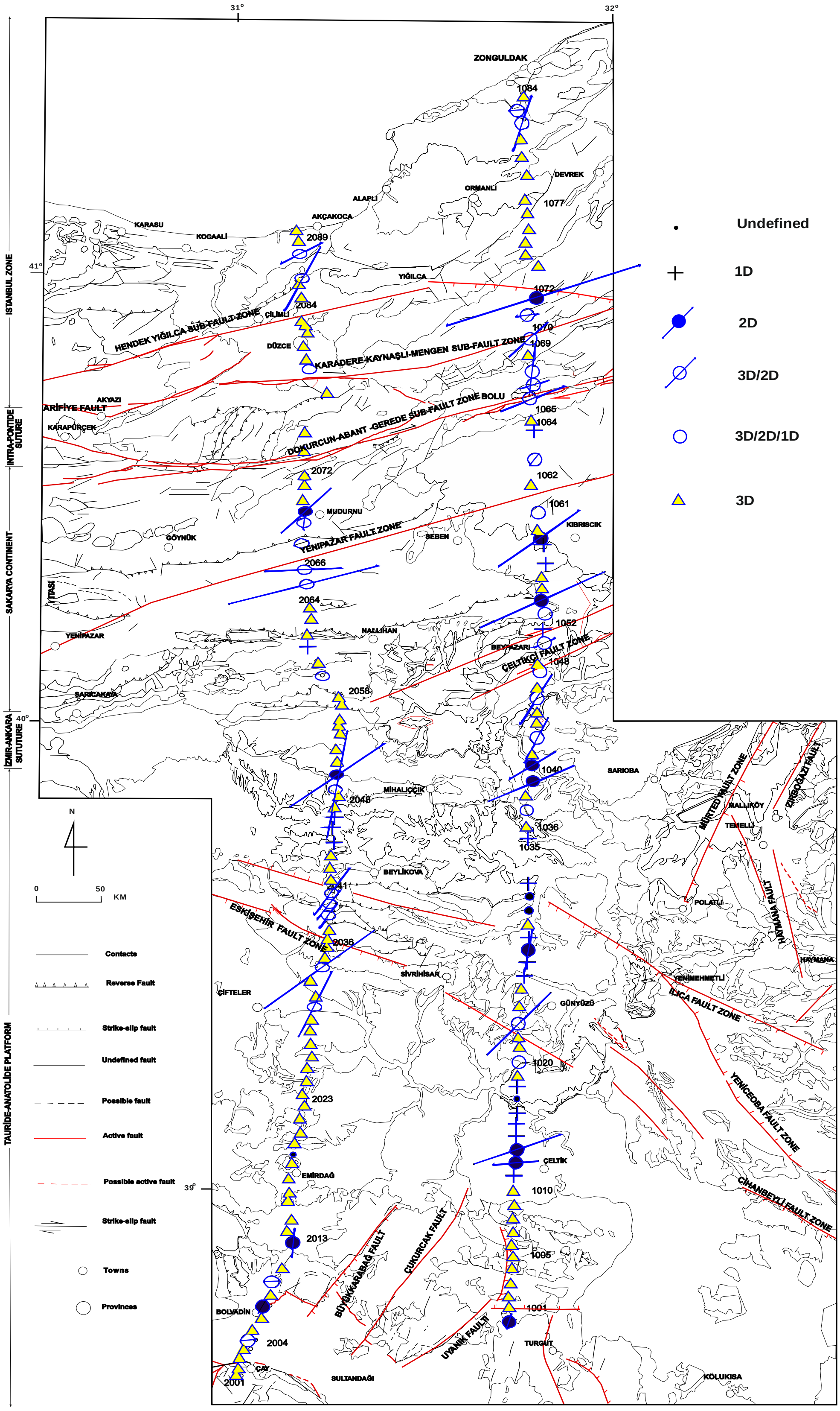

Fig. 11. Shows the KBA dimensionality analysis results on T=0.0s-0.01s band. Arrows show the strike direction. 3D/2D twist and 3D/2D are drawn as a single incident (3D/2D). Strike directions were scaled inversely proportional to error values. Certain signes are used for the existence of certain structures.

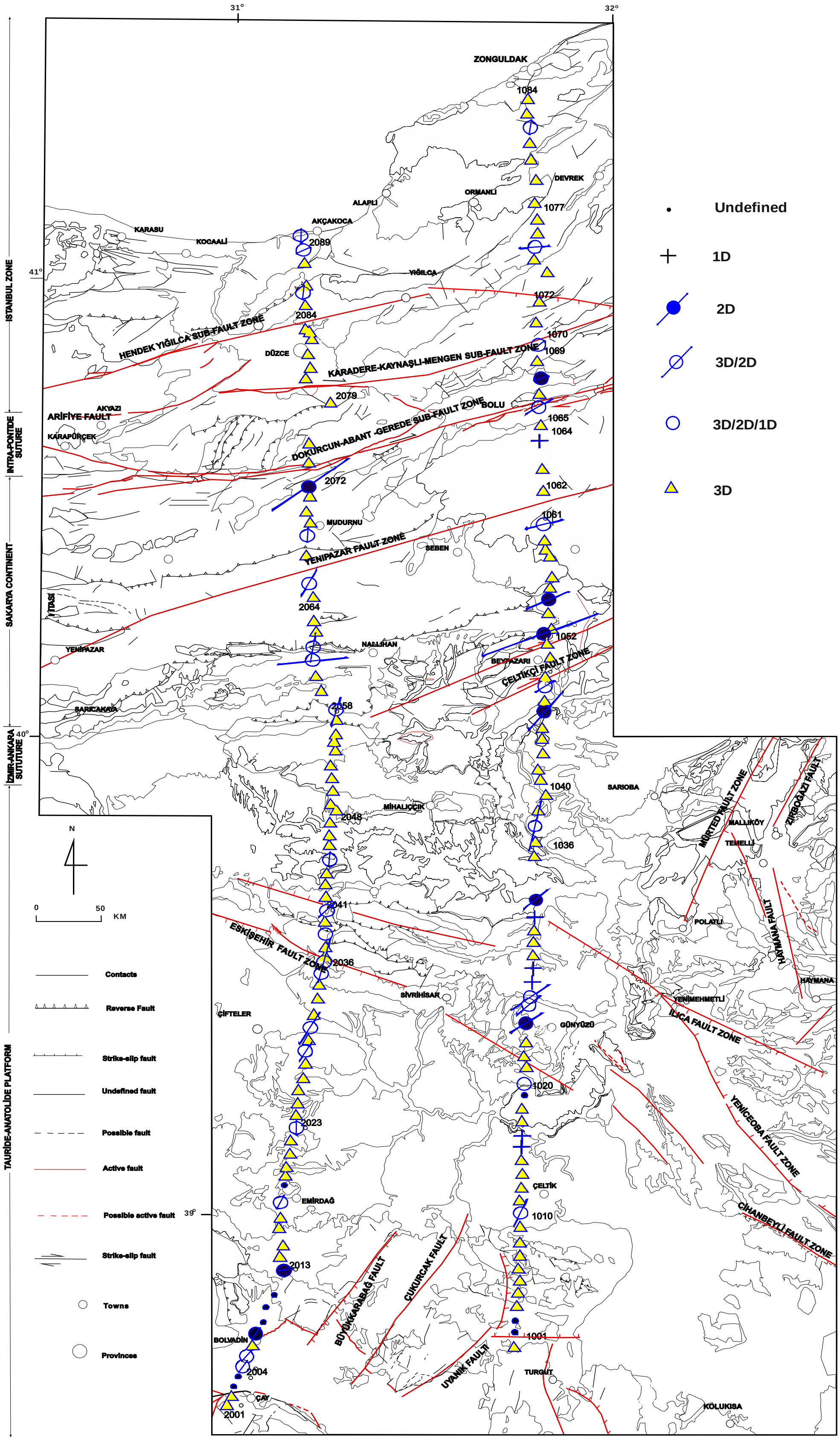

Fig. 12. Shows the KBA dimensionality analysis results on T=0.0s-0.01s band. Arrows show the strike direction. 3D/2D twist and 3D/2D are drawn as a single incident (3D/2D). Strike directions were scaled inversely proportional to error values. Certain signes are used for the existence of certain structures.

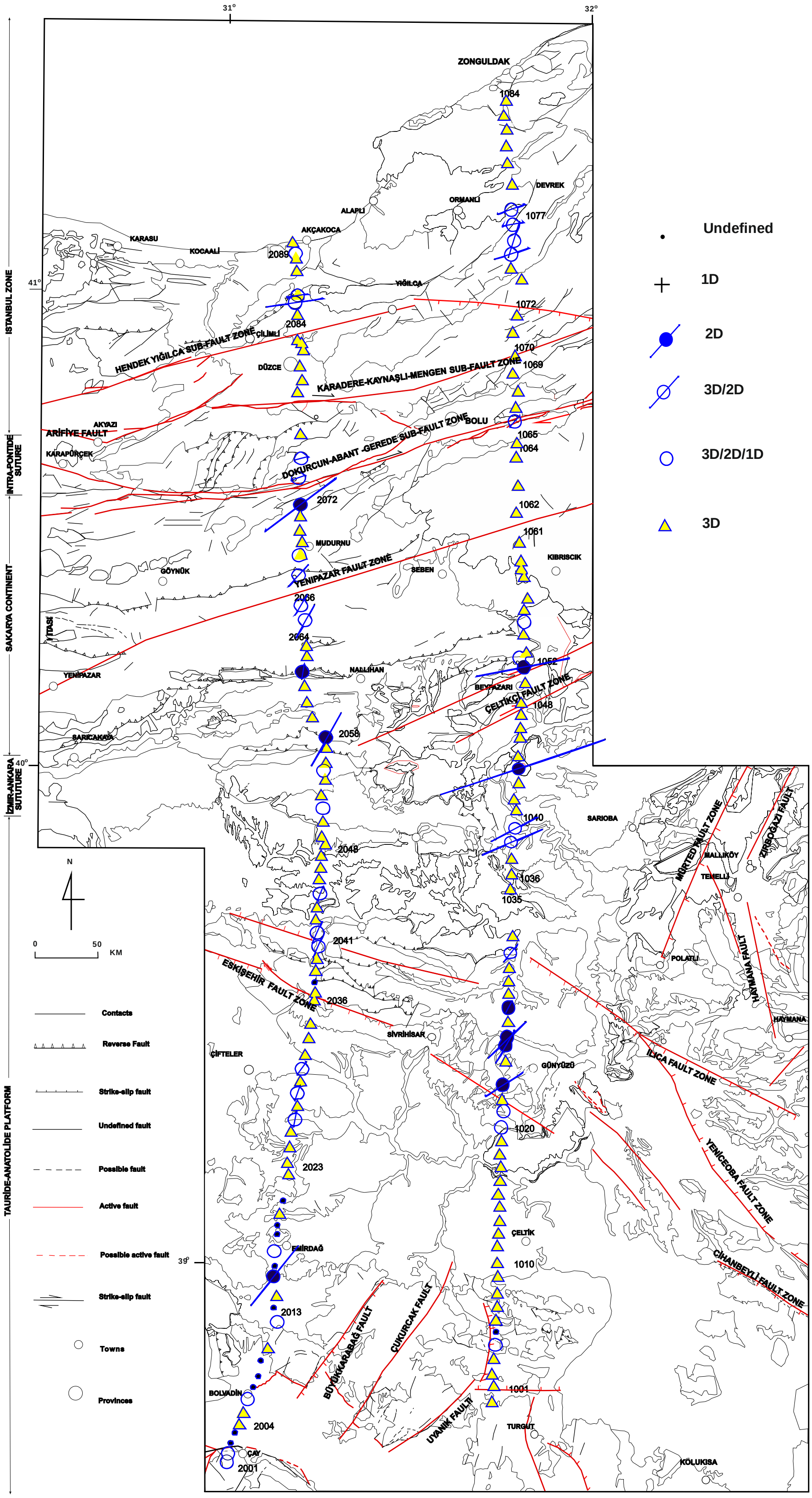

Fig. 13. Shows the KBA dimensionality analysis results on T=0.0s-0.01s band. Arrows show the strike direction. 3D/2D twist and 3D/2D are drawn as a single incident (3D/2D). Strike directions were scaled inversely proportional to error values. Certain signes are used for the existence of certain structures.

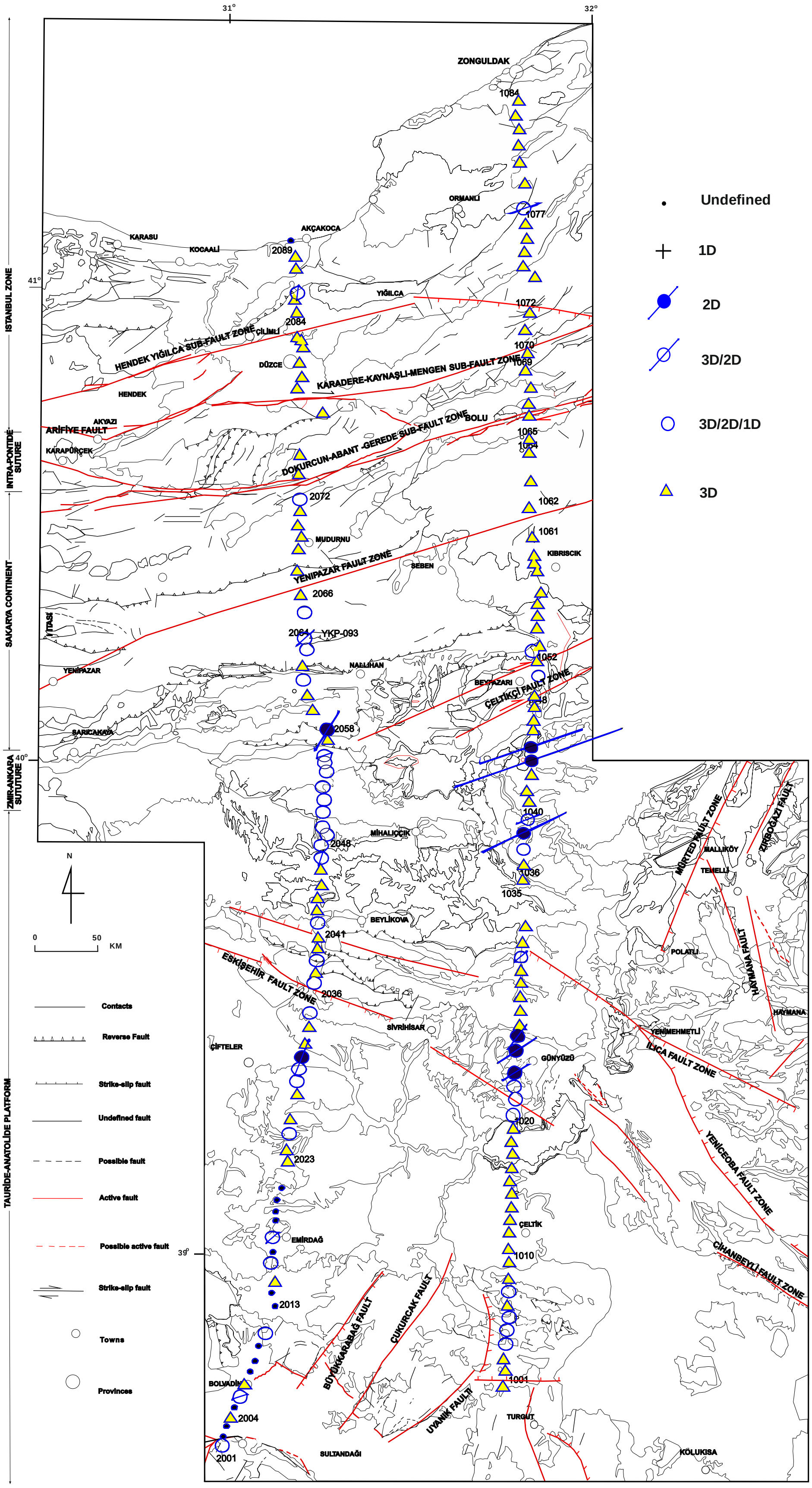

Fig. 14. Shows the KBA dimensionality analysis results on T=0.0s-0.01s band. Arrows show the strike direction. 3D/2D twist and 3D/2D are drawn as a single incident (3D/2D). Strike directions were scaled inversely proportional to error values. Certain signes are used for the existence of certain structures.

Fig. 12 shows the dimensionality analysis results obtained from WAL parameters on T=1-10s period band for measurement points 1001-1084 throughout the 1st Profile, from south to north. According to the figure, the most of the 1st Profile is 3D on the 4th band. Moving towards the north, some 2D structures with N60E strike angle and 3D/2D structures with N56E strike angle are also observed among these 3D structures.

Fig. 12 shows the dimensionality analysis results obtained from WAL parameters on T=1-10s period band for measurement points 2001-2090 throughout the 2nd Profile, from south to north. According to the figure, the most of the 2nd Profile is 3D on the 4th band.

Fig. 13 shows the dimensionality analysis results obtained from WAL parameters on T=10-100s period band throughout the 1st Profile, from south to north. According to this figure, there are 3D structures between points 1001-1023. The area between points 1023-1029 is represented by 2D structures with N46E strike angle and the area between points 1029-1075 is generally represented by 3-dimensionality and there are also a small number of 3D/2D structures with N66E strike. The dimensionality of points 1075-1078 is 3D/2D and the strike angle is N61E. The areas between points 1078-1084 located at the northernmost section of the 1st profile is 3D.

Fig. 13 shows the dimensionality analysis results obtained from WAL parameters on T=100-1000s period band for measurement points 2002-2090 throughout the 2nd profile, from south to north. According to this figure, the dimensionality at the first 21 points at the southernmost section of the 2nd profile is 3D and 3D/2D/1D. However, dimensionality could not be determined at most of the measurement points. While it is 3D between points 2021-2027, there are 3D structures and 3D/2D structures with N24E strike angle between points 2027-2031. The dimensionality between points 2031-2039 is 3D. Between points 2041-2046 there are 3D/2D and 3D structures with N24E strike angle. The dimensionality between points 2046-2065 is generally 3D. Among these 3D structures, there are also some 2D structures with N21E strike angle. The dimensionality at points 2065, 2066, 2067 is 3D/2D and the strike angle is N35E. The dimensionality between points 2068-2071 is 3D. The dimensionality at points 2072, 2074, 2075 is 3D/2D and 2D and the strike angle is N68E. The other points up to 2090 located at the northernmost section are mainly 3D.

Fig. 14 shows the dimensionality analysis results obtained from WAL parameters on T=100-1000s period band for measurement points 1001-1084 throughout the 1st profile, from south to north. According to this figure, there are 3D structures at the first 3 points of the 1st profile. Between points 1004-1009 there are some undistinguishable structures that could either be 3D/2D or 3D/1D. There are 3D structures between points 1009-1021. There are 2D structures with N51E strike and 3D/2D/1D structures between points 1021-1027. The structures located between points 1027-1039 are 3D. At points 1039, 1040 and 1044, 1045 there are 3D/2D structures with 70° strike angle and NE direction and 2D structures. The dimensionality of all other points up to 1084 at the northernmost section is 3D.

Fig. 14 shows the dimensionality analysis results obtained from WAL parameters on T=100-1000s period band for measurement points 2001-2090 throughout the 2nd profile, from south to north. According to this map, dimensionality could not be determined at some points in the south of the 2nd profile. It could only be determined at some points and usually there are some 2D structures and 3D structures observed with high error rates. The structures between points 2023-2048 are usually 3D and there are also 3D/2D/1D structures at some areas. The dimensionality between points 2048-2056 is 3D/2D/1D and between points 2056-2066 it ranges from 3D to 3D/2D/1D. At all other points to the north of 2066, mainly 3-dimensionality is observed.

7. DIMENSIONAL SECTIONS

WAL invariants for 80 periods were calculated based on the MT data from 174 stations throughout 2 profiles from the region between Zonguldak and Akşehir. Dimensionality states were obtained in accordance with WAL criteria on 80 periods for the 174 MT data and the data were contoured on Win G link program as vertical axis being the period and horizontal axis being the distance and dimensionality sections were obtained accordingly. Fig. 15 shows the changes in dimensionality throughout the 1st profile and the 2nd profile according to the period and the distance.

In Fig. 15, the dimensionality between 0.01-1s periods in the 1st profile is represented by 2D and 1D. 3D and 3D/2D dimensionality is mainly observed between periods 1-100s. The dimensionality between periods 100-10000s is 1D and 2D.

The dimensionality distribution in the 2nd profile is similar to that of the 1st profile. The dimensionality between periods 0.01-1s is represented by 2D and 1D. 3D and 3D/2D dimensionality is mainly observed between periods 1-100s. The dimensionality between periods 100-10000s is 1D and 2D.

Looking at the sections given below, it is possible to say that the sections in both profiles can be vertically divided into three sections. This could be interpreted as the upper crust, lower crust and upper mantle sorting, respectively, for the geoelectric section of the YKP profile suggested by Kaya (2010) (Fig. 16 a)).

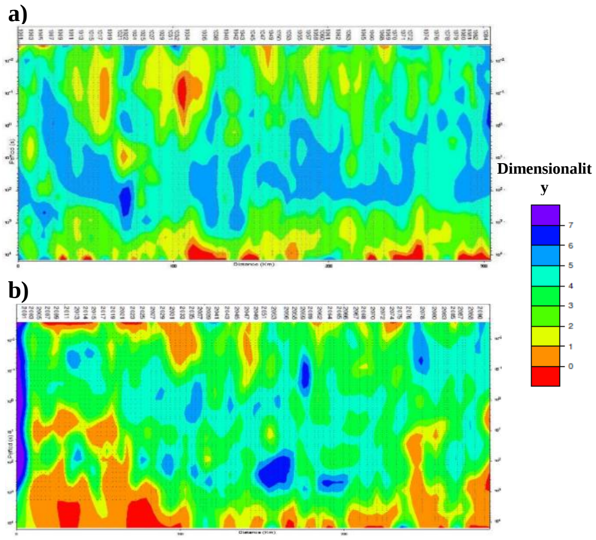

Fig. 15. Dimensional sections prepared according to WAL constants criteria a) Profile 1, b) Profile 2

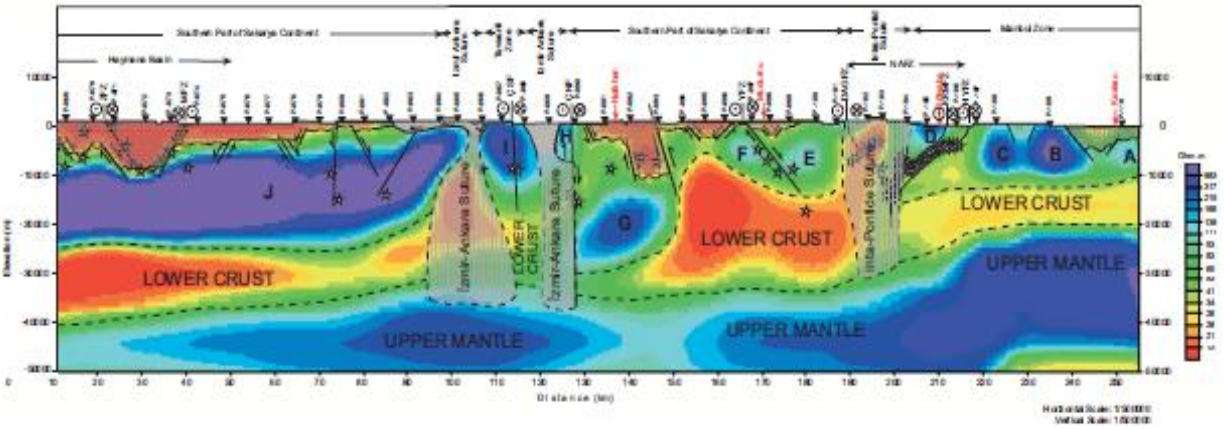

Fig. 16. a) The 2D resistivity model obtained as a result of inverting the MT data measured along a line close to the study area which obtained from the YKP points located in Fig. 1 (Kaya, 2010).

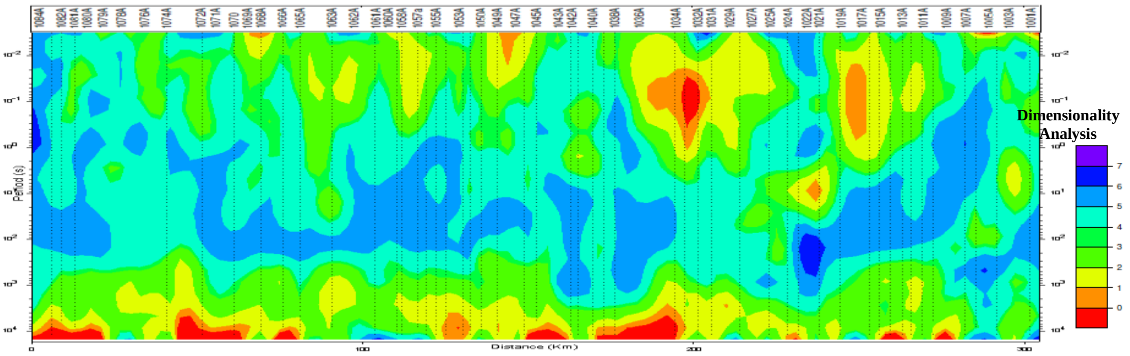

Fig. 16. b) Dimensional cross-section prepared according to WAL constants criteria along profile

8. CONCLUSIONS

As a result of the dimensionality analysis obtained from the KBA's MT data, 2D and 3D structures were revealed. The areas that were detected as 3D in 2D evaluation of the MT data should be interpreted more carefully.

The distinction between the upper crust and the lower crust can be observed more clearly when the dimensionality sections prepared in accordance with the WAL invariants criteria are analyzed (Fig. 16a and Fig. 16b).

According to the dimensionality maps;

- It was observed that the dimensionality was complex in short periods due to conductive heterogeneous materials close to the surface and 3D structures were more predominant in long periods.
- Moreover, it was observed that the dimensionality was more complex in areas near the suture zones according to the dimensionality analysis results.
- The strike directions of the structures near the North Anatolian Fault were generally N-NE.

These results show that dimensionality can be correlated to the geo-electric structure and geology. This should definitely be used in the evaluation of magnetotelluric measurement results.

ACKNOWLEDGEMENTS

This work, which includes a part of the graduate thesis (Kaçmaz, 2009) of Fahriye Akar, was supported by Cumhuriyet University Scientific Research Projects (CÜBAP, under grant no: M-350) and Scientific and Technological Research Council of Turkey (TUBITAK, under grant no: 105G145).

REFERENCES

Bahr, K., 1988, Interpretation of the magnetotellüric impedance tensor: regional induction and local tellüric distorsion. J.Geophys., 62, 119-127

Bahr, K., 1991. Geological noise in magnetotellüric data : a classification of distortion types, Phys. Earth planet. Inter., 66, 24-38.

Berdichevsky, M. N. and Dmitriev, V. I., 1976, Basic principles of interpretation of magnetotellüric sounding curves, In: Geoelectric and Geothermal studies, Ed.: Adam, A. Budapest, Akademai Kiado, 165-221.

Caldwell, T.G., Bibby, H.M., Brown, C., 2004. The Magnetotelluric Phase Tensor, Geophys. J. Int, 158,457-469.

Fischer, G. And Masero, W., 1994. Rotational properties of the magnetotelluric impedance tensor, the example of the Araguainha impact crater, Brazil, Geophys. J. Int., 119, 548-560.

Ingham, M.R., 1988. The use of invariant impedance in magnetotelluric interpretation, Geophys. J., 92, 165-169.

Kaçmaz, F. 2009. Magnetotelluric Investigation of Zonguldak-Aksehir Region Crustal Structure And Dimensionality Analysis, Graduate Thesis, 83 pp., Institute of Science, Cumhuriyet University, Turkey.

Kaya, C., 2010. Deep Crustal Structure of Northwestern Part of Turkey, Tectonophysics, 489, 227-239.

Lilley, F.E.M., 1976, Diagrams for magnetotelluric data: Geophysics, 41, 766–779.

Lilley, F.E.M., 1993a, Mohr circles in magnetotelluric interpretation (i) simple static shift; (ii) Bahr's analysis: Journal of Geomagnetism and Geoelectricity, 45, 833–839.

Lilley, F.E.M., 1993b, Three-dimensionality of the BC87 magnetotelluric data set studied using Mohr circles: Journal of Geomagnetism and Geoelectricity, 45, 1107–1113. Lilley, F.E.M., 1993c, Magnetotelluric analysis using Mohr circles: Geophysics, 58, 1498–1506.

Lilley, F.E.M., 1998a, Magnetotelluric tensor decomposition: Part I, Theory for a basic procedure: Geophysics, 63, 1885–1897.

Lilley, F.E.M., 1998b, Magnetotelluric tensor decomposition: Part II, Examples of a basic procedure: Geophysics, 63, 1898–1907.

Okay, A.I., 1989. Tectonic units and sutures in the Pontides, northern Turkey. In: A.M.C. Şengör, (Ed.), Tectonic evolution of the Tethyan region. Kluwer Academic Publications, Dordrecht: 109–115.

Okay, A.I. and Mostler, H., 1994. Carboniferous and Permian radiolarite blocks from the Karakaya Complex in northwest Turkey. Turk. J. Earth Sc., 3: 23-28.

Okay, A.I., Tüysüz, O., 1999. Tethyan sutures of northern Turkey. In "The Mediterranean Basins: Tertiary extension within the Alpine orogen" (eds. B. Durand, L. Jolivet, F. Horváth and M. Séranne), Geological Society, London, Special Publication 156, 475–515.[3]

Ranganayaki, R. P., 1984, An interpretativite analysis of magnetotelluric data:Geophysics, 49, 1730-1748.

Park, S. W. and Livelybrooks, D.W., 1989. Quantative interpretation of rotationally invariant parameters in magnetotellürics, Geophysics, 54, 1483-1490.

Romo, J. M., Gomez-Trevino, E. and Esparza, F. J., 1999. An invariant representation of the magnetic transfer function in magnetotellürics, Geophysics, 64, 1418-1428.
Smith, J. T., 1995. Understanding telluric distortion matrices, Geophys. J. Int., 122, 219-226.

Swift, C. M., 1967. A magnetotelluric investigation of an electrical conductivity anomaly in the southwestern United States, Ph.D. thesis, Massachusetts Institute of Technology, Cambridge, MA.

Szarka, L. and Menveille, M., 1997. Analysis of rotational invariantsof the magnetotellüric impedance tensor, Geophys. J. Int., 129, 133-142.

Turkish Journal of Engineering

Turkish Journal of Engineering (TUJE)
Vol.3, Issue 2, pp. 92-96, April 2019
ISSN 2587-1366, Turkey
DOI: 10.31127/tuje.429072
Research Article

THE BIOSYNTHESIS OF SILVER NANOPARTICLES BY CYTOPLASMIC FLUID OF CORIOLUS VERSICOLOR

Fatma Deniz *[1], Ali Osman Adigüzel [2] and Mehmet Ali Mazmanci [3]

[1] Mersin University, Engineering Faculty, Department of Environmental Engineering, Mersin, Turkey
ORCID ID 0000-0001-6782-8169
denizfatmaa@gmail.com

[2] OndokuzMayıs University, Faculty of Science and Letters, Department of Molecular Biology and Genetics, Samsun, Turkey
ORCID ID 0000-0002-5602-5886
adiguzel.ali.osman@gmail.com

[3] Mersin University, Engineering Faculty, Department of Environmental Engineering, Mersin, Turkey
ORCID ID 0000-0003-0219-530X
mazmanci@gmail.com

*Corresponding Author
Received: 31/05/2018 Accepted: 21/09/2018

ABSTRACT
The aim of this study is to investigate the production conditions of silver nanoparticles (NPs) in the presence of $AgNO_3$ with the fungal cytoplasmic fluid (FCF) of white rot fungus *Coriolus versicolor*. In this study, parameters such as pH, $AgNO_3$ concentration and FCF ratio of *C. versicolor* were optimized. *C. versicolor* was grown in SBM and then kept in ultrapure water to obtain FCF for synthesis of the nanoparticle. Nanoparticle formation was monitored by UV spectrophotometry at 420 nm wavelength and the silver nanoparticles were imaged by SEM. In the optimization study, it was found that at pH 5.0, 1.5 mM $AgNO_3$ and 50% FCF containing medium was found to provide optimal conditions for the synthesis of the silver nanoparticle. The nanoparticles were spherical and varied between 15-35 nm.

Keywords: *Nanoparticle, Silver, Coriolus Versicolor, Biosynthesis*

1. INTRODUCTION

Applications in which materials with dimensions less than 100 nm are used form the basis of nanotechnology (Gurmen & Ebin, 2008). Nanoparticles (NPs) have superior properties like high surface/volume ratio, character of surface atoms, quantum size effects, dimensional dependence of electronic structure when compared to materials in macro-size (Shukla *et al.*, 2012). Their superior properties enable them to be used in optical applications and in the production of many materials such as highly active catalysts, super conducting materials, surface-active materials (Gurmen & Ebin, 2008). Numerous advantages and wide application areas make nanoparticle synthesis one of the most interesting topics of the last few decades.

Nanoparticle synthesis is carried out by different chemical methods (such as chemical/photochemical reduction, electrochemical techniques) or by physical methods (Pantidos & Horsfall, 2014). However, these methods have disadvantages such as the use of toxic chemicals or high cost (Shanmugasundaram *et al.*, 2013). For this reason, alternative biological methods called "green nanotechnology/green synthesis" have been developed. Green synthesis applications are usually performed using microorganisms (such as algae, bacteria, fungi) or plant extracts. Especially microorganisms can be optimized for different conditions because they have high adaptability ability (Pantidos & Horsfall, 2014).

Compared with bacteria, fungi with micelles providing large surface area offer great advantages in the synthesis of metallic nanoparticles (Mukherjee *et al.*, 2001). This large area can be used to accelerate the interaction of metal ions with the fungal reducing material, and thus the conversion of ions to metallic nanoparticles can be increased (Pantidos & Horsfall, 2014).

Fungi can synthesize molecules in protein structure that can increase the rate of nanoparticle synthesis (Pantidos & Horsfall, 2014).

Silver, with good conductivity, chemical stability, catalytic, antibacterial and healing activity, is among the attracting metallic nanoparticles (Pantidos & Horsfall, 2014; Sharma *et al.*, 2009).

Investigations on the synthesis of silver nanoparticles (AgNPs) by biological methods show that microorganisms have great potential. Biomolecules such as amino acids, enzymes, proteins, polysaccharides, vitamins found in extracts reduce the amount of Ag+ ions in wastewater. Although it is a chemically complex reaction, it makes Ag+ ions harmless to the environment (Sharma *et al.*, 2009).

In this study, the synthesis of AgNPs was optimized by biosynthesis method**,** developed as an alternative to physical and chemical NP synthesis methods. Optimization parameters were determined as pH, $AgNO_3$ concentration and fungal cytoplasmic fluid ratio.

2. MATERIALS AND METHOD

2.1. Material

White rot fungus *C. versicolor* was obtained from the Microbiology Laboratory of the Department of Environmental Engineering, Mersin University. $AgNO_3$ and other chemicals have analytical purity.

2.2. Method

2.2.1. Preparation of Fungal Cytoplasmic Fluid (CV-FCF)

C. versicolor grown on SDA plates at 30°C was transferred to modified Stock Basal Medium (mSBM) with different pH values (5.0; 6.0) to obtain cytoplasmic fluid (Table 1) (Mazmanci *et al.*, 2002).

The fungus was then incubated at 30 °C, in the dark, at 160 rpm for 10 days. At the end of the incubation, the pellets were rinsed with sterile ultrapure water to remove the metabolite formed during the incubation. Subsequently, the pellets were re-suspended in sterile ultrapure water-containing tubes (1:1 v/v) and incubated for 5 days at 30 °C in the dark, at 160 rpm to obtain fungal cytoplasmic fluid (CV-FCF). After the incubation, the pellets were removed from the medium by centrifugation and the CV-FCF was stored at +4 °C for study.

Table 1. Modified Stock Basal Medium (mSBM)

Material	g/L
KH_2PO_4	13.60
K_2HPO_4	17.41
$CaCl_2.2H_2O$	0.05
$MgSO_4.7H_2O$	0.05
$NH_4(H_2PO_4)$	1.00
Glucose	10.00
pH	5.0; 6.0

2.2.2. Optimization Studies in AgNPs Biosynthesis

$AgNO_3$ solution was added to CV-FCF obtained from pellets grown at different pH values (5.0; 6.0) as final concentration on 1.00 mM. CV-FCF-free $AgNO_3$ solution and $AgNO_3$-free CV-FCF medium were used as control groups for pH optimization.

Optimization of the $AgNO_3$ concentration was performed in medium containing 0.50, 0.75, 1.00, 1.50 mM $AgNO_3$. CV-FCF medium without $AgNO_3$ and medium without CV-FCF for each $AgNO_3$ concentration were used as control groups.

Optimization of CV-FCF ratio was performed using media containing 25%, 50%, 75% and 100% CV-FCF. $AgNO_3$-free media containing 25, 50, 75 and 100% CV-FCF and $AgNO_3$ solution without CV-FCF were used as control groups.

Optimization studies were carried out at 30 °C, in dark conditions and at 160 rpm. The formation of AgNPs was observed with an increase in the medium color at 420 nm in the UV spectrophotometer at two-day intervals for 20 days.

Characterization of AgNPs in precipitates obtained from centrifugation was performed by scanning electron microscopy (SEM) after washing with ultrapure water and drying.

3. RESULTS

For the growth of the *C. versicolor*, optimum pH range has been reported to be 5.0-5.8 (Jo *et al.*, 2010). FCF obtained from *C. versicolor* cultivated in pH 5.0 and 6.0 conditions were studied to show the effect of medium pH. It was observed that the fungus pellets grown in pH 5.0 were larger than those grown in pH 6.0 (data not shown).

The effects of CV-FCF obtained from the fungus pellets grown at pH 5.0 and 6.0 were shown in Fig. 1a. It was observed that CV-FCF at pH 5.0 produced higher concentrations of AgNP and reached the highest absorbance value at day 18 (Fig. 1b).

Results of $AgNO_3$ concentration optimization were presented in Figs. 2a and b. The highest absorbance value was reached on day 16 in medium containing 1.50 mM $AgNO_3$.

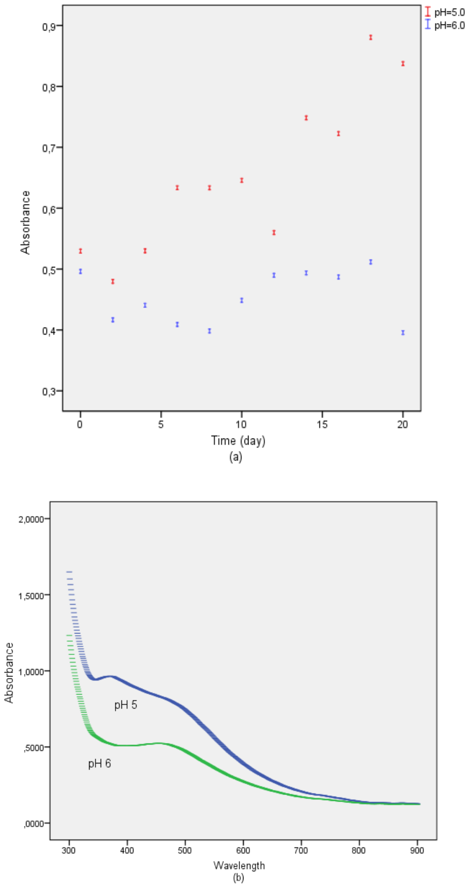

Fig. 1. Effect of pH on AgNPs biosynthesis. (a) Change in time-dependent absorbance value, (b) Spectra of the day reaching the highest absorbance value

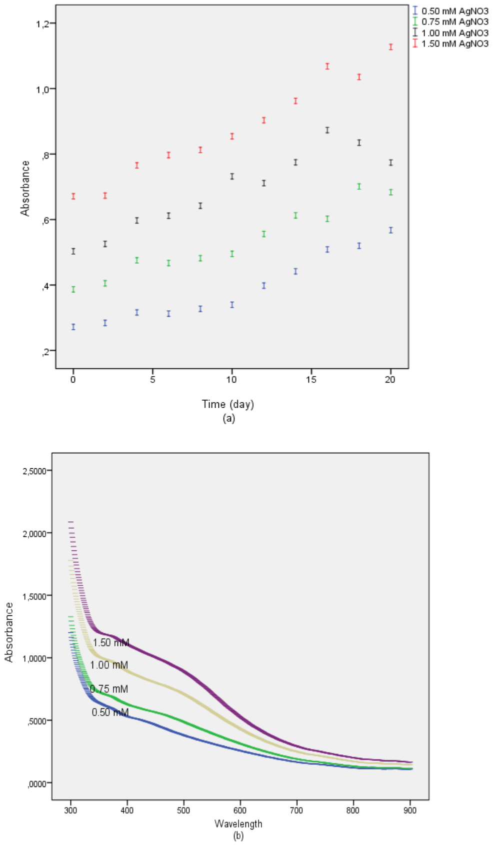

Fig. 2. Effect of $AgNO_3$ concentration on AgNP biosynthesis. (a) Change in time-dependent absorbance value, (b) Spectra of the day reaching the highest absorbance value.

The CV-FCF ratio optimization studies demonstrated that the highest absorbance value was reached on day 14 for 100% CV-FCF containing medium. (Fig. 3a and b).

In the SEM analysis, the AgNPs obtained from the solution with the highest absorbance value (the pH 5.0, 1,50 mM $AgNO_3$, 100% CV-CFC) were used. Results have shown that they were spherical and their size varied between 15-35 nm (Fig. 4).

4. DISCUSSION

Microorganisms, like every living thing, have various defense mechanisms to maintain their lives. Most metal ions are toxic to bacteria, therefore, converting toxic metal ions into water-insoluble form is a defense mechanism developed by bacteria (Sastry *et al.*, 2003; Prathna *et al.*, 2010). They carry out this transformation either inside or outside the cell with the biomolecules they produce. Many studies have been conducted with fungi in this regard and it has been shown that fungi, which are exposed to toxic conditions, may exhibit similar behaviors by producing extracellular or intracellular metabolites (Khan *et al.*, 2018).

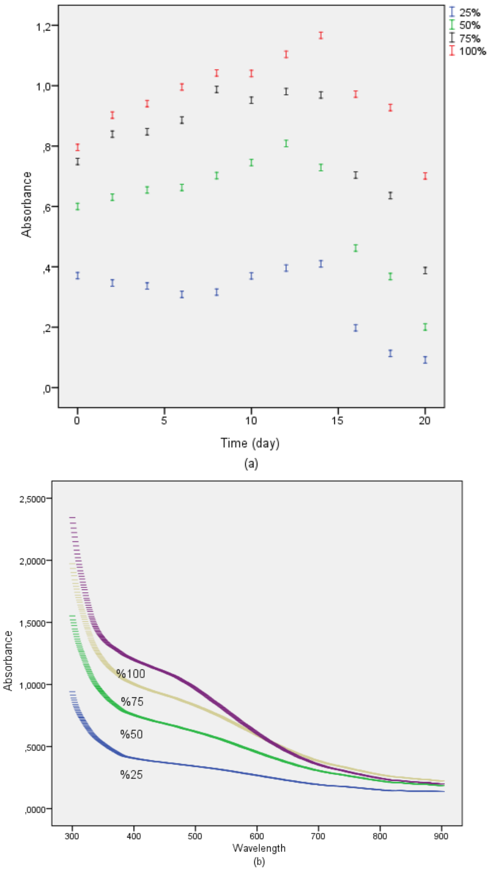

Fig. 3. Effect of CV-FCF dilution ratio on AgNP biosynthesis. (a) Change in time-dependent absorbance value, (b) Spectra of the day reaching the highest absorbance value.

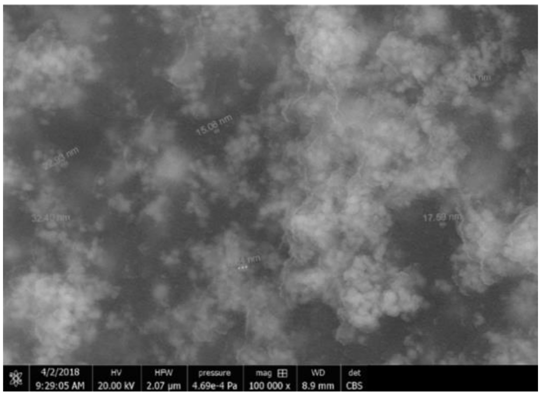

Fig. 4. Scanning electron micrograph of silver nanoparticles synthesized by CV-FCF.

Silver NPs exhibit remarkable colors (yellow to brown) due to the excitation of surface plasma vibrations in the particles, and their formation can be qualitatively determined (Sastry *et al.*, 2003). During the study, same color changes were observed when $AgNO_3$ solution was added to CV-FCF. This result indicated that Ag+ ions are reduced very quickly. According to the results, it can be predicted that the fungus may convert silver toxicity to a non-toxic metallic form despite the use of fungal cytoplasmic fluid (Sastry *et al.*, 2003; Ahmad *et al.*, 2003; Khan *et al.*, 2018).

Gudikandula *et al.* synthesized the AgNPs using the media of white rot fungus grown at pH 6.0 (Gudikandula *et al.*, 2017). In this study, FSF obtained from fungus grown at pH 5.0 and 6.0 was used. CV-FCF obtained from *C. versicolor* grown at pH 5.0 was found to be more efficient in AgNPs synthesis. This suggests that pH is an important parameter. Similarly, Kathiresan *et al.* optimized the pH value (5.0-9.0) of the cytoplasmic fluid obtained from *Penicillium fulvutanum*. They obtained the best optical density at pH 6.0 (Kathiresan *et al.*, 2009). This indicates that the pH value of both fungi growth environment and FCF have a significant effect on AgNPs synthesis.

The final concentration of $AgNO_3$ was used as 1.00 mM for nanoparticle synthesis in the previous studies (Vigneshwaran *et al.*, 2006; Zonooz&Salouti, 2011; Abdelrahim *et al.*, 2017). In this study, $AgNO_3$ concentration varied between 0.50 - 1.50 mM. AgNP formation increased with increasing $AgNO_3$ concentration and the highest absorbance value was reached at 1.50 mM. Kathiresan *et al.* (2009) and Gudikandula *et al.* (2017) reported the similar results. Adıgüzel *et al.* synthesized AgNPs with bacterial cytoplasmic fluid (BCF) obtained from newly isolated Streptomyces genus. They studied $AgNO_3$ concentrations ranged from 0.50 to 1.50 mM and reported the highest absorbance value at 1.00 mM $AgNO_3$ concentration (Adiguzel *et al.*, 2018).

In the optimization of the CV-FCF ratio, the absorbance values reached on day 12 were 0.390, 0.809, 0.980 and 1.103 for the 25, 50, 75 and 100% CV-FCF, respectively. Formation of AgNP was increased with increasing CV-FCF ratio in media. This suggests that the amount of AgNP synthesized depends on the amount of metabolite. When the results were compared as proportionally, it was seen that the amount of nanoparticle produced in the medium that contains 50% CV-FCF was higher than the others. Although the highest absorbance value was reached (day 14; 1,160 abs) in the medium containing 100% CV-FCF, 50% CV-FCF was found to be more efficient in AgNP biosynthesis (day 12; 0,809 ABS). Therefore, the optimum value was accepted as 50%.

As a result of SEM analysis, it was observed that the synthesized NPs were in spherical shape and in dimensions ranging from 15-35 nm. Previous studies supported these findings (Kathiresan *et al.*, 2009; Syed *et al.*, 2013; Das *et al.*, 2012).

Ahmad *et al.* reported that AgNP synthesis takes place outside the cell because biomass remains in its original color after the reaction (Ahmad *et al.*, 2003). However, Sastry *et al.* determined that AgNP synthesis takes place in the cell because of the color change in the biomass (Sastry *et al.*, 2003). Bacteria or fungi can synthesize silver nanoparticles both in- and outside the cell. Results obtained in this study demonstrate that fungal biomass is not needed for AgNP synthesis and this process can be performed with metabolites. On the other hand, the reaction catalyzed by CV-FCF does not provide evidence of which of the intracellular metabolites are involved in nanoparticle synthesis.

5. CONCLUSION

Fungal cytoplasmic fluid of *Coriolus versicolor* obtained from different conditions (pH 5.0 and 6.0, 0.50-1.50 mM $AgNO_3$ concentration, 25-100% CV-FCF) was investigated for silver nanoparticle biosynthesis. Maximum AgNPs production was carried out in media obtained from *C. versicolor* grown at pH 5, containing 1.50 mM $AgNO_3$ and 100% CV-FCF. But, it has been found that 50% CV-FCF is more effective in AgNPs biosynthesis. SEM analysis of AgNPs showed they were spherical and their dimensions varied between 15-35 nm.

ACKNOWLEDGEMENTS

This paper has been presented orally at the 1st International Symposium on Innovative Approaches in Scientific Studies in Antalya.

REFERENCES

AbdelRahim, K., Mahmoud, S. Y. and Ali, A. M., Almaary, K. S., Mustafa, M. A. and Husseiny, S. M. (2017). “Extracellular biosynthesis of silver nanoparticles using *Rhizopus stolonifera*.” *Saudi Journal of Biological Sciences*, 24, pp. 208-216.

Adigüzel, A. O., Adigüzel, S. K., Mazmanci, B., Tunçer, M., Mazmanci, M A. (2018). “Silver Nanoparticle Biosynthesis from Newly Isolated Streptomyces Genus From Soil.” *Materials Research Express,* 5, pp. 1-12 DOI: 10.1088/2053-1591/aab861.

Ahmad, A., Mukherjee, P., Senapati, S., Mandal, D., Khan, M. I., Kumar, R. and Sastry, M. (2003). “Extracellular biosynthesis of silver nanoparticles using the fungus *Fusarium oxysporum*.” *Colloids and Surfaces B: Biointerfaces*, 28, pp. 313-318.

Das, S. K., Khan, Md. M. R., Guha, A. K., Das, A. R. and Mandal, A. B. (2012). “Silver-nanobiohybride material: Synthesis, characterization and application in water purification.” *Bioresource Technology,* 124, pp. 495-499.

Gudikandula, K., Vadapally, P. and Charya, M. A. S. (2017). “Biogenic synthesis of silver nanoparticles from white rot fungi: Their characterization and antibacterial studies.” *OpenNano* 2, pp. 64-78.

Gurmen, S., Ebin, B. (2008) “Nanopartiküller ve Üretim Yöntemleri – 1.” *TMMOB Metalurji Mühendisleri Odası, Metalurji Dergisi*, 150, pp. 31-38.

Jo, W. S., Kang, M. J., Choi, S. Y., Yoo, Y. B., Seok, S. J. and Jung, H. Y. (2010). “Culture Conditions for Mycelial Growth of *Coriolus versicolor*.” *Mycobiology,* 38, pp. 195-202.

Kathiresan, K., Manivannan, S., Nabeel, M.A. and Dhivya, B. (2009). “Studies on silver nanoparticles synthesized by a marine fungus, *Penicillium fellutanum* isolated from coastal mangrove sediment.” *Colloids and Surfaces B: Biointerfaces,* 71, pp. 133-137.

Khan, A. U., Malik, N., Khan, M., Cho, M. H., Khan, M. M. (2018). “Fungi-assisted silver nanoparticle synthesis and their applications.” *Bioprocess Biosyst Eng,* 41, pp. 1-20.

Mazmanci, M. A., Unyayar, A. and Ekiz, H. I. (2002). “Decolorization of methylene blue by white rot fungus *Coriolus versicolor*.”*Fresenius Environmental Bulletin*, 11, pp. 254 - 258.

Mukherjee, P., Ahmad, A., Mandal, D., Senapati, S., Sainkar, S. R., Khan, M. I., Parishcha, R., Ajaykumar, P. V., Alam, M., Kumar, R., Sastry, M. (2001). “Fungus-Mediated Synthesis of Silver Nanoparticles and Their Immobilization in the Mycelial Matrix: A Novel Biological Approach to Nanoparticle Synthesis.” *Nano Letters,* 1, pp. 515-519.

Pantidos, N. and Horsfall, L. E. (2014). “Biological Synthesis of Metallic Nanoparticles by Bacteria, Fungi and Plants.” *Nanomedicine & Nanotechnology*, 5, pp. 1-10.

Prathna, T.C., Mathew, L., Chandrasekaran, N., Raichur, A. M. and Mukherjee, A. (2010). “Biomimetic Synthesis of Nanoparticles: Science, Technology & Applicability.” *Nature*, DOI:10.5772/8776.

Sastry, M., Ahmad, A., Khan M. I. and Kumar, R. (2003). “Biosynthesis of metal nanoparticles using fungi and actinomycete.” *Current Science*, 85, pp. 162-170.

Shanmugasundaram, T., Radhakrishnan, M., Gopikrishnan, V., Pazhanimurugan, R., Balagurunathan, R. (2013). “A study of the bactericidal, anti-biofouling, cytotoxic and antioxidant properties of actinobacterially synthesized silver nanoparticles.” *Colloids and Surfaces B: Biointerfaces,* 111, pp. 680-687.

Sharma, V. K., Yngard, R. A. and Lin, Y. (2009). “Silver nanoparticles: Green synthesis and their antimicrobial activities.” *Advances in Colloid and Interface Science*, 145, pp. 83-96.

Shukla, V. K., Yadav, R. S., Yadav, P. and Pandey, A. C. (2012). “Green synthesis of nanosilver as a sensor for detection of hydrogen peroxide in water.” *Journal of Hazardous Materials*, 213– 214, pp. 161-166.

Syed, A., Saraswati, S., Kundu, G. C. and Ahmad, A., (2013). “Biological synthesis of silver nanoparticles using the fungus Humicola sp. and evaluation of their cytoxicity using normal and cancer cell lines.” *Spectrochimica Acta Part A: Molecular and Biomolecular Spectroscopy,* 114, pp. 144-147.

Vigneshwaran, N., Kathe, A. A., Varadarajan, P.V., Nachane, R. P. and Balasubramanya, R. H. (2006). “Biomimetics of silver nanoparticles by white rot fungus, *Phaenerochaete chrysosporium*.” *Colloids and Surfaces B: Biointerfaces,* 53, pp. 55-59.

Zonooz, N. F. and Salouti, M.(2011). “Extracellular biosynthesis of silver nanoparticles using cell filtrate of Streptomyces sp. ERI-3.” *Scientia Iranica F* 18, pp. 1631-1635.

Turkish Journal of Engineering

Turkish Journal of Engineering (TUJE)
Vol. 3, Issue 2, pp. 97-101, April 2019
ISSN 2587-1366, Turkey
DOI: 10.31127/tuje.451173
Research Article

STUDY THE EFFECT OF HAIR STYLE PRODUCTS ON THE QUALITY OF DOMESTIC WASTEWATER- WAX AS CASE STUDY

Muhammed Saleh *[1], Mutlu Yalvaç [2], Ferhat Sime [3] and Mehmet Ali Mazmanci [4]

[1] Mersin University, Ph.D. student, Environmental Engineering Department, Mersin University. Mersin, Turkey
ORCID ID 0000-0002-3145-4457
E-mail: Muh.saleh89@gmail.com

[2] Mersin University, Ph.D., Environmental Engineering Department, Mersin University. Mersin, Turkey
ORCID ID 0000-0002-1281-5712
E-mail: myalvac@mersin.edu.tr

[3] Mersin University MSc. Student, Environmental Engineering Department, Mersin University. Mersin, Turkey
ORCID ID 0000-0002-4925-5982
E-mail: ferhatsime04@gmail.com

[4] Mersin University, Professor, Environmental Engineering Department, Mersin University. Mersin, Turkey
ORCID ID 0000-0003-0219-530X
E-mail: mazmanci@gmail.com

---

* Corresponding Author
Received: 06/08/2018 Accepted: 25/09/2018

ABSTRACT

People have used personal care products throughout history. Hair cosmetics are among the most common and widely used products. In this study, the effect of WAX and shampoo, which are hair cosmetics, on domestic wastewater pollution were investigated separately and together. The study consists of two stages. In the first stage, Chemical Oxygen Demand (COD) and hydrogen concentration (pH) of WAX, shampoo and WAX + shampoo were analyzed. COD results were 1096 mg / L, 584 mg / L and 1896 mg / L, respectively. In the second stage, these products (0.1 g WAX and 0.1 g shampoo) were added separately and jointly to 2g of human raw hair. In this stage, wastewater was prepared by shaking sample of hair in 100 mL water for 30 minutes. The concentrations of COD were 1296 mg / L, 592 mg / L and 1328 mg / L, respectively. The PH increased from 7.3 to about 8 after adding cosmetics. The experiments showed that the added WAX to the hair is reduced by 40% by weight in 25 ^{0}C and 30 minutes. In order to quantify and realize the human habits of using such hair cosmetics during the day, a questionnaire was prepared and distributed to 385 of people. It was found that 43% of the people used WAX and 45% of them used this product every day. Accordingly, this study have been investigated only WAX and shampoo, keeping in mind that chemicals used for cosmetic purposes have been found enormous effects on domestic wastewater.

Keywords: *Domestic Wastewater; Hair-style Products; Shampoo; Human Hair.*

1. INTRODUCTION

Wastewater can be defined as any used liquid discharged into the environment and can harm it. It can be divided by mass to water which forms (99.9%). The residue part (0.1%) can be normal and industrial compounds which can be called as contaminants (Templeton & Butler, 2011).

Hair is very important to the human, it covers the human skin. Also, it protects the human body from the environmental factors and the injuries (Bouillon & Wilkinson, 2005). Follicles producing keratinized cells which form the hair shaft (Robbins, 2012). Hair elasticity caused by the presence of keratin (Marsh, et al., 2015). The hair shapes differ from individual to another but in general, it has a shape of an elongated cylinder. The hair diameter can vary between 45-110μm (Yin, et al., 1977).

In order to preserve hair shape, chemical products such as (WAX, Spray ….etc.) were used by the human. When applying and drying these materials it causes a film on the hair surface which causes a stable shape (Bouillon & Wilkinson, 2005). Many factors affecting this process such as human habits, environmental conditions, etc. but the main factor is the time needed to conserve the shape of hair (hairstyle) (Bouillon & Wilkinson, 2005).

According to Schueller and Romanowski (2000), the main agent of hair styling product is the polymer (Schueller & Romanowski, 2000). The polymers can be one of these major categories: Non- ionic Polymers, Anionic Polymers, Cation Polymers, and Amphoteric Polymers (Frosch, et al., 1994).

WAX as one of the popular conditioner products which helps in maintaining the shape of the hair. It has an anhydrous base which can be formed from fat or emulsions. In both cases, WAX behaves as thickeners and hardeners because of the effect of fatty phases (Bouillon & Wilkinson, 2005). The problem is in removing the fats from hair, in order to deal with that, there are many products were used. The shampoo is a preferred product for human hair washing. The effect of these components (WAX and shampoo) on the domestic wastewater should be studied.

This paper aims to find the effect of using hairstyle products (especially WAX) on the quality of the domestic wastewater. Also, the effect of the shampoo on domestic wastewater was taken into the scope of this study.

2. MATERIAL AND METHOD

2.1. Material

In this study the effect of hair cosmetics (WAX and Shampoo) on the domestic wastewater was assessed. The main materials (WAX, shampoo and raw- clean human hair) were used in this research. WAX is the product used for men hair style while the shampoos are the preferred product for human hair washing. The above three component were collected from barber salon. Raw-clean hair (RC-Hair) was collected from people who have never used cosmetics, bleach or dies before, while WAX and shampoo were randomly selected with no brand discrimination was made.

2.2. Method

To study the effect of hair cosmetics on domestic wastewater, the following procedure had been followed:

2.2.1. People habits of using WAX and shampoo exploration

To explore people habits of using WAX and shampoo in Yenişehir –Mersin, field surveys were conducted to collect required information from barber salon and community. In order to facilitate this mission two simple and definite questionnaires were prepared for barber saloon and the community.

In this research, 95% confidence level and 5 confidence interval were achieved by distributing 385 questioners to the community Eq.(1). The collected data were used for analyzing and estimating the percent of WAX users in the sample area.

$$SS = \frac{Z^2 \times P \times (1-P)}{C^2} \qquad (1)$$

Whereas: SS: sample size, Z: Z-Value, P: Percentage of population picking a choice, C: Confidence interval.

2.2.2. Sample Preparation

Four samples were prepared as control groups (only WAX, only shampoo, only hair, shampoo, and WAX). Other three samples were prepared in the presence of human hair (Table 1). The hair samples were washed with distilled water and then dried for 24 h at the room temperature. All the work had been done in a tap water medium to simulate the real situation.

Table 1: Experimental design

No.	Experiment	Constituents (g/ 100 mL water)	Method of application (shaken for 30 min at 150 rpm)
1	WAX	0.1	WAX was dissolved in water.
2	Shampoo	0.1	Shampoo was dissolved in water.
3	WAX	0.1	A mix of shampoo and WAX were dissolved in water.
	Shampoo	0.1	
4	Raw-Clean Hair	2.0	Human hair was washed in water.
5	Shampoo	0.1	Human hair was washed with shampoo and water.
	Raw-Clean Hair	2.0	

6	WAX	0.1	Human hair was treated with WAX, waited to dry for 30min in room temperature, and then washed in water.
	Raw-Clean Hair	2.0	
7	WAX	0.1	Clean human hair was treated with WAX, waited to dry for 30 min in room temperature, and then treated with shampoo and then washed in water.
	Shampoo	0.1	
	Raw-Clean Hair	2.0	

2.2.3. Analysis

Closed Reflux, Titrimetric Method (5220 C) was used in order to find Chemical Oxygen Demand (COD) (AWWA, WEF, APHA, 1998). pH was measured before and after shaking. The volatile value of WAX (vvWAX) was calculated Eq. (2).

$$vvWAX = [aWAX] - [rWAX] \qquad (2)$$

Whereas:

[vvWAX]: Volatile value of WAX;

[aWAX]: Amount of WAX applied to the hair;

[rWAX]: Amount of remaining WAX after 30 min.

3. RESULT AND DISCUSSION

3.1. Questionnaire's results

The used WAX in Yenişehir –Mersin data was collected from questionnaires (community and barber). For the community questioners, it showed that 61% of the sample were washing their hair every day which is 1.6 higher than the percentage obtained by (Ficheux, et.al, 2016) for French people for the same washing time. While 30% were cleaning it one time every two days, 8% one time every three days and just 1% are washing it one time every week (Figure 1).

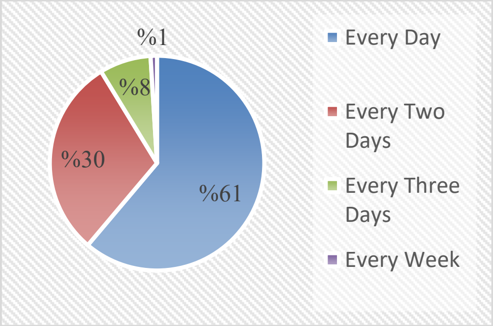

Fig. 1. Shows the hair washing rate.

The hairstyle users' percentage was 43% while the nonuser’s percentage was 57% (Figure 2).

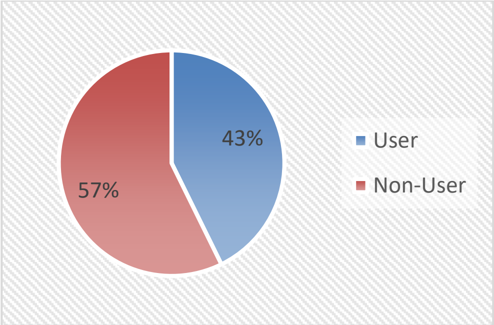

Fig. 2. Shows the hair style products user percentage.

It also showed that 45% of hairstyle users were using it every day, while 27%, 21%, 7% are using it every two days, three days, every week respectively (Figure 3).

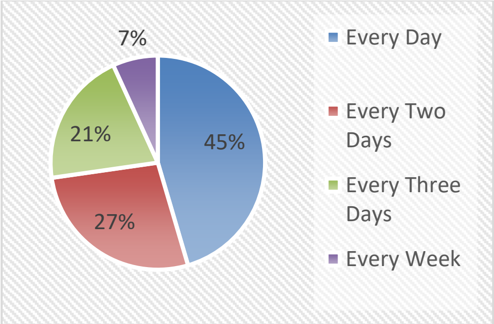

Fig. 3. Shows hair style product using rates.

The questioners showed that 80% of the community is using shampoo as washing material while as 13% using soap and 7% using both (Figure 4). In Turkey, there is no record for quantifying of WAX or such cosmetics, but according to U.S EPA annual report (2002) cosmetics annuals imports and productions increased by ten times for the last twenty-five years (U.S. Environmental Protection Agency (U.S. EPA), 2002). In China, there are more than 20000 kinds of cosmetics, the exportation reached 437000 tons, and the importation amount was 74000 tons (Editorial Department of D&C, 2015).

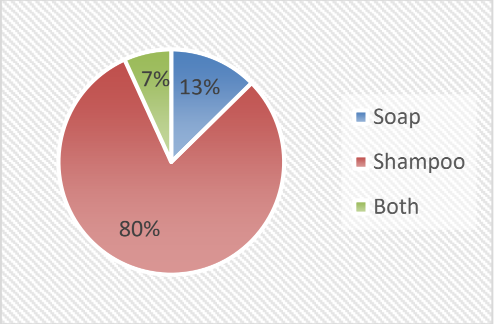

Fig. 4. Shows hair washing material.

3.2. COD and pH results

The samples were tested in terms of pH and COD as described in material and method section. The pH for all samples after shaking process varies from 8.0 to 8.3. These values are close to the result of other researches. Ma and Chen (2018) have studied the characteristics of cosmetic wastewater. They found that the pH values range from 8.6-8.7 (Ma & Chen, 2018).

Minimum pH and COD values were noted in the combination human hair with water tab and they were 8.0 and 504 mg/L respectively. While the maximum pH and COD values were noted in the combination (human hair, WAX, and Shampoo) where they were 8.3 and 1896 mg/L respectively. It was noticed that approx. 40% of WAX was volatile, even though that presence of small amount of WAX caused a relatively high COD value. The cosmetic wastewater may cause a high level of COD. It can be larger than 100000 mg/l (Jan Bogacki et.al, 2011). Ma and Chen (2018) have found the COD value concerning a certain product. It was 5490 mg/l (Ma & Chen, 2018).

The pH results of the combinations consisting of Shampoo reflect the formulation conditions of shampoos, which are near neutrality (Robbins, 2012). COD results for the same group can be explained by the sorption capability of hair, which depends on the relationship between the interaction with keratin (binding or attraction) versus hydrophilicity (Robbins, 2012).

This paper suggests that a significant amount of shampoo have remained at the tested hair, and the hair should be rewashed to extract the total amount of shampoo. Unfortunately, this amount had not been determined in this paper.

It is noticed that whenever shampoo was mixed with WAX, the COD values become higher than using WAX alone. The possible explanation implies that the shampoo might expedite dissolving WAX in the water and causing relatively high COD values. These results reflect the capability of anionic surfactant shampoos in aiding removal of fats and WAX'es (Bouillon & Wilkinson, 2005).

The test results of the other combinations can be shown in Table 2.

Table 2: Combinations Results

NO.	Combination	Hair (g)	Water (mL)	Wax (g)	Shampoo (g)	pH	COD (mg/L)
Ref	Tap Water		100			7.3	25.0
1	Wax		100.0	0.1		8.1	1096. 0
2	Shampoo		100.0		0.1	8.2	584.0
3	Wax + Shampoo		100.0	0.1	0.1	8.3	1896.0
4	RC Hair	2.0	100.0			8.0	504.0
5	Shampoo + RC Hair	2.0	100.0		0.1	8.1	592.0
6	Wax + RC Hair	2.0	100.0	0.1 *		8.1	1296.0
7	WAX +Shampoo + RC Hair	2.0	100.0	0.1*	0.1	8.1	1328.0
* This is the weight of WAX before volatilization average and after the volatilization is 0.0608g.							

4. CONCLUSION

The effects of the hair care product WAX and shampoo were examined on the domestic wastewater in this paper. It had been found that 40% of WAX volatilized in 30 minutes after applying to the hair, at room temperature, even though the residue part caused an increscent of COD to 1328 mg/L. Shampoo could increase the COD to 584 mg/L when applying it directly to the water. When applying it to the hair shampoo should be washed more than one time to have the exact amount of COD.

It has been assumed that no WAX residue on the hair. In future researches, this assumption should be verified and the other parameters like turbidity, toxicity, total solids, etc. could be controlled. The experiments were accomplished in normal water temperature (18℃) the effect of water temperature on the solubility of WAX’s water should be examined.

REFERENCES

AWWA, WEF, APHA (1998). *Standard Methods for the Examination of Water and Wastewater Closed Reflux, Titrimetric Method (5220 C)* page 5-16/17.

Bouillon, C. and Wilkinson, J. (2005). *The science of hair care.* Second edition. Taylor & Francis Group, LLC. ISBN 9780824759698.

Editorial Department of D & C (2015) "Analysis of Chinese Cosmetics" *Industry Detergent & Cosmetics* Vol. 1, 8-11.

Ficheux, A.S., Bernard, A., Chevillotte, G., Dornic, N. and Roudot A.C., (2016) "Probabilistic assessment of exposure to hair cosmetic products by the French population". *Journal of Food and Chemical Toxicology*, Vol. 92, 205-216

Frosch, F., Hinz, W., Pfrommer, E., Reinhardt, R. D., Richter, H., Sperling, K. and Wekel, H. U. (1994). *Assessment of polymers for hair setting. Spray Technology & Marketing*, May 1994, pp. 25-29.

Bogacki, J., Naumczyk, J., Marcinowski, P. and Kucharska, M. (2011). "Treatment of cosmetic wastewater using physicochemical and chemical methods", *CHEMIK* Vol. 65, 2, 94-97.

Ma, G. and Chen, J. (2018). "Nitrogen and Phosphorus Pollutants in Cosmetics Wastewater and Its Treatment Process of a Certain Brand". *IOP Conf. Series: Earth and Environmental Science*, Volume 113, 012051.

Marsh, J., Gray, J. and Tosti, A. (2015). *Healthy Hair*. New York: Springer International Publishing Switzerland

Robbins, C. R. (2012). *Chemical and Physical Behavior of Human Hair*. 5th Edition ed. Heidelberg: Springer. ISBN 978-3-642-25610-3.

Schueller, R. and Romanowski, P. (2000). "Fundamentals of formulating hair care products". *Cosmetics and toiletries* 115 (10), 67-73.

Templeton, M. and Butler, D. (2011). *An Introduction to Wastewater Treatment.* London: Ventus Publishing ApS. ISBN 978-87-7681-843-2.

U.S. Environmental Protection Agency (U.S. EPA), (2002). *Non-confidential inventory update reporting production volume information*. Toxic Substances Control Act (TSCA) Inventory,

Yin, N. E., Kissinger, R. H., Tolgyesi, W. S. and Cottington, E. M. (1977). "The effect of fiber diameter on the cosmetic aspects of hair". *Journal of the Society of Cosmetic Chemists*, Vol. 28, No. 3, 139-150.

Turkish Journal of Engineering

Turkish Journal of Engineering (TUJE)
Vol. 3, Issue 2, pp. 102-105, April 2019
ISSN 2587-1366, Turkey
DOI: 10.31127/tuje.456741
Compilation Article

THE REMOVAL OF NICKEL IONS WITH WALNUT SHELL

Şevket Tulun *1, Tolga Bahadır [2], İsmail Şimşek [3] and Mustafa Karataş [4]

[1] Aksaray University, Engineering Faculty, Environmental Engineering Department, Aksaray, Turkey
ORCID ID 0000-0002-0570-7617
sevkettulun@gmail.com

[2] Aksaray University, Engineering Faculty, Environmental Engineering Department, Aksaray, Turkey
ORCID ID 0000-0001-9647-0338
tolgabahadir61@gmail.com

[3] Aksaray University, Engineering Faculty, Environmental Engineering Department, Aksaray, Turkey
ORCID ID 0000-0003-1950-5159
ismailsimsek83@hotmail.com

[4] Aksaray University, Engineering Faculty, Environmental Engineering Department, Aksaray, Turkey
ORCID ID 0000-0001-8137-7253
mkaratas33@gmail.com

---

* Corresponding Author

Received: 03/09/2018 Accepted: 25/10/2018

ABSTRACT

The present study was aimed at determining whether walnut shell would have acceptable adsorption efficiency for removing Ni (II) and thereby offer an effective and economical alternative to more expensive treatments. This paper describes the removal of Ni (II) ions from aqueous solutions containing 100 mg L^{-1} of nickel using walnut shell. The effects of various parameters such as optimum adsorbent mass, contact time, pH of the medium were investigated. The maximum removal efficiency of 43.23% was obtained at a pH of 5.85 with a 5-min contact time for a 5 mg L^{-1} solid-to-liquid ratio and an initial heavy metal concentration of 100 mg L^{-1}. it can be concluded that walnut shell could be used as a low-cost and abundant source for the removal of Ni (II), and as an alternative to more costly materials such as ion-exchange resins and activated carbon. It is thought that it will be possible to make walnut shell modification studies in order to obtain higher increases in recovery efficiency.

Keywords: *Adsorption, Nickel Removal, Walnut Shell*

1. INTRODUCTION

Heavy metal pollution in many parts of the world is an important economic and environmental problem (Whang *et al.,* 2009). Heavy metals are defined as metals with a density of 5 g cm^{-3} (Kobielska *et al.,* 2018). Heavy metals are transferred to the environment through many industrial activities such as mining, metal plating, painting, automobile production and metal processing. In order to meet water and food quality standards, heavy metals in the environment need to be monitored (Feizi and Jalali, 2015). In addition, it has been determined that high concentrations of heavy metals have negative effects on human, animal and plant health (Çelebi and Gök, 2015). Lead (Pb), Cadmium (Cd) and Nickel (Ni), which are among heavy metals, are considered important environmental contaminants.

Natural nickel is a mixture of five stable isotopes. Although it occurs in many oxidation cases, its common oxidation under environmental conditions is Ni (II). Ion radius of Ni (II) shows similarity with other cations (Ca, Mg). In contrast, Cd and Pb have high transportation and mobility (Amari *et al.,* 2017).

Although the World Health Organization (WHO) determined the maximum acceptable nickel concentration in drinking water as 0.02 mg L^{-1}, it has been determined that the nickel concentration in industrial wastewaters has reached 900 mg L^{-1}. If no treatment is made, these wastewaters may contaminate drinking water resources (Ong *et al.,* 2017). Harmful health effects of having high concentrations of Ni(II) ions in drinking water include anemia, diarrhea, encephalopathy, hepatitis, lung and kidney damage, gastrointestinal distress, pulmonary fibrosis, renal edema, skin dermatitis, and central nervous system dysfunction. Due to these adverse effects, it is important to take measures in removing nickel from contaminated wastewaters before discharge to the environment (Mangaleshwaran *et al.,* 2015)

It is typically used in processes like production of stainless steel, coins, metallic alloys, super alloys, nonferrous metals, batteries, copper sulfate, electroplating, forging, compound for coloring ceramics, mineral processing, paint formulation and team-electric power plants, and as a catalyst (Raval *et al.,* 2016; Ghaee *et al.,* 2012).

Related to the removal of heavy metals in the water, there are various methods such as chemical precipitation (Mauchauffee and Meux, 2007) reverse osmosis (Mohsen-Nia *et al.,* 2007), ion exchange (Verma *et al.,* 2008), coagulation (El Samrani *et al.,* 2008) and adsorption (Gupta *et al.,* 2003; Gupta and Ali, 2004; Gupta and Ali, 2000; Zabihi *et al.,* 2009).

Among these methods, adsorption process offers an attractive alternative because it can provide treatment with cheap adsorbents (Cao *et al.,* 2014). Sorption process by using biosorbents is based on use of organic sorbents such as agricultural residues. The application of different sorbents such as sugar beet pulp, rice husk, carrot residue, bagasse, corn stalk, bacterial biomass, rice straw, green tomato husk, sugarcane bagasse, banana pee and sunflower residues have been recently investigated (Feizi and Jalali, 2015). Walnut shells, which are used as solid fuel in Turkey, are agricultural wastes that can be found in large amount. When the structural analysis of walnut shell was examined, it was determined that it had a lignocellulosic structure containing 17.74% cellulose, 36.06% hemicellulose and 36.90% lignin (Altun and Pehlivan, 2012).

Due to its wide surface area, high mechanical strength, chemical stability and easy regeneration, the walnut shell has been successfully used to remove heavy metals such as Cesium, Copper, Chromium (IV), Zinc and Mercury from wastewaters (Cao *et al.,* 2014).

The main purposes of this study are to remove Ni (II) from aqueous solution by using walnut shells that can be found cheap and in a large amount in our country and to investigate the beneficial usage of the walnut shell that is seen as agricultural waste.

The effects of factors such as contact time, pH, adsorb concentration on the studies of Ni (II) adsorption were investigated.

2. MATERIAL AND METHOD

2.1. Adsorbents and chemicals

Walnut shells were obtained from walnut trees grown in Usakpinar, a village in Silifke County of Mersin Province in the Mediterranean Region of Turkey. Walnut shells were shredded with grinders (Arnica, GH21520), the particles were sifted through a series of sieves, and only the samples passing from the pore diameter of 212 µm were used in this study. Walnut shells were washed 3 times with distilled water and the effects that could emerge due to the foreign substances in their structures were prevented. Then, they were dried in a drying oven (Memmert, UNB-400) at 70 °C for 24 hours.

In this study, Ni^{+2} having 100 mg L^{-1} concentration was used. The stock Ni (II) (1000 mg L^{-1}) solution was prepared by using $NiCl_2*6H_2O$ chemical compound. The pH value of each solution was set to the desired values by adding 0.1 M NaOH or 0.1 M HNO_3. All chemical compounds used to prepare reactive solutions were prepared in analytical quality (Merck)

2.2. Measurements

All batch experiments were carried out in series of 250 mL Erlenmeyer flasks Adsorption studies were carried out in the specific period at the temperature of 25°C in the thermal mixer (ZHWY-200B, ZHICHENG Analytical Co., Ltd). After adsorption process, samples were filtered from 0.45 µm membrane filters. Ni^{+2} concentrations of the filtered samples were analyzed by using an inductively coupled plasma mass spectrometry (Optima 2100DV ICP, Perkin-Elmer, Boston, MA) (SM: 3120 B). pH measurements (SM: 4500- H^+ B) were performed using multi- electrode digital ion analyzer (Hach, HQ440d Multi) (APHA, 2005).

2.3. Experimental procedure

The effects of adsorbent mass, operating time and pH on the adsorption were examined by using the experimental conditions shown in Table 1. Experimental adsorption studies were carried out within 250 mL erlenmeyer flask.

Table 1. Adsorption process was carried experimental conditions

	Agitating speed (rpm)	**Adsorbent content (mg L^{-1})**	**Time (min)**	**pH**	**Initial solution of nickel**
Effect of adsorbent mass, Ms (g)	150	0,5-5,0	60	5,85	100,6
Effect of contact time, t (min)	150	5,0	0-120	5,85	103,2
Effect of pH	150	5,0	5,0	2-6	104,3

Each study was performed in 3 repetitions and the results were given as mean values. In the study, tests were repeated to check for errors in cases where standard errors are greater than 0.01.

3. RESULTS AND DISCUSSIONS

3.1. Effect of the adsorbent amount

The effect of adsorbent mass on adsorption of Ni (II) was examined by using 100 ml of 100 mg L^{-1} Ni (II) solution during 60-minute operation process of 0.5-5.0 mg walnut shell samples.

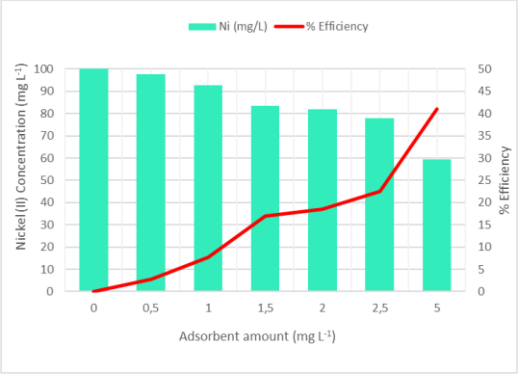

Fig. 1. Effect of the adsorbent amount

As seen in Figure 1, the adsorption of Ni (II) increased gradually with the increasing adsorbent amount and it was determined that the optimum walnut shell concentration was 5 mg L^{-1}. It was shown that the proportional increase between adsorbent concentration and removal efficiency was associated with the increase in the amount of adsorbent per unit contaminant.

3.2. Effect of contact time

The effect of contact time was studied by using Ni (II) solution that had constant concentration at room temperature. The adsorption of Ni (II) heavy metal was examined at 1-120 min time intervals. The effect of contact time on adsorption is given in Figure 2.

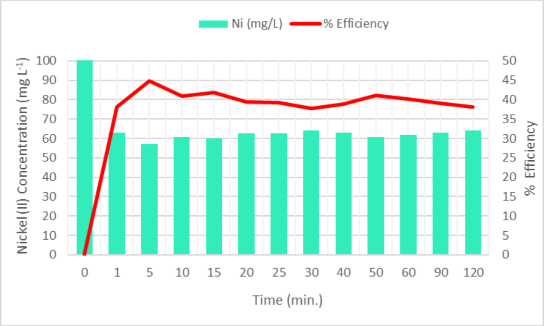

Fig. 2. Effect of contact time

Because increasing of the contact time in adsorption studies significantly increases the costs, time optimization needs to be done. As shown in Figure 2, the highest adsorption efficiency was obtained in 5 minute contact time (44.90%). In different contact times, decreases and increases in removal efficiency were observed. It is thought that the main reason for this situation is the desorption process, which occurs at the end of the saturation of heavy metals that hold onto the surfaces of walnut shells.

Based on these results, the optimum contact time was determined to be 5 minutes.

3.3. pH Effect

The effect of pH on walnut shells and Ni (II) heavy metals that have 100 mg L^{-1} initial concentration was investigated in pH 2-6 range. The effect of Ni (II) on adsorption in determined pH values was shown in Figure 3.

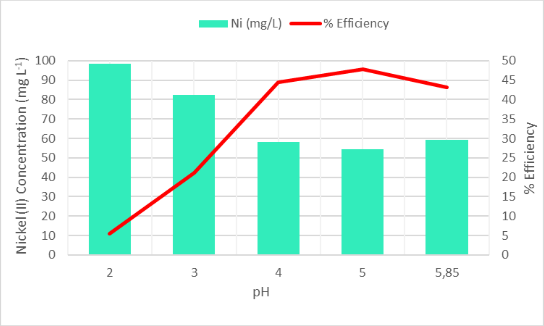

Fig. 3. Effect of pH

Because of the coating of the surface of the walnut shell due to the increase in H^+ ion concentration at low pH values, Ni (II) ions were not able to hold on to the surface. As a result of this, the removal efficiency was determined as 5.53%. Depending on the increases in pH values, increases in removal efficiency were obtained.

Although the highest removal efficiency was obtained in pH 5 with 47.82%, the solution's own pH value (5.85) was determined as the most appropriate pH value. In pH 5.85, the removal efficiency of 43.23% was obtained. Given the economic factors, the effect of the use of chemical substances to change pH value on the adsorption efficiency has been neglected.

4. CONCLUSIONS

In this study, it was determined that by using the walnut shell found as common agricultural waste, removing of the heavy metal Ni (II) with aqueous adsorption process was possible. The removal efficiency of 43.23% was obtained in 5 mg L^{-1} adsorbent concentration at 5 minute contact time and pH 5.85. It was concluded that the walnut shell can be used as a low-cost and abundant source for the removal of Ni (II) from water and it can be also used as an alternative to expensive materials such as ion exchange resins and active carbon. It is thought that obtaining higher increases in removal efficiency can be possible by making modification studies of walnut shell.

REFERENCES

Altun, T., Pehlivan E. (2012). “Removal of Cr(VI) from aqueous solutions by modified walnut shells.” *Food Chemistry*, Vol. 132, pp. 693-700.

Amari, T., Ghnaya, T., Abdelly, C. (2017). “Nickel, cadmium and lead phytotoxicity and potential of halophytic plants in heavy metal extraction.” *South African Journal of Botany*, Vol. 111, pp. 99-110.

APHA (2005), Standard methods for the examination of water and wastewater, American Public Health Association (ALPHA): Washington, DC, USA.

Cao, S.-J., Lin, X.-J., Fang, F., Zhang, T.-M., Hu, R.-Z. (2014). “A new absorbent by modifying walnut shell for the removal of anionic dye: Kinetic and thermodynamic studies.” *Bioresource Techonology*, Vol. 163, pp. 199-205.

Çelebi, H., Gök, O. (2015). “Evaluation of lead adsorption.” *International Journal of Environmental Research*, Vol. 11, pp. 83-90.

El Samrani, A.G., Lartiges, B.S., Villieras, F. (2008). “Chemical coagulation of combined sewer overflow: Heavy metal removal and treatment optimization.” *Water Research*, Vol. 42, pp. 951-960.

Feizi, M., Jalali, M. (2015) “Removal of heavy metals from aqueous solutions using sunflower, potato, canola and walnut shell residues.” *Journal of Taiwan Institute of Chemical Engineers*, Vol. 54, pp. 125-136.

Ghaee, A., Shariaty-Niassar, M., Barzin, J., Zarghan, A. (2012). “Adsorption of copper and nickel ions on macroporous chitosan membrane: equilibrium study.” *Applied Surface Science,* Vol. 258, pp. 7732–7743.

Gupta V.K., Ali L. (2000). “Utilization of bagasse fly ash (a sugar industry waste) for the removal of copper and zinc from wastewater.” *Separation and Purification Technology*, Vol, 18, pp. 131-140.

Gupta V.K., Ali L. (2004). “Removal of lead and chromium from wastewater using bagasse fly ash – a sugar industry waste.” *Journal of Colloid and Interface Science*, Vol, 271, pp. 321-328.

Gupta, V.K., Jain, C.K., Ali, L., Sharma, M., Saini, V.K. (2003). “Removal of cadmium and nickel from wastewater using bagasse fly ash – a sugar industry waste.” *Water Research*, Vol. 37, pp. 4038-4044.

Kobielska, A.P., Howarth, J. A., Farha, K. O., Nayak, S.(2018). “Metal-organic frameworks for heavy metal removal from water.” *Coordination Chemistry Reviews*, Vol. 358, pp. 92-107.

Mangaleshwaran, L., Thirulogachandar, A., Rajasekar, V. Muthukumaran, C.,Rasappan, K. (2015). “Batch and fixed bed column studies on nickel (II) adsorption from aqueous solution by treated polyurethane foam.” *Journal of the Taiwan Institute of Chemical Engineers,* Vol. 55, pp. 112–118.

Mauchauffee, S., Meux, E. (2007). “Use of sodium decanoate for selective precipitation of metals contained in industrial wastewater.” *Chemospher*, Vol. 69, pp.763-768.

Mohsen-Nia, M., Montazeri, P., Modarress H. (2007). “Removal of Cu^{2+} and Ni^{2+} from wastewater with a chelating agent and reverse osmosis processes.” *Desalination*, Vol. 217, pp. 276-281.

Ong, C.D., Kan, C.-C., Mae, S., Pingul-Ong, B., Daniel, M., de Luna, G. (2017). “Utilization of groundwater treatment plant (GWTP) sludge for nickel removal from aqueous solutions: Isotherm and kinetic studies.” *Journal of Environmental Chemical Engineering*, Vol. 5, pp. 5746-5753.

Raval, N.P., Shah, P.U., Shah, N.K. (2016). “Adsorptive removal of nickel(II) ions from aqueous environment: a review.” *Journal of Environmental Management*, Vol. 179, pp. 1–20.

Verma,V.K., Tewari, S., Rai, J.P.N. (2008). “Ion exchange during heavy metal bio-sorption from aqueous solution by dried biomass of macrophytes.” *Bioresource Technolgy*, Vol. 99, pp. 1932-1938.

Verma,V.K., Tewari, S., Rai, J.P.N. (2008). “Ion exchange during heavy metal bio-sorption from aqueous solution by dried biomass of macrophytes.” *Bioresource Technolgy*, Vol. 99, pp. 1932-1938.

Whang, S.X., Li, Z.Z., Tao, R.S. (2009). “Removal of chromium (VI) from aqueous solution using walnut hull.” *Journal of Environmental Management*, Vol. 90, pp.721-729.

Zabihi, M., Ahmadpour, A., Asl, H. A. (2009). “Removal of mercury from water by carbonaceous sorbents derived from walnut shell.” *Journal of Hazardous Materials*, Vol, 167, pp. 230-236.

CONTENTS

ISSN 2587-1366

TURKISH JOURNAL OF ENGINEERING

VOLUME 3 ISSUE 2 APRIL 2019